Wall-Modelled Large Eddy Simulation of fully rough non-uniform flow for the purpose of predicting stone stability

by

## Lina Nikolaidou

TU Delft

Deltares
Enabling Delta Life

Wall-Modelled Large Eddy Simulation of fully rough non-uniform flow for the purpose of predicting stone stability

by

Lina Nikolaidou

in partial fulfilment of the requirements to obtain the degree of

Master of Science

in Civil Engineering

at

Delft University of Technology

to be defended publicly on Wednesday August 28, 2019 at 09:00 AM.

Student number:	4631943
Thesis committee:	Prof. dr. ir. W.S.J. Uijttewaal TU Delft
	Dr. ir. B. Hofland TU Delft
	Dr. ir. J.D. Bricker TU Delft
	Dr. ir. T. O'Mahoney Deltares
	Dr. ir. N.G. Jacobsen Deltares

An electronic version of this thesis is available at `http://repository.tudelft.nl/`.

TUDelft

Deltares
Enabling Delta Life

Preface

The present thesis concludes my master studies in Hydraulic Engineering at Delft University of Technology. The research is a collaboration between Deltares and TU Delft. It was carried out at the office of Deltares in Delft, within the Hydraulics for Infrastructure and Industry department.

Firstly I would like to thank my thesis committee members, who formed a strong and diverse group that helped me develop my work. I truly enjoyed all our dynamic discussions during the progress meetings and I always looked forward to those. I would like to thank Wim Uijttewaal, for his sharp remarks and also for the motivation and inspiration he gave me to pursue a msc thesis in turbulence and turbulence modelling in the first place. My gratitude also goes to Tom O'Mahoney, for his supervision for more than one year during my internship and thesis at Deltares. Our discussions on theory and applications, helped me develop in a personal and professional level. I would also like to thank Bas Hofland, for giving me the opportunity to work on such an interesting topic. His enthusiasm and insights on this topic always made me leave our meetings with full energy. I am also glad for the involvement of Niels Jacobsen in this work, for his keen remarks on both numerical modelling and theoretical aspects that helped me improve my work. I would also like to thank Jeremy Bricker for his feedback and for helping me connect with other people working on similar research areas. That being said, I would like to thank Dr. Timofey Mukha for our insightful meetings during his visit in Delft and later via e-mail. These helped me position my msc thesis work in a bigger research area and realize the boundaries and possibilities of this work. Lastly, I would like to thank Akshay Patil, fellow CFDer, for his crucial help with regards to HPC supercomputing and various technical challenges I faced with OpenFOAM.

I am very glad I decided to conduct my internship and master thesis at Deltares. It has been the perfect learning environment for me. Special thanks to all the people I met during my stay in Deltares, which made my experience working there unforgettable. I am also thankful to all the friends I made in TU Delft. Vassia and Fontas, thank you for your support during our studies. And of course, thank you Antonis for being by my side until the end.

Lastly, I want to express my gratitude to my parents and my brother, for their unconditional love and support.

Lina Nikolaidou
Delft, August 2019

Abstract

Granular bed protections are a common measure to mitigate scour of the sand bed around hydraulic structures like groynes, breakwaters, piers and storm surge barriers. The layers of stones applied must be able to withstand the forces exerted on them by the flow. In practice, in order to arrive to the needed rock grading, calculations are done with simple stability formulas that represent the ratio of destabilizing to stabilizing forces. However, these formulas include simplifications on rather complex non-uniformity and turbulence related phenomena, leading to conservative designs.

In view of marching towards cost-effective solutions to tackle erosion-related problems, it is important to predict more accurately the loads exerted on the bed and come up with the needed rock grading. To that end, a 3D eddy resolving modelling technique could help in formulation of a new stability formula, based on extreme local flow conditions. That being said, it is the aim of this thesis to build a hydrodynamic numerical tool, able to predict governing mechanisms in stone stability and able to be used for the derivation of such a formula.

The present numerical study aims to contribute to a bigger research area related to stone stability. Previous works done include Steenstra et al. (2016)and Stevens (2018). To that end, addition post processing is conducted to the work of Stevens (2018) and more specifically on the limitations of the numerical model applied there. The shear layer development and also the range of the flow scales that the model used in this study was able to resolve, where identified as the main points that have room for improvement. Further investigation on numerical modelling techniques and ways to incorporate the bottom roughness elements in the model, led to the selection of the Wall-Modelled Large Eddy Simulation (WMLES) as a next step in this research area. The model was build using the open-source CFD toolbox OpenFOAM.

Firstly, in order to access the performance of wall functions that include the effect of roughness in the LES environment, simple Open Channel flow cases are build. Tests are done using different wall functions, sub-grid scale models and grid cell size to equivalent sand grain diameter ratios. It was shown that the set-up of a Smagorinsky sub-grid model with the `nutURoughWallFunction` as implemented in OpenFOAM and also with a cell size to equivalent sand grain diameter of about 1.2 yielded the best results. In the absence of experiments, the validation was done using the theoretical log-law for rough surfaces. Further validation with experimental results is suggested in order to minimize the uncertainty of the theoretical prediction.

Secondly, the performance of the WMLES is assessed by simulation a backward facing step kind of flow, from the experimental set of Jongeling et al. (2003). In this case both free and wall turbulence are present. A comparison with the experimental results showed that again the Smagorinsky sub-grid model performed best among the ones tested. The model was able to capture the separation region and the shear layer development after the step. Comparison of mean turbulent kinetic energy of the experiment, showed an over prediction in the points up to one step height above the bed. Further investigation is suggested on this feature. The synthetic turbulence production boundary condition in the inlet of the domain is hypothesized as a parameter than could cause such a behavior so further investigation is suggested on that. However, the model was able to resolve eddies down to the stone size that were considered important for the initiation of motion of a stone.

The numerical model suggested here to be used for the derivation of a new stability formula, showed some improvements over the previous numerical models suggested in this research area and recommendations are suggested in order to arrive to a more accurate and well-validated numerical model. Among them, more detailed experiments are suggested to be undertaken so that the reproduction and validation of a "numerical twin" is improved. Special attention should be paid to the description of the near wall region.

Lastly, it is noted that in order to simulate 3 minutes of the experiment 30 days were needed, meaning that the costs of the WMLES simulations should not be neglected.

Contents

Nomenclature

Abbreviations	Meaning
3D	three Dimensional
BFS	Backward Facing Step
CFD	Computational Fluid Dynamics
DES	Detached Eddy Simulation
DNS	Direct Numerical Simulation
IDDES	Improved Delayed Detached Eddy Simulation
LES	Large Eddy Simulation
meas	Measured
PIV	Particle Image Velocimetry
QSF	Quasi Steady Forces
RANS	Reynolds Averaged Navier Stokes
SEM	Synthetic Eddy Method
SGS	Subgrid-Scale
TKE	Turbulent Kinetic Energy
TWP	Turbulent Wall Pressures
WMLES	Wall-Modelled Large Eddy Simulation

Introduction

In this chapter, the topic of this thesis is first positioned in the research area that it will aim to serve. After that, a more specific definition of the topic will be given. Subsequently, the research objective and questions will be posed, followed by the research methodology. Finally the outline of the thesis will be presented.

1.1. Background

Granular bed protections are a common measure to prevent scour of the sand bed around hydraulic structures. In view of marching towards cost-effective solutions to tackle erosion-related problems, it is important to accurately predict the loads exerted on the rock particles and come up with the needed rock size. However, predicting the forces and assessing the damage in bed protections is far from trivial.

In practice, to determine the rock size, use is made of simple formulas originally derived for uniform flows, which include corrections for non-uniform flows in form of empirical coefficients. Furthermore, a critical stability parameter is defined, above which the bed becomes unstable. The use of these empirical factors prevents the method from being "generally applicable" and imposes crude simplifications on rather complicated turbulence and non-uniformity related phenomena. The concept of a single critical stability number to determine bed stability is also contradicting with the economic and efficient way towards which engineers are striving.

Figure 1.1: Storm surge barrier in Rotterdam Waterway (source: www.dutchwatersector.com)

A famous example of a hydraulic structure that needs such bed protection, is the storm surge barrier in Rotterdam (see figure 1.1). The barrier consists of two convex steels gates, which rotate around a spherical hinge.During the closure, the gates converge and are lowered on top of concrete blocks. At the lowering, high velocities occur between the gates and the concrete blocks. Which are then the dominant forces occurring on top and after the sill? How are they related to the rock size of the bed protection needed?

1.2. Problem definition

In recent years, stability parameters are developed that are based on local flow characteristics and take into account the effects of turbulence explicitly. To that end, use of Computational Fluid Dynamics (CFD) is made to predict the local (fluctuating) forces that give rise to stone movement. Contrary to scale models, which offer a limited amount of flow characteristics' information, a well-validated 3D eddy resolving numerical model is likely to offer much more possibilities. In addition, the use of CFD modelling seems like an economic method that enables the user to extrapolate the theory to different geometries. The application of interest itself and the numerical power available are the main considerations when choosing to apply CFD.
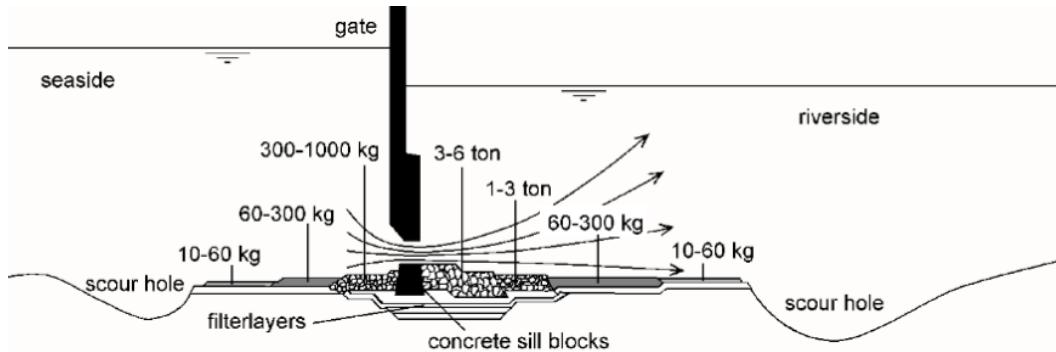
Figure 1.2: Cross section of the bed protection in Rotterdam storm surge barrier (from Schiereck and Verhagen (2012))

Seeing figure 1.2, we discern an acceleration region on top of the sill and also a deceleration region after the sill. In addition, we expect the development of both free turbulence over the sill and also wall turbulence close to the bottom. To that end, when choosing a CFD model, one must pay attention to both the precise development of the shear layer and also to choosing an efficient way to represent the bottom roughness. Furthermore, flow separation is expected behind the sill, with the critical area being a few step heights away from the downstream tip of the sill. This is also realized from the heavier bed protection being on the riverside in figure 1.2. All the above are taken into account to arrive in a modelling technique in the current thesis.
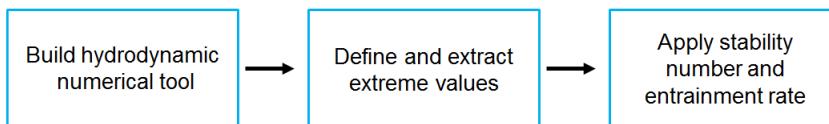
Figure 1.3: Research components in stone stability

It must be noted that the investigation of the hydrodynamic processes in stone stability in non-uniform flow, is part of a bigger system comprising of three components. These can be seen in figure 1.3 in a simplified schematic way. When followed one by one, it is possible to arrive at the definition of the stone size in bed protection. The current thesis only deals with the first step, namely with the hydrodynamic modelling of this research topic. However, research is undertaken also for the other ones. However, research is undertaken also for the other ones. In appendix A, basic concepts and ideas for further work on the last two components is given.

1.3. Objective and research questions

In order to arrive at a well-formulated stability formula for the design of bed protections, a better prediction is needed of the governing physical mechanisms in non-uniform and fully rough flows. In this research an attempt is made to build a numerical model able to predict the hydrodynamics in such flows. The objective of this study is then:

To establish a hydrodynamic numerical tool for the purpose of simulating high Reynolds number non-uniform flows associated with stone stability

Important considerations in this study area are:

- The choice of the modelling technique.
- The choice of the flow scales resolution. What is modelled and what is resolved?
- The method to represent the rough boundary.

It is also the aim of the thesis to establish a trade-off between:

- Resolving flow scales that contribute to the initiation of motion of stones in a gravel bed.
- The computational time demands of the engineering application of interest.

The main research question is formulated as:

Which hydrodynamic numerical tool can be used for the prediction of the governing mechanisms associated with stone stability, in case of non-uniform high Reynolds number flows?

Sub-questions:

1. How can the previously applied IDDES model be improved for predicting stone stability?
2. Which is the most appropriate method to include bottom roughness in the case of granular bed protections in high Reynolds number engineering flows based on literature?
3. How does WMLES perform in predicting wall shear stress in fully rough open channel flow?
4. Which sub-grid scale model is more appropriate when modelling rough walls with wall functions in LES?
5. How does WMLES perform in predicting high frequencies important for stone stability studies?

1.4. Methodology

The methodology followed to answer the research questions is summarized in the following steps. Each step contributes to answering one or more research sub-questions. This is also indicated in the following:

1. Identification of the governing mechanisms in stone stability.(sub-question 1)
2. Additional post-processing of the output of the IDDES model used in the current research area. (sub-question 1)
3. Investigation of methods to represent rough boundaries in the LES environment from literature. (sub-question 2)
4. Selection of an appropriate experiment to simulate.
5. Selection of an appropriate numerical code.
6. Numerical modelling. (sub-questions 3,4,5)
7. Analysis of the results. (sub-questions 3,4,5)
8. Conclusions and Recommendations (main research question)

It can be seen that the first sub-question is mainly answered by further post-processing the numerical results of a previous research study (Stevens (2018)), while the second sub-question is answered by literature study. The rest of the sub-questions are answered from the analysis of the numerical modelling undertaken in the current thesis.

1.5. Thesis Outline

In chapter 2, the literature review is presented. This starts with an investigation of the governing hydrodynamics mechanisms in stone stability. After that past numerical studies undertaken for the purposes of the present research area discussed. Special attention is paid on the potential of WMLES and on the near wall treatment in the case of rough boundaries. In chapter 3, the model set-up of the simulations undertaken is described in detail. Results and some analysis are presented in chapter 4, followed by the discussion in chapter 5. Finally, answers to the research questions are given in chapter 6 and recommendations for further research are given in chapter 7.

<div style="text-align: right; font-size: 3em;">2</div>

Literature review and previous studies

In this section, a review is given, of the governing physical mechanisms and flow conditions relevant to stone stability studies. Next, the numerical modelling techniques are discussed and the suitability of them for predicting governing mechanisms is argued. Special attention is paid to the previous numerical studies done within this research area and the uncertainties present in them. Various methods to include bottom roughness in numerical models are also elaborated. Finally, the experiment selected to model in the next chapters is described.

2.1. Governing hydrodynamic mechanisms in stone stability

In this section, the basic concepts in stone stability are presented, which are necessary to discuss before proceeding to the numerical modelling chapter. Important physics and the current knowledge within the topic are included.

2.1.1. Force origins

When zooming in on a single stone, we usually distinguish in a drag force and a lift force, the drag being the streamwise force component and the lift the vertical. In case of a constant velocity above the bed, these are proportional to the stream wise velocity squared. Therefore, the drag and lift forces can be expressed in general form as in:

$$F_D = \frac{1}{2} C_D A_D \rho u u \tag{2.1}$$

$$F_L = \frac{1}{2} C_L A_L \rho u u \tag{2.2}$$

where

C_D is the drag coefficient (-)
C_L is the lift coefficient (-)
A_D the surface area exposed to the drag force (m^2)
A_L the surface area exposed to the lift force (m^2)
u the velocity in the vicinity of the stone, usually taken as the mean velocity $\overline{u}$ (m/s)

However, flow around a rough bed is turbulent. The extreme forces that cause stone movement occur due to fluctuations. Coherent structures can cause a fluid package from higher up the water column to be transported downwards the bed, resulting in a fluctuating force at the bed.

Because it is basically the same flow mechanism that causes the forces on the stone in steady flow, these forces are referred to as the quasi-steady forces (**QSF**). They originate from the presence of the stones in the field. These forces induce a streamline curvature of the flow passing a stone. The associated pressure differences from this mechanism are included in the QSF mechanism.

Generally, the fluctuating parts of the velocity are much smaller than the mean velocity. However, in Hofland (2005) it is stated that close to the bed the extreme values of velocity fluctuations u' can have the same order of magnitude as $\overline{u}$ itself. This means that their contribution to the forces on the stone is considerable. Substituting $u = \overline{u} + u'$ in the normal drag/lift law of equations 2.1 and 2.2, leads to:

$$F'_D \propto \overline{u}^2 + u'^2 + 2\overline{u}u' \tag{2.3}$$

$$F'_L \propto \overline{u}^2 + u'^2 + 2\overline{u}u' \tag{2.4}$$

In addition to the quasi-steady forces, turbulent wall pressure fluctuations (**TWP**) also contribute to the initiation of motion. For this type of forces, the presence of a rough bed is not necessary. That is because in turbulent flow, acceleration of water particles and streamline curvature are always present.In the work of Hofland (2005), the pressures on a cube placed under uniform and non-uniform flow are measured, to study the contribution of TWP-forces. In Hofland (2005) it is concluded that TWP-forces are particularly important for low stone protrusions (stones shielded by other stones) and high turbulence intensities.

In the study of Vollmer and Kleinhans (2007), the need to include the turbulence-induced vertical pressure gradients in the upper sediment layer when considering the destabilization processes of the riverbed is also highlighted. It is argued that this is particularly important for particles that lie in the lee of larger ones and are not exposed to the flow. Short-term pressure fluctuations are induced by turbulent flow fluctuations above the bed, and penetrate into the bed over a depth of an order of magnitude larger than the particle size (Vollmer et al. (2002), Packman et al. (2004)). The decay of pressure fluctuations into the porous bed was found to be independent of global flow parameters, but depended solely on the roughness length scale (Vollmer and Kleinhans (2007)). Integration of this function over the full height of the particle yielded the fluctuating pressure component of the lift force.

Another cause of a fluctuating force on the particle is the unsteady separation of the flow from the particle itself. In work of Nelson et al. (1993), the variation in shear stress along the surface of ripple bed forms is measured. It was observed that the mean bed shear stress, close to the point of reattachment remained below the critical stress value required for the initiation of motion. Therefore, any sediment motion, in this place, takes place because of wake turbulence produced by the separation at the bed form crest.

The aforementioned mechanisms are illustrated in figure 2.1.
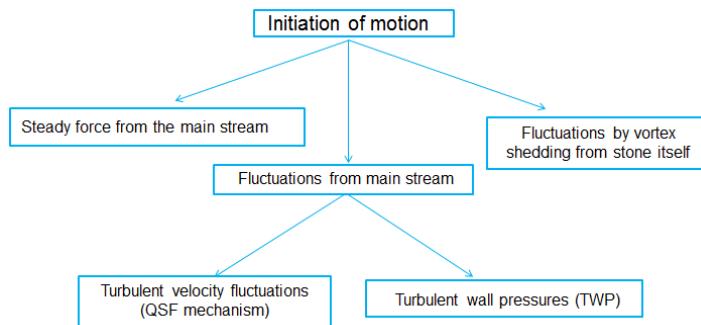
Figure 2.1: Hydraulic forces on a stone that contribute to the initiation of motion

To illustrate what the direct influence of the TWP on stone stability can be, a rectilinear model vortex in a uniform potential flow over a wall is discussed, as described by Hofland (2005). This flow field can be seen as a rough approximation of a vortex in a turbulent flow.

A point vortex with strength (circulation) κ is placed in a uniform flow, as depicted in figure 2.2. By adding a mirrored vortex, the wall is modelled. If a porous granular bed is present, this pressure gradient will penetrate further into the bed than the longitudinal velocity, which will be blocked by the surrounding stones. This pressure gradient can create a net force on a stone placed in the bed. The pressure on the stone between the dashed lines is higher on the upstream side (left) than on the downstream side, creating an increased horizontal force component. It must be noted that this counteracts the quasi steady mechanism, as at this moment u is decreased under the vortex. In Hofland (2005) it is stated that especially TWP with wavelengths of roughly 1.5d, with d being the diameter of the rock, are expected to have a large influence on the fluctuating forces. If these are caused by vortices, then the vortices will be situated at about 1d from the stone.
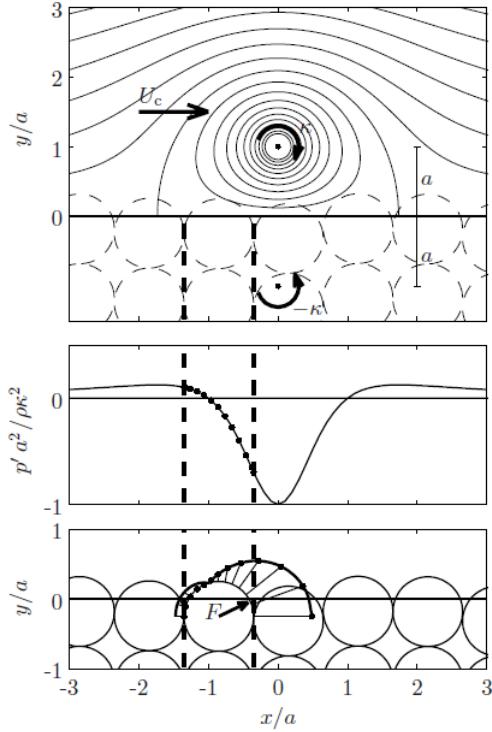
Figure 2.2: Streamlines of a 2D potential flow around a point vortex near a wall. (adjusted from Hofland (2005))

Initiation of motion

Based on Hofland (2005), both in uniform and non-uniform flow, the initiation of stone movement occurs under an exceptional combination of two normal flow structures, at least one of each has an exceptionally high magnitude. More specifically, a lift force caused by TWP and a quasi-steady drag force can cooperate to dislodge the stone from the bed. Stones that initially do not protrude far into the flow, experience a lift force that increases their exposed area and subsequently, an increased streamwise velocity u, transports the stone. In the latter, usually a Q4 event (sweep event with u'>0 and w'<0) is responsible for increased drag forces via the QSF mechanism.

2.1.2. Mathematical description of flow forcing

In Hofland (2005), a general formula for the stability parameter ψ is given by:

$$\Psi = \frac{(C_B(\bar{u} + \tilde{u}')^2 + C_m(\bar{\tilde{a}} + \tilde{a}')d)_{max}}{\Delta g d} \tag{2.5}$$

In the above equation, the nominator acts as the destabilizing force (m^2/s^2) and the denominator, $\Delta g d$, as the resistance part (m^2/s^2) and is a function of the stone diameter d. In the nominator:

C_B is a combined drag and lift coefficient (-)

C_m is the added mass coefficient (-)

a is the acceleration (m/s^2)

u is the streamwise velocity (m/s)

<~> denotes projection on the bed

< − > denotes time averaging

<′> denotes fluctuation over the mean

<max> refers to the use of an extreme value for the occurring forces

It must be noted that this is a general stability formula, which does not include separate terms for the QSF and TWPs as described before. It just denotes that a maximum force responsible for the stone displacement is expressed by the summation of the instantaneous squared velocity and acceleration. In that case, it is considered that the QSFs and TWPs are implicitly included. The exact definition of the maximum is an open topic, but a probabilistic method is most likely to be required.

From as early as Shields (1936) and Isbash (1932), researchers try to approach as much as possible the above form of the formula. In other words, they try to include as many physical processes as they can and translate them in a mathematical form. The use of the depth-averaged flow velocity $\overline{u}$, was the first term to be included. The effect of turbulence was then taken into account by empirical coefficients and then by the use of the turbulent kinetic energy k (e.g. Jongeling et al. (2003), Hoan (2008), Hoffmans (2006)) and De Gunst (1999)). That is in accordance with the development of numerical models, which are of aid in this topic, where usually a RANS modelling technique is applied. In that case the kinetic energy k is the output of the turbulence closure model, which is then applied in the formula. Afterwards, the steady spatial acceleration term was added. The influence of the averaged acceleration on stone stability is among others studied by Dessens (2004), Huijsmans (2006) and Steenstra (2014). The last part to be included in the formula are the acceleration fluctuations. This was studied by fewer researchers eg. Tromp (2004) who focused on the influence of fluid accelerations due to waves on the threshold of motion. He included the total derivative of velocity in the drag force. Finally, in Stevens (2018), it was the first time that a detailed eddy resolving modelling technique was used for the aim of determining the stone stability in a granular bed protection. This resulted in an additional step in including all the relevant processes in this topic. Nevertheless, Steenstra (2014) was the last one to introduce a well calibrated stability formula. The stability parameter of the formula reads:

$$\psi_{RS} = \frac{(max[\left\langle \overline{u} + \alpha \sqrt{k} \right\rangle_{Lm}]^2) + C_{m:b}(\overline{u}\frac{\theta \overline{u}}{\theta x})_{h_\alpha} d}{K(\beta)\Delta g d} \qquad (2.6)$$

It must be noted that instead of using accelerations, often these formulas include pressure gradients. These two are linked through Newton's second law. More specifically, a negative pressure gradient means accelerations, while a positive pressure gradient means deceleration.

In equation 2.6, the steady spatial acceleration term $\overline{u}\frac{\theta \overline{u}}{\theta x}$ is used. It stems from the total derivative of velocity:

$$\alpha = \frac{Du_i}{Dt} = \frac{\theta u_i}{\theta t} + u_x \frac{\theta u_i}{\theta x} + u_y \frac{\theta u_i}{\theta y} + u_z \frac{\theta u_i}{\theta z} \qquad (2.7)$$

The first term in the right hand side in equation 2.7, also called local acceleration, accounts for the TWPs or waves. The remaining terms also referred to as advective acceleration terms, account for the steady spatial acceleration due to eg. structures. How is it possible to measure these terms in experiments? How is it possible to model the corresponding processes? And finally how is the initiation of motion linked with some combination of velocity and accelerations in equation 2.5?

2.1.3. Flow over rough surfaces

In stone stability problems, the near wall region is of great importance and therefore some aspects concerning the interaction of main flow with the bottom will be discussed. Flows near a wall, where the no-slip condition is applicable, give rise to large velocity gradients. These velocity gradients along with the associated shear stresses, cause energy and momentum transfer from regions higher in the water column, to regions near the wall. The aforementioned processes are important for stone stability.

Boundary layer

In terms of the relative importance of turbulent shear stress versus viscous shear stress, it is convenient to divide the flow as depicted in figure 2.3, into a viscosity-dominated region and a turbulence-dominated region. In between the two a buffer region exist, which shows characteristics of both other regions.

The **viscous sublayer** falls into the viscosity dominated region where turbulent shear stresses can be neglected. It is a thin layer immediately adjacent to the boundary, ranging from a fraction of millimeter to many millimeters ((Southard, 2006)). Eddies originating from regions farther away from the wall are quickly damped out by viscous shear stresses within the sublayer. The **outer layer**, lies within the turbulence-dominated region. This layer extents up to the free surface. Turbulent eddies present in this layer are more efficient in transporting momentum normal to the flow direction than are the much smaller eddies nearer the boundary. Just in the middle of the two, the **buffer layer** is found. Within this layer both viscous shear stress and turbulent shear stress are too important to be ignored. Very energetic small-scale turbulence is generated there by instability of the strongly sheared flow, and there is a sharp peak in the conversion of mean-flow kinetic energy to turbulent kinetic energy, and also in the dissipation of this turbulent energy; for this reason the buffer layer is often called the turbulence-generation layer.
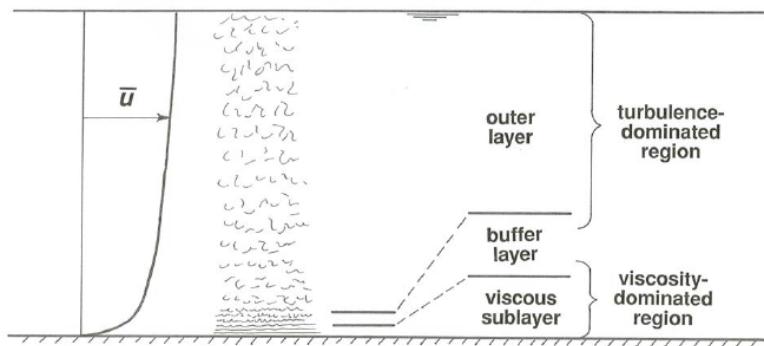
Figure 2.3: Division of turbulent open-channel flow into layers on the basis of turbulence structure (adjusted from Southard (2006))

Smooth vs Rough boundary flows

In the following, a distinction is made between physically smooth/rough boundaries and dynamically smooth/rough boundary flows.

At every point on the solid boundary, no matter how intricate in detail the geometry of that boundary may be, two kinds of fluid forces act: pressure, acting normal to the local solid surface at the point, and viscous shear stress, acting tangential to the local solid surface at the point.

In the case of a **physically smooth boundary** (upper part of figure 2.4), the downstream component of force the fluid exerts on the boundary can result only from the action of the viscous shear stresses, because the pressure forces can then have no component in the direction of flow. However, most natural flows, and many in engineering practice also, have **physically rough** boundaries. Then the picture is more complicated (middle part of figure 2.4), because there is a downstream component of pressure force on the boundary in addition to a downstream component of viscous force.

The details of pressure forces on roughness elements depend among other on the roughness Reynolds number, the shape, the arrangement and the spacing of the rough elements. Qualitatively, at low Reynolds numbers the pressure force on an element is of the same order as the viscous force, whereas at higher Reynolds numbers the pressure forces are much greater than the viscous forces. The sum of all the forces on individual roughness elements on the boundary, constitutes the overall drag on the boundary, or conversely the overall resistance to the flow. This is represented by the boundary shear stress τ_o.

Moving in characterizing the actual flow above boundaries, a comparison is made between the thickness of the viscous sublayer and the height of the roughness elements. In the case that the boundary is actually smooth, or the roughness height is smaller than the height of the viscous sublayer, the roughness elements are fully located in the viscous sublayer. The flow is then **dynamically smooth**. However, in the case that the height of the roughness elements is higher than the viscous sublayer thickness in absence of the roughness, the flow is said to be **dynamically rough**. In the latter case, flow over and among the roughness elements is turbulent, and the structure of this flow is dominated by effects of turbulent momentum transport.

If the Reynolds number of flow around individual roughness elements is small, as must be the case if the elements are much smaller than the viscous sublayer, pressure forces and viscous forces are of about the same magnitude, so that the presence of roughness makes little difference in the overall resistance to flow. If the elements are much larger than the potential thickness of the viscous sublayer, however, Reynolds numbers of local flow around the elements are large enough that pressure forces on the elements are much larger than viscous forces, and then the roughness has an important effect on flow resistance.

The aforementioned are summarized in 2.4
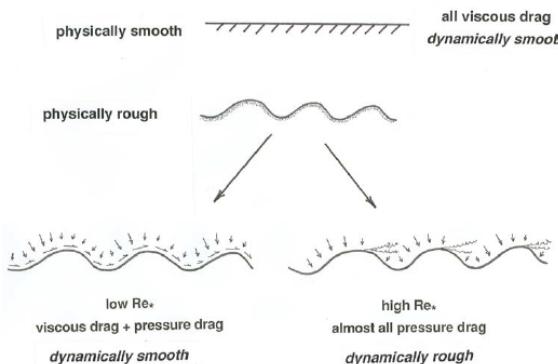
Figure 2.4: Differences in near-bed flow and forces in flow over a rough boundary, as a function of the roughness Reynolds number Re*. (adjusted from Southard (2006))

Velocity profiles

This section will focus on treatment of velocity profiles in turbulent boundary-layer in open channel flows. Knowledge of such flows is important for choosing an appropriate model for stone stability. Two velocity profiles with be discussed, one will follow the law of wall for smooth boundaries and one will follow the law of the wall for rough boundaries.

In both cases, the inner layer(viscous sublayer and buffer layer) and the outer layer are dominated by different mechanisms ((Southard, 2006)). Within the inner layer, the velocity profile is being controlled by local effects (strong viscous shear and intense small scale turbulence respectively) and is considered to be independent of the nature of the turbulence in the rest of the flow, all the way up to the free surface. In this sense, the velocity profile is independent of the water depth d. In the outer layer, the velocity profile is dependent on water depth d, as the large eddies are a significant proportion of the water depth. Viscous stresses and the height of the roughness elements is considered to play no role. Finally, there should be a region is the middle where the two layer characteristics overlap.
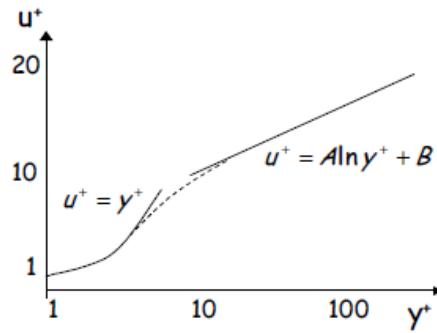
Figure 2.5: Dimensionless mean flow velocity vs. dimensionless distance from boundary for the inner layer over a smooth boundary. (adjusted from Uijttewaal (2002))

In the case of a **dynamically smooth boundaries**, figure 2.5 represents the law of the wall. The constants A and B, are usually taken to be equal to 2.5 and 5.1 respectively. The mean velocity and the distance from boundary are made dimensionless with:

$$u^+ = \frac{\overline{u}}{u_*} \tag{2.8}$$

and

$$y^+ = \frac{\rho u_* y}{\mu} \tag{2.9}$$

For $y^+ < 5$ the velocity profile lies in the viscosity dominated region whereas for $y^+ > 30$, the viscous shear stresses are negligible. For $5 < y^+ < 30$, there is a smooth transition between the viscosity dominated and the turbulence dominated profile.

The thickness of the inner layer varies with the Reynolds number, but it occupies only a small percentage of the flow depth.

Strictly speaking, the law of the wall is not valid for highly variable flows like those discussed in this thesis , as locally the logarithmic part of the velocity profile might be smaller, at another height or even be absent. Nevertheless, in practice also for these cases the law of the wall is used because it still will provide valuable insight in the general flow characteristics over the rough bottom. In fact the law of the wall has quite a large area of applicability, even in the case of the presence of substantial pressure gradients ((Southard, 2006)).

On the other hand, in case of **dynamically rough boundaries**, the velocity profile should also depend on the height of the roughness elements (relative to the viscous sublayer) and on the distance relative to them.

The latter is easily understood when considering all the wakes and the flow separation induced by the non-uniform individual elements. In that sense, it is expected that in distances of the same order of the rock size, the velocity profile changes spatially. Higher on the water column, as the effect of the roughness elements diminishes, turbulence structure is only dependent on local dynamics in analogy with the smooth boundaries.

By introducing the roughness length y_0, the velocity law in upper part of the inner layer reduces to the one in 2.6. Depending on the equivalent sand roughness ks, the flow could be transitionally rough or fully rough. Finally it can also be smooth, in which case we speak of a dynamically smooth, rough boundary. The above is summarized in figure 2.6.
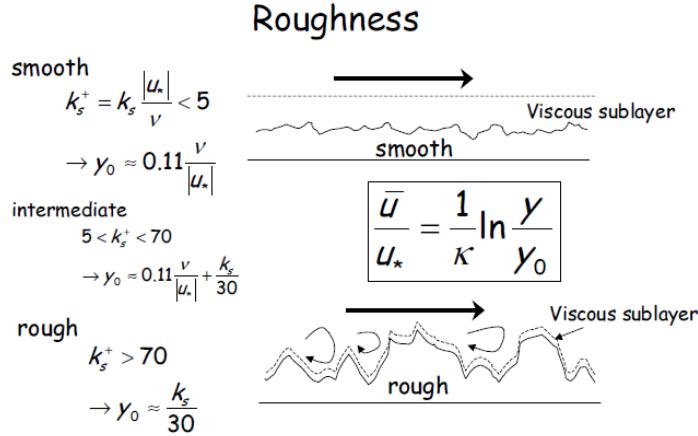
Roughness

Figure 2.6: Roughness limits (from Uijttewaal (2002))

2.1.4. Backward facing step

The case of open channel step flow is a fundamental case of geometry induced non-uniform flow. Since the present thesis deals with this type of flow, the basic flow patterns present in a Backward Facing Step (BFS) are given in short. Another such case, is the flow under a gate, which was used in section 1.2, to introduce the reader to the research topic.
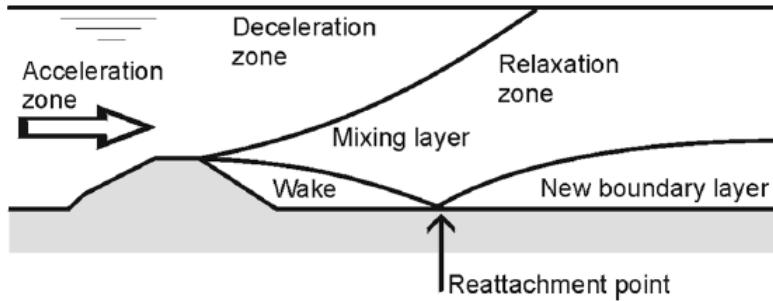
Figure 2.7: Overview of backward facing step zones (Verhagen (2016))

In figure 2.7, we suppose that a fully developed turbulent velocity profile approaches a step. An acceleration region is expected on top of the step and a deceleration region after that. In the acceleration region a favorable pressure gradient arises which is in flow direction. An opposite pressure gradient causes deceleration. In figure 2.8 we can see that the boundary layer thickness changes accordingly. The change is given by Schiereck and Verhagen (2012):

$$\frac{\delta}{x} = \frac{-(4 \sim 5)\delta}{u_0} \frac{du_0}{dx} \tag{2.10}$$
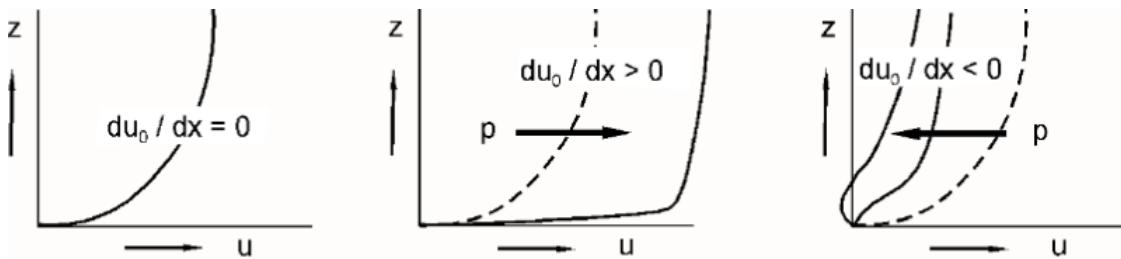
Figure 2.8: Influence of pressure gradient on velocity profile (Schiereck and Verhagen (2012))

That being said, in the acceleration the boundary layer becomes thin, and the velocity profile more full. The velocity gradient in the vertical direction becomes larger, leading to larger bed shear stress. In the deceleration zone behind the flow, the opposite happens. The boundary layer becomes larger with the appearance of flow separation. In this case the flow streamlines diverge and turbulence is expected to increase.

In figure 2.7 we can discern certain areas. These will be elaborated one by one and in the end the relevance to bed stability will be highlighted.

Mixing/shear layer

Right after the edge of the step, the uniform wall flow becomes free, with a shear layer development. Kelvin-Helmholz instabilities are generated. These instabilities roll up and form spanwise vortices. These vortices pair to form larger structures. They also become unstable over their rotational axis and develop into three-dimensional turbulence. (Hofland (2005))The mixing layer grows until the water column becomes fully mixed.

Recirculation zone

In between the mixing layer and the wall bottom, a recirculation region or gyre exists. In this area a lower speed than the water arriving from the step is expected(Nakagawa and Nezu (1987),De Gunst (1999), Hofland (2005)). According to literature the length of this zone is estimated to be 5-8 times the step height (Nakagawa and Nezu (1987), Bradshaw and Wong (1972)). In addition a velocity of 0.3 times the main stream is expected (Uijttewaal (2002)). The transfer or momentum between the main stream and the gyre is governed by the large eddies in the mixing layer in between (Uijttewaal (2002)).

In the reattachment point where the flow hits the bottom high pressures are expected. Upstream of the reattachment point the flow is forced in opposite direction from the mainstream due to the pressure gradient present. At the reattachment point flow structures with a size of the order of the step height are observed. (Hofland (2005))

New boundary layer

Downstream of the reattachment point, a new boundary layer starts to develop and eventually a new equilibrium log-law profile is reached. The recovery of the profile to a uniform one can take more than 50 step heights(Nezu and Nakagawa (1989)). The turbulence intensity and shear stresses decrease in this zone.
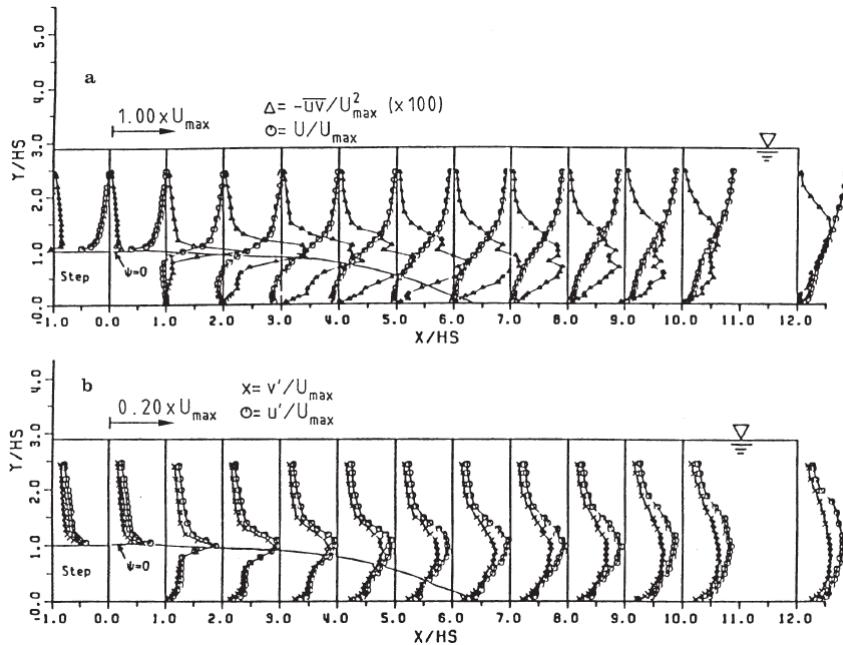

Figure 2.9: Distribution of U, turbulence intensities u',v' and Reynolds shear stress - $\overline{uv}$ in a backward facing step (Nezu and Nakagawa (1989))

In figure 2.9, results of an experimental campaign of Nezu and Nakagawa (1989) are shown. It can be seen that 10 step heights after the step, the profile has not yet recovered (upper plot). The mixing layer and the tendency to smoothen the induced gradients and revert to uniform flow are shown (upper and down plot). In upper plot of figure 2.9, it can also be seen that the reattachment point is at around 6 step heights downstream the step.

Relevance with stone stability

To calculate stone stability it is important to estimate the location of the reattachment point as well as the recovery rate of the velocity profile after that. Concerning the former, it is often realized that the reattachment point lies 5-8 times the step height, downstream of the step as stated above. It must be noted that in this point, where the highest damage is expected, the mean velocity is zero leading to zero damage if the conventional formulas are used (Hofland (2005)). In Nakagawa and Nezu (1987) it is reported that higher Froude numbers seem to increase the reattachment length. In order to calculate the necessary stone size in bed protections used near step flows, equation 2.11 can be used to estimate the decay of turbulence intensity r after the reattachment point (Schiereck and Verhagen (2012)):

$$r(x) = \sqrt{0.5 k_0 [1 - \frac{D}{H}]^{-2} [\frac{x}{\lambda} + 1]^{-1.08} + 1.45 \frac{g}{C^2}} \qquad (2.11)$$

where λ is a relaxation length, ($\lambda \approx 6.67 H$), k_0 is the relative turbulent energy in the mixing layer and D is the step size. In equation 2.11, the first multiplier in the first term represents the initial turbulence by the sill, the second multiplier represents the turbulence decay over the distance x (downstream of the reattachment point) and the second term the turbulence for uniform flow conditions.

2.2. Numerical Modelling

As already mentioned, the choice of modelling technique is immediately linked to the stability formula to be derived. The information available in a numerical model is then translated in a mathematical form.

In this section, spacial attention is paid to the numerical aspects of modelling methods relevant to the application of the present research. The applicability of these method on stone stability and past numerical studies are discussed. These methods are:

1. Direct Numerical Simulation (DNS)
2. Large Eddy Simulation (LES)
3. Detached Eddy Simulation (DES)
4. Reynolds-Averaged Navier-Stokes (RANS)

2.2.1. Past numerical studies

DNS

DNS is the method that solves the unsteady 3D Navier Stokes equations numerically, without introducing any model. In such an approach all scales of the turbulent motion from the largest ones down to the smallest, dissipative scales must be resolved. Due to the very fine grid size and time step, even at medium Reynolds numbers and for simple flows, the computing effort is enormous. More specifically, for a domain of dimension L, the number of grid points needed is on the order of magnitude $N_g \approx \dfrac{L}{\lambda_{kolm}} \approx Re^{9/4}$. This means that for Re=1000, already 6 million grid points are needed (Uijttewaal (2002)). The Reynolds number that the current study has are of the order of magnitude 200000. However, it is a very useful tool for studying the details of turbulence at low Reynolds numbers as the complete information on all details of the turbulent motion can be extracted from such simulations. In the present topic, to the researcher's knowledge, no DNS simulation has been undertaken specifically designed to serve the purposes of the creation of a new stability formula. However, fundamental studies with DNS for flows above rough surfaces are available. An example of that is the work of Singh et al. (2007), where a DNS study of turbulent flow above a fully rough bed ($k_s > 70$) is undertaken. It is worth noting that the rough bed was represented by identical spheres positioned in the channel bed. The corresponding Reynolds number was approximately 3000 and 67 million cells were needed to reach a grid resolution of $\Delta x^+ = 3.6$ and $\Delta y^+ = \Delta z^+ = 4.2$. It can be then understood that the large Reynolds number engineering flows that the present thesis is dealing with are far from suitable for DNS studies.

RANS

Next, RANS simulations will be discussed. In that case, turbulent fluctuations are averaged out and only equations governing mean-flow quantities are solved. Splitting up the instantaneous flow quantities into mean and fluctuating values and then averaging the non-linear original Navier Stokes equation leads to the appearance of correlations between velocity fluctuations, which act like stresses on the mean flow and are called turbulent or Reynolds stresses. These terms are unknown and must be described by a model before the mean-flow equations can be solved. Due to their low cost, these kind of simulations are most widely used.

In Steenstra et al. (2016), a 2D RANS model, along with the k-ω turbulence model was used. A ligid lid assumption was chosen for the free surface. The numerical model was validated with experimental results of Jongeling et al. (2003). The validation process revealed the limitation of the RANS modelling approach: averaged velocities deviated in the order up to 10% from the measurements while the error in the turbulent kinetic energy could even be of the order of 50% or more.

Also in Jongeling et al. (2003), a 2DV RANS code along with k - ϵ model was used. In addition to the previous case, comparison with experimental data revealed agreement only in case of uniform flow over a flat bed.

Supposing that RANS results of mean motion agree well with experimental results of rough non uniform flows, still they provide information only on the mean flow characteristics. However, as stated in section 2.1.1, the initiation of motion in stability arises from extreme forces.

It is worth noting, that many more advanced turbulence closure models other than the ones mentioned above are developed, that are modified to predict the near wall boundary layer of interest in a more accurate way. As an example, the numerical model developed in Fuhrman et al. (2011) is noted. In this study, a model is proposed that solves the incompressible RANS equations coupled with the $k - \omega$ turbulence closure model, modified in a simple way to incorporate anisotropy in turbulent normal stresses. The model is applied on oscillatory wave boundary layers on spatially varying bottom roughness (roughness transition).

IDDES

Lastly in Stevens (2018), for the first time an eddy resolving technique was used. Resolving the turbulent eddies enabled the use of local flow parameters instead of depth-averaged flow characteristics, because the extreme forces on the bed can be determined. Therefore, the stability parameter derived included local parameters near the bed. For that case the DES method was used. Here again the near-wall region is calculated by RANS and regions away from the wall and particular in separated flow regions by LES. In Stevens (2018) it is mentioned that the large anisotropic turbulence, important for the specific application, scales are expected to be resolved instead of modelled. However, for the stone stability at the place of interest i.e. near the bottom, the turbulent quantities are modelled. To get an idea of the status quo in modelling these hydrodynamics, two plots representing the improvement of an eddy resolving technique in non-uniform flow compared to a RANS, is depicted below.
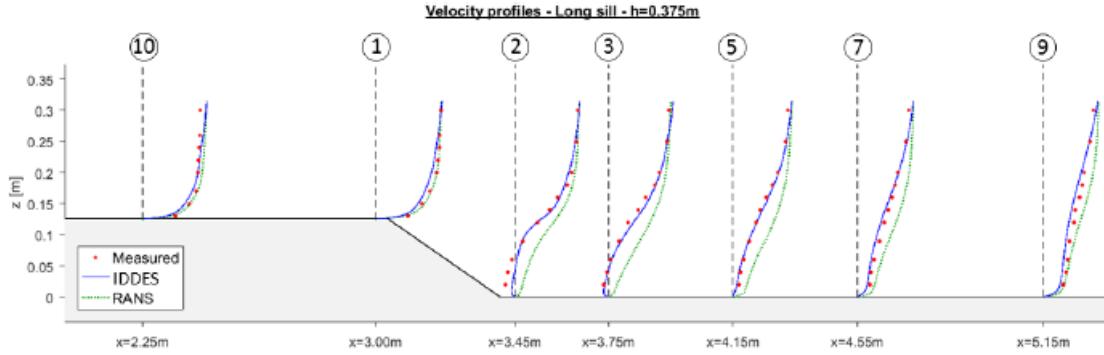
Figure 2.10: Averaged measured and simulated profiles of the velocity in x-direction ux. (adjusted from Stevens (2018))
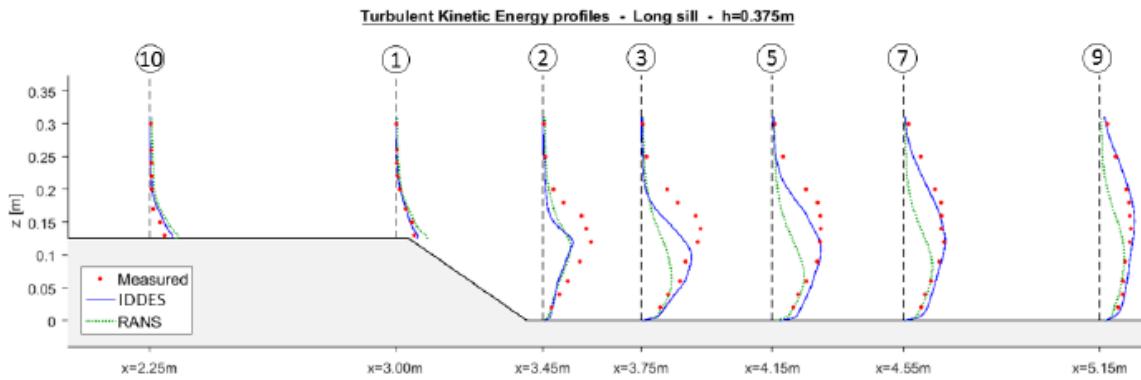
Figure 2.11: Averaged measured and simulated profiles of the total TKE. (adjusted from Stevens (2018))

In Stevens (2018) it was concluded that applying the IDDES method in the long sill case of Jongeling et al. (2003), the simulated averaged velocity profiles are in good agreement with the measurements since the mean deviation between the simulated and measured velocities was in the same order of magnitude as the measuring error. The largest deviations were unfortunately observed in the area of interest for this thesis, namely near the bottom and the shear layer. The simulated averaged TKE profiles of the IDDES also deviated from the measurements.
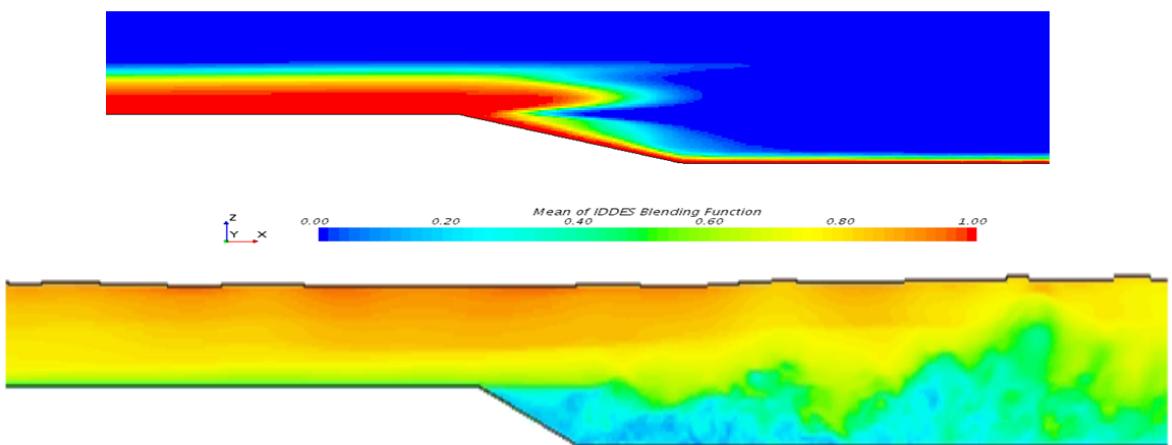
Figure 2.12: Upper plot: Impression of RANS and LES regions in IDDES. Lower plot: Instantaneous velocity profile in x-direction. (adjusted from Stevens (2018))

Taking a closer look at figure 2.12 from Stevens (2018), the areas where the flow is solved with RANS and LES (red and blue regions respectively) are discerned. It can be realized that in the area above the sill (acceleration region) RANS region dominates. That means that both the wall turbulence above the sill and the initiation of the mixing layer after the step lie in the RANS region where only mean flow characteristics are solved. In addition, in the RANS region, an interface exists between the wall function used and the RANS flow region. After that, an interface exists between RANS and LES region. Sweeps come from the outer region only to get damped quickly in the RANS region. Ejections are not resolved because in the RANS near wall region no production of energy is at place. In Stevens (2018), is was recommended that more investigation is needed for the flow transition between these regions.

In Stevens (2018), also attention was paid to the resolved and modelled flow scales, relevant for stone stability. As already discussed in section 2.1.1, the low frequency drag fluctuations cause the largest forces on the stones. However the total force caused by these low frequency drag fluctuations can be increased temporarily by high-frequency turbulence wall pressures. This combination gives the higher extreme forces responsible for the stone instability. TWP with wavelengths of roughly 1.5d are expected to have a large influence on the fluctuations forces (Hofland (2005)).

From the above, it is understood that scales up to the size of the stones are important for bed stability. In figure 2.13 the energy density spectrum of the IDDES model is depicted. It can be seen, that the red line of the simulated velocity signal, follows the blue line quite accurately, until a frequency of about 2 to 3 Hz, were it starts to drop.
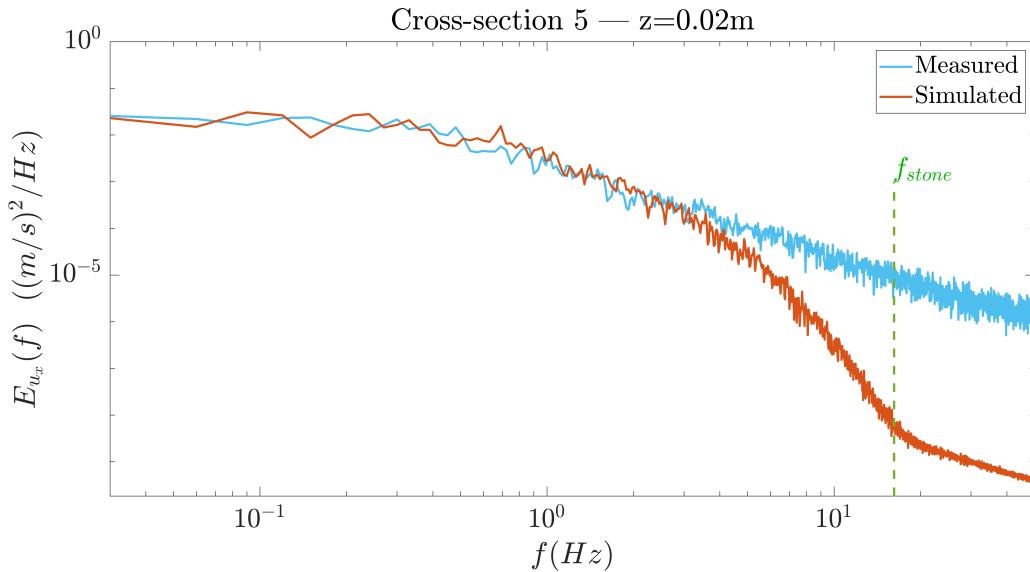
Figure 2.13: Variance density spectrum of ux on double-logarithmic scale(from Stevens (2018))

The basic idea in LES that was also followed by Stevens (2018), is that the modelling part of the eddies will begin when there is no anisotropy in the eddies anymore (reach of inertia sub-range or -5/3 slope), as suggested in literature (see Rodi et al. (2013) and section). By computing the Taylor microscale by $L_{tms} \approx Re^{-0.5}$, the resulting length scale was 2.24 mm. However due to computational limitations, the grid size in the model was 5 mm. The corresponding frequency expected to be reached with this 5 mm grid, was calculated to be 25 Hz by:

- assuming that at least 2 grid cells are needed to resolve one eddy.
- using the local mean u_x velocity as a velocity scale
- the time scale of the eddies to be resolved is $T_{exp} = \dfrac{2L_{grid}}{\overline{u}_x} \approx 0.04s$
- calculating the expected resolution as $f_{exp} = \dfrac{1}{T_{grid}} \approx 25Hz$

In correspondence, the frequency required to reach the length scale of a rock was calculated by $f_{stone} = \frac{1}{T_{stone}} = \frac{\overline{u}_x}{d_n^{50}}$ to 16 Hz.

As mentioned above, the achieved resolution was 2 Hz, substantially smaller than the expected one. In Stevens (2018), this is attributed to the anisotropy that small scales have, which are assumed homogeneous and isotropic.

Finally, having the indication (see figure 2.12) that the initiation of motion might not be captured as good as possible in the IDDES model, further investigation of numerical results of Stevens (2018), is undertaken. More specifically, energy density spectra are calculated for cross section 3, 0.20 m above the wall bottom, in the mixing layer region (see figure 2.11). As can be seen from figure 2.14, there is a large mismatch between the simulated and measured energy. This is also evident from cross section 3 from figure 2.11. This leads to the conclusion the the performance of this model to the mixing layer, has room for improvement.
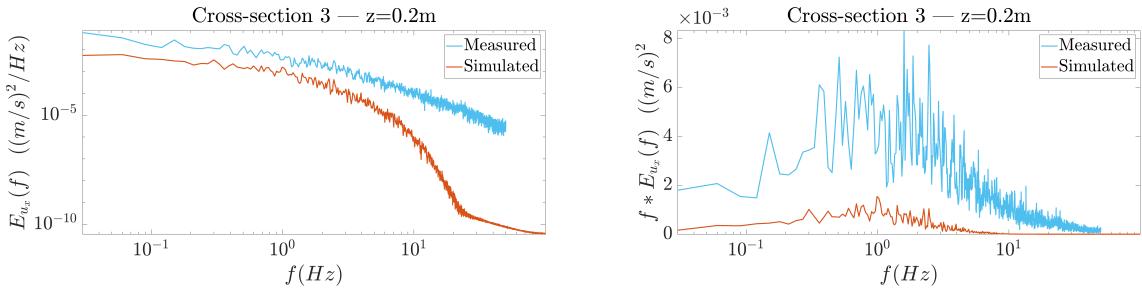
Figure 2.14: Left plot: Spectral Density E(f) in double logarithmic scale. Right plot: Premultiplied Energy density spectrum in semilogarithmic scale (Data retrieved from Stevens (2018))

2.2.2. Large Eddy Simulation

In this section, the concept of large eddy simulation is given. This method has not yet been used for the purpose of formulating a stability formula. Since this will be the main modelling technique implemented for numerical modelling in this thesis, the governing equations in LES and other numerical aspects concerning LES are presented below. Since OpenFOAM will be the code to be used for numerical modelling (see also appendix B), the implementation of LES model in OpenFOAM is particularly of interest.

The main idea behind LES is that once the large structures are broken up into the smaller scales via the energy cascade, they become more isotropic and lose their energy in self-similar processes that are not much affected by the large scale geometry. So, if we are able to resolve the large-scale part of the energy spectrum on our numerical grid, the remaining isotropic small scale turbulence is less of a problem to model. This implies than we must resolve all the flow structures until the inertial subrange is reached (Sagaut (2006),Rodi et al. (2013)). To achieve that, in LES the original Navier-Stokes equations are filtered spatially. The turbulent motion is separated into larger scales that are resolved and to smaller scales that are modelled with a sub-grid model.

Concerning the specific application, LES could prove to be less expensive than DNS, but still quite computationally intense for high Reynolds number flows. That is because near the walls the length scale of turbulence decreases with increasing Re so that the number of grid points required to resolve adequately the near-wall zone increases approximately with Re^2. More specifically, in Piomelli and Balaras (2002) , a constant grid spacing in recommended to resolve the inner region with grid sizes in streamwise and spanwise directions as $\Delta x^+ \approx 100$ and $\Delta y^+ \approx 20$. In Sagaut (2006), somewhat more strict requirements are presented indicating $\Delta x^+ \approx 10 - 80, \Delta y^+ \approx 5 - 30, \Delta z^+ \approx 2 - 3$. In practice, usually the first grid point is placed in the zone $(0 < z^+ < 1)$.

On the other hand, the number of grid points required to resolve the outer layer scales with Re^0.4 (Sagaut (2006),Piomelli and Balaras (2002)). In this case, the first grid point is place in the log-layer 30<z<200.That being said, a solution for simulating high Reynolds number flows could be a wall-modelled LES. This is further explained in section 2.2.3. The basic idea is illustrated in figure 2.15.
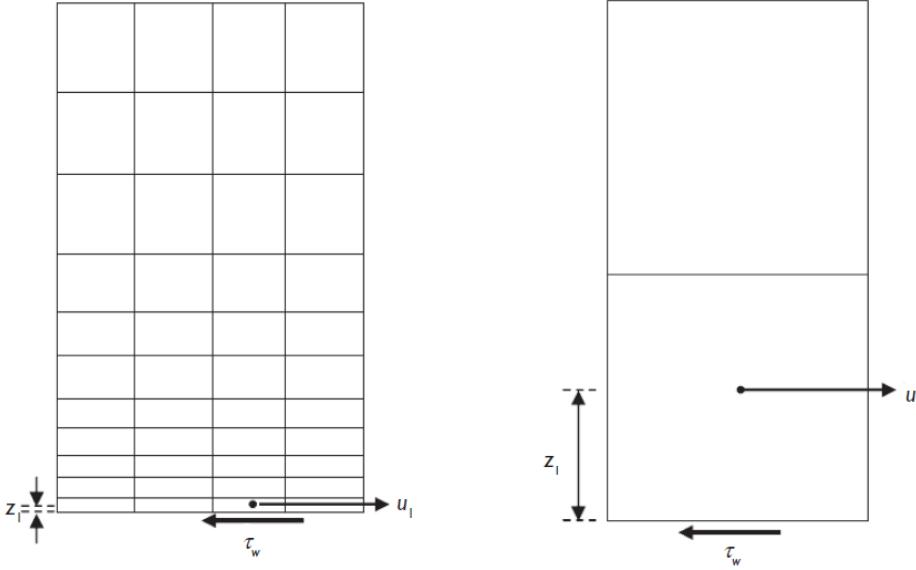
Figure 2.15: The difference between Wall-Resolved LES (left) and Wall-Modelled LES (right) (from Rodi et al. (2013))

Governing equations

In the LES approach, small scale motion is removed by spatial averaging or filtering. Local quantities are split into resolved (or filtered) quantities $\overline{f}$ and deviations from these f' (or sub-grid or residual quantities):

$$f = \overline{f} + f' \tag{2.12}$$

Depending on the way the smaller scales are removed from the larger ones, the LES can be classified as:

1. Implicit LES (spatial averaging approach)
2. Explicit LES (use of a filter function)

In OpenFOAM, LES with the implicit filtering is implemented, in which only the filter width is specified and the filter shape is not. In this case, the removal of the small-scale motion and hence the averaging is performed mostly by the numerical grid, as on a given grid only motions with scales larger than the mesh size can be resolved; the others fall through the mesh, and the quantity that is calculated is an average over the control volume formed by the grid (Schumann (1975)). On the other hand, with explicit filtering a separate filter function is introduced with a filtered width Δ. This is not the practice followed in this thesis. An extent discussion on this option is given at Sagaut (2006) and Pope (2001).

Applying the filter operation to the Navier-Stokes equations leads to the following filtered equations:

$$\frac{\partial \overline{u_i}}{\partial x_i} = 0 \tag{2.13}$$

$$\frac{\partial \overline{u_i}}{\partial t} + \frac{\partial \overline{u_i u_j}}{\partial x_j} = -\frac{1}{\rho}\frac{\partial \overline{p}}{\partial x_i} + \frac{\partial}{\partial x_j}(\nu\frac{\partial \overline{u_i}}{\partial x_j}) - \frac{\partial \tau_{ij}^{SGS}}{\partial x_j} + \rho g \tag{2.14}$$

where

$$\tau_{ij}^{SGS} = \overline{u_i u_j} - \overline{u_i}\,\overline{u_j} \tag{2.15}$$

In the above equations the space vector is defined as $x_i \equiv x_1, x_2, x_3$, and the velocity vector as $u_i \equiv u_1, u_2, u_3$.

The term τ_{ij}^{SGS} in equation 2.15, represents the effect of the small scale motion to the resolved motion and introduces the subgrid-scale stresses in the equation. These stresses need to be modelled by a subgrid-scale model. In the limit of a small mesh spacing $\Delta \to 0$ and also $\tau_{ij}^{SGS} \to 0$; a DNS solution is then returned.

It can be realized that in implicit LES, the SGS model and hence the final results, depend on the grid size, which determines the limit between resolving and modelling. As the discretization is refined, the solution approaches the DNS one. However in practice this is not reached. The aim in the LES is often to resolve scales up to the point that the inertial sub-range is reached and only the dissipative motion is modelled (Rodi et al. (2013)). In the current thesis, grid refinement is done as much as could be afforded, keeping in mind the inertial subrange limit.

Subgrid-scale model

In this section, the subgrid-scale models used in this thesis are elaborated. Focus is on the implementation of this models in OpenFOAM. Mathematical implementation is given according to Fumiya Nozaki's CFD Blog (Nozaki (2019)) and OpenFOAM v.1812 user's guide and source code.

The Smagorinsky subgrid scale (SGS) model was developed by Joseph Smagorinsky in the meteorological community in the 1960s (Smagorinsky (1963)). It is based on the eddy viscosity assumption, which postulates a linear relationship between the SGS shear stress and the resolved rate of strain tensor.

The sub-grid scale tensor is:

$$\tau_{ij}^{SGS} = \overline{u_i u_j} - \overline{u_i}\,\overline{u_j} = \frac{1}{3}\tau_{kk}\delta_{ij} + (\tau_{ij}^{SGS} - \frac{1}{3}\tau_{kk}\delta_{ij}) \tag{2.16}$$

where the sub-grid scale tensor is split is a isotropic part $\frac{1}{3}\tau_{kk}\delta_{ij}$ and an anisotropic part $\tau_{ij}^{SGS} - \frac{1}{3}\tau_{kk}\delta_{ij}$ in analogy with the Reynolds stress tensor in RANS approach.

Next, again just like in the RANS approach, the Boussinesq hypothesis can be introduced in order to model the deviatoric part of the sub-grid stress tensor. In this way the turbulent stresses are believed to behave formally as the viscous stresses:

$$\tau_{ij}^{SGS} = \overline{u_i u_j} - \overline{u_i}\,\overline{u_j} = \frac{1}{3}\tau_{kk}\delta_{ij} + (\tau_{ij}^{SGS} - \frac{1}{3}\tau_{kk}\delta_{ij}) = \frac{1}{3}\tau_{kk}\delta_{ij} - 2\nu_{SGS}dev(\overline{S_{ij}}) \tag{2.17}$$

In the above equation, $\overline{S_{ij}}$ is the resolved-scale strain rate tensor defined as:

$$\overline{S_{ij}} = \frac{1}{2}\left(\frac{\partial \overline{u_i}}{\partial x_j} + \frac{\partial \overline{u_j}}{\partial x_i}\right) \tag{2.18}$$

Finally given that the subgrid scale viscosity is defined as:

$$k_{SGS} = \frac{1}{2}\tau_{kk} = \frac{1}{2}(\overline{u_k u_k} - \overline{u_k}\,\overline{u_k}) \tag{2.19}$$

Equation 2.21 becomes:

$$\tau_{ij}^{SGS} = \overline{u_i u_j} - \overline{u_i}\,\overline{u_j} = \frac{1}{3}\tau_{kk}\delta_{ij} + (\tau_{ij}^{SGS} - \frac{1}{3}\tau_{kk}\delta_{ij}) = \frac{1}{3}\tau_{kk}\delta_{ij} - 2\nu_{SGS}dev(\overline{S_{ij}}) = \frac{2}{3}\tau_{kk}\delta_{ij} - 2\nu_{SGS}dev(\overline{S_{ij}}) \tag{2.20}$$

The turbulent viscosity is then computed from the following equation, that follows the principle already adopted in RANS where the viscosity scales with a length scale and velocity:

$$\nu_{SGS} = C_k \Delta \sqrt{k_{SGS}} \tag{2.21}$$

where $C_k = 0.094$ is the default value.

The remaining part is the calculation of the sub-grid kinetic energy. In Smagorinsky, this is calculated under the assumption of the balance between the subgrid scale energy production and dissipation (local equilibrium):

$$\overline{S} : \tau_{ij}^{SGS} + C_\epsilon \frac{k_{SGS}^{1.5}}{\Delta} = 0 \tag{2.22}$$

After some manipulation, the subgrid scale viscocity is given by:

$$\nu_{SGS} = (C_s \Delta)^2 \sqrt{2\overline{S_{ij}\,S_{ij}}} \tag{2.23}$$

The only constant needed is the Smagorinsky constant C_s and is usually given between 0.1 and 0.2. In OpenFOAM the default value is 0.168.

An important shortcoming of the Smagorinsky model is that ν_{SGS} as predicted by equation 2.23 does not reduce to zero in the viscous sublayer, in which turbulent fluctuations should be damped as impermeable surfaces, e.g. walls, are approached. This is due to the fact that large velocity gradients prevail in the boundary layer and result in high values of the rate of strain S . Hence, the turbulent eddy viscosity ν_{SGS} needs to be damped near impermeable surfaces by a damping function. The most popular of such functions was proposed by Driest (1956).

In addition, the kinetic energy is transferred only from large resolved scales to small scales, i.e. the Smagornisky model is strictly dissipative and does not allow for a backscatter of energy from small unresolved scales to large scales.

In the dynamic procedure the coefficients of the Smagorinsky SGS model are determined as part of the calculation, based on the energy content of the smallest resolved scales, rather than a priori input as in the Smagorinsky model.

The introduction of dynamic models has caused significant progress in the sub-grid scale modelling of transitional flows and has resolved many of the problems encountered with traditional "static" models. In free shear and channel flows the dynamic model automatically adjusts, by lowering the coefficient in areas of high shear and near the walls, a function that is normally performed by the van Driest damping function. Another advantage is that the eddy viscosity automatically goes to zero in laminar regions of the flow(Rodi et al. (2013)).

The Wall-Adapting Local Eddy viscosity model (WALE), firstly introduced by Nicoud and Ducros (1999), is an eddy-viscocity model like Smagorinsky, with the difference that it can account for the wall effects without a separate employing of a wall damping function (eg. van Driest in Smagorinsky). Like in Smagorinsky, the sub-grid scale viscosity is computed through the sub-grid turbulent kinetic energy. The latter one is computed from:

$$k_{SGS} = \left(\frac{C_w^2 \Delta}{C_k}\right)^2 \frac{\left(S_{ij}^d S_{ij}^d\right)^3}{\left(\left(\overline{S_{ij}\,S_{ij}}\right)^{5/2} + \left(S_{ij}^d S_{ij}^d\right)^{5/4}\right)^2} \tag{2.24}$$

where $\overline{S_{ij}}$ is the resolved-scale strain rate tensor and S_{ij}^d, the traceless symmetric part of the square of the velocity gradient tensor.

Substituting 2.24 to 2.21 , the expression of subgrid scale viscocity ν_{SGS} is acquired:

$$\nu_{SGS} = (C_w \Delta)^2 \frac{\left(S_{ij}^d S_{ij}^d\right)^{3/2}}{\left(\overline{S_{ij}\,S_{ij}}\right)^{5/2} + \left(S_{ij}^d S_{ij}^d\right)^{5/4}} \tag{2.25}$$

A model slightly different than the Smagorinsky model discussed in the previous, is the one equation eddy viscosity SGS model. The two models differ in the calculation of the subgrid scale kinetic energy k_{SGS} (equation 2.19); the Smagorinsky model assumes the local equilibrium to compute k_{SGS}, while the one equation eddy viscosity model solves a transport equation for k_{SGS}. In the original model of Yoshizawa (1982), the transport equation is determined as:

$$\frac{\vartheta \rho k_{SGS}}{\vartheta t} + \frac{\vartheta \rho \overline{u}_j k_{SGS}}{\vartheta x_j} = \frac{\vartheta}{\vartheta x_j}\left[\rho(\nu + \nu_{SGS})\frac{\vartheta k_{SGS}}{\vartheta x_j}\right] + 2C_V\Delta k_{SGS}^{1/2}\overline{S}_{ij} - C_\epsilon\frac{k_{SGS}^{3/2}}{\Delta} \tag{2.26}$$

where C_V and C_ϵ are model constants. In equation 2.26, the first term is the time derivative, the second term is the convective term, the first term on the right hand side is the diffusion term, the second term is the production term and the last on the dissipation. In the case of the Smagorinsky SGS model, only the production and dissipation terms are taken into account with the assumption of the local equilibrium.

An important advantage of the one eddy model is the fact that it allows for backscatter without destabilization of the numerical solution procedure, because the k-equation requires an SGS energy balance (Rodi et al. (2013)). On the other hand, in one-equation models it is necessary to solve one extra transport equation, which makes the model computationally more expensive.

Generating turbulence at the inlet

In unsteady simulations (DNS, LES, DES) the challenge is particularly pronounced at the inflow boundary of spatially developing turbulence simulations for which the accurate prescription of the incoming turbulent eddies as a function of time is a prerequisite to obtaining the unsteady solution in the interior of the domain (Wu (2017)). In this thesis special attention is paid is that feature. Some possibilities within OpenFOAM are presented below.

Random Velocity fluctuations

This method creates random velocity fluctuations in every discrete point with a specified amplitude. An example of the correspond boundary condition in the inlet patch in OpenFOAM is:

```
inlet
  {
      type            turbulentInlet;
      fluctuationScale (0.14 0.05 0.05); // RMS fluctuation scale (fraction of mean)
      alpha           0.05; //fraction of new random component added to previous|
      referenceField  uniform (7.72 0 0); // reference (mean) field
      value           uniform (7.72 0 0); //placeholder
  }
```

It has been seen that the turbulent fluctuations generated with this methods are specially and temporally uncorrelated. As a results they die out quickly and therefore this methods is not suitable for the purpose of these simulations.

Recycling method

In this method, the inlet and the outlet boundaries of the domain are cyclic. The flow field at the outlet is prescribed in the inlet. In this way, instantaneous flow fields are prescribed every time in the inlet. Correlated turbulence fluctuations are inserted in the domain. However, this method demands the extension of the domain in upstream/downstream direction, since it is only applicable to fully developed stationary flow. Rescaling is needed in case the geometry changes along the domain. This method could prove also computationally expensive since the domain is enlarged. More details on this method can be found in Wu (2017).

Precursor simulation

Maybe the post popular method of generating turbulence at the inlet is employing a precursor simulation. More specifically, a separate simulation is build with periodic boundary conditions. Next, the flow field is extracted in several time steps. The sampling time should be in accordance to the realistic turbulent structured expected to be generated by the specific flow field. In OpenFOAM the set up of a periodic simulation is relatively easy. The sampling patch later to be inserted in the main simulations is easily extracted from putting in the `controlDict` folder something like:

```
sampledSurface
{
    type          surfaces;
    writeControl  writeTime;
    surfaceFormat boundaryData; //output format style
    interpolationScheme none;
    interpolate false;
    triangulate false;
    fields
    (
        U UPrime2Mean nut p
    );
    surfaces
    (
        middle_surface{
            type plane;
            planeType  pointAndNormal;
            pointAndNormalDict
            {
                point (1.5 0.0 0);
                normal (1 0 0);
            }
        }

    );
}
```

After the necessary fields are created, they can be place in the `constant` file folder. The inlet condition of the main simulation is specified as:

```
inlet
{
    type          timeVaryingMappedFixedValue;
    mapMethod     nearest;
    offset        constant (0 0 0);
}
```

The main disadvantage of this method is that it is computationally expensive. In addition, for the simulating case of the thesis, where was not a cross section with a fully developed velocity profile that the output of a precursor simulation could be set. That is why this method was not selected for the numerical modelling of this thesis

Synthetic Turbulence Generation

Multiple synthetic turbulence generation methods have been proposed in the last years. However, to the writer's notice, few options are already implemented in OpenFOAM. The one used in the present thesis is described in Poletto et al. (2013). In this work, the challenge of moving from a RANS region to an LES is addressed. More specifically, one must superimpose physically representative instantaneous turbulent fluctuation in the mean velocity profile obtained by the RANS region, in order to move to the LES region. As mentioned in the previous, superimposing random fluctuations is not sufficient. Efforts to impose space correlated turbulent fluctuations to arrive to a realistic turbulent state, include the works of Lund et al. (1998) and Benhamadouche et al. (2006). It is stated at Poletto et al. (2013) that the main challenge with these methods is that they are two-dimensional methods that suffer drawbacks from the requirement that stream-wise fluctuations were generated by an altogether separate equation, thereby being uncorrelated with the other components.
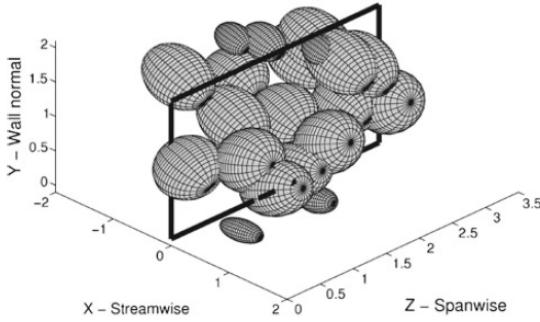
Figure 2.16: Eddies convected across the inlet plane by the DFSEM method. Each spheroid represents the spatial region influenced by the perturbations of a single eddy (from Poletto et al. (2013)).

In the work of Jarrin et al. (2009), a different approach to the problem is presented where fluctuations are imposed by eddies convected through a virtual volume. This method was based on a three-dimensional correlation of fluctuations with a predefined shape function. More specifically, synthetic eddies, each of which represents a set of velocity fluctuations, are convected through a box that entirely surrounds the inlet plane upon which a turbulent velocity field is required. These eddies, which are defined by their center and a formulation for the velocity fluctuation distribution around it, are convected at each time step by the locally imposed mean velocity (see figure 2.16). Once they have traversed and exited the box they are regenerated at a random location on the box inlet plane. The SEM proposed by Jarrin et al. (2009) defined the velocity fluctuations according to the following:

$$u_i'(x) = \frac{1}{\sqrt{N}} \sum_{k=1}^{N} \alpha_{ij} \epsilon_j^k f_\sigma \left(\frac{x - x^k}{\sigma^k} \right)$$

(2.27)

where N is the number of eddies introduced into the SEM domain, x^k is the location of the center of the kth eddy, σ^k is the turbulence length scale calculated at the eddy center, f_σ is a suitable shape function, ϵ_j are random numbers with zero average and α_{ij} are the Lund coefficients as defined in Lund et al. (1998). In Poletto et al. (2013) it is argued that although this formulation does allow any desired Reynolds stress field to be prescribed, the velocity field will not, in general, also satisfy continuity. To obtain a divergence free method the original SEM is applied to the vorticity field which is then transformed back to the velocity field by taking the curl of it. Lastly, the reproduction of turbulence anisotropy is ensured by defining a different length-scale, σ_i, in each of the coordinate directions x_i, and allows a different shape function to be associated with each direction. A new version of equation 2.27 in then proposed where the turbulence anisotropy and the divergent free constraints are met. Sensitivity test are undertaken, by using data coming from a DNS experimental set. However it is stated that tests using data from a RANS model have led to similar conclusions. From comparing the numerical results of Poletto et al. (2013) study with other SEM methods and by the experimental ones it is concluded that this boundary condition would be able to :
- impose a divergence free velocity field
- reproduce almost any possible state of Reynolds stress anisotropy
- decrease the required development region downstream of the inlet in a standard LES case, significantly decreasing the computational demands

As far as the implementation of this method in OpenFOAM is concerned, first the RANS data are stored in a RANS precursor simulation as described in the previous section:

```
sampledSurface
{
   type         surfaces;
   writeControl  writeTime;
   surfaceFormat boundaryData; //output format style
   interpolationScheme none;
   interpolate false;
   triangulate false;
   fields
   (
      U turbulenceProperties:R
   );
   surfaces
   (
      middle_surface{
          type plane;
          planeType  pointAndNormal;
          pointAndNormalDict
          {
             point (1.5 0.0 0);
             normal (1 0 0); //normal is the streamwise
          }
      }

   );
}
```

Apart from U and R fields a turbulent length scale L is needed. This can be generated through a eg. python script using the definition of turbulent length scale depending on the turbulent model used.

Finally, the inlet boundary condition of the LES simulation is defined as:

```
inlet
{
    type            turbulentDFSEMInlet;
    value           uniform (0.5311 0 0);
    delta           0.1875; // a domain-based length scale, e.g. the channel half-height
    mapMethod       nearestCell;
}
```

It must be noted that a new synthetic turbulence generation method for LES/DES appear is OpenFOAM verion 1906, based on the Digital-Filter Method (DFM). This is not analyzed here or tested in this work, since it was released by the end time of this thesis.

2.2.3. Near-wall treatment when modelling rough boundaries in LES

In engineering applications where the near-wall flow is important, two different but coupled parameters should be considered. First one is whether the turbulent boundary layer is modelled or resolved. The second one is how the boundary is embedded in the numerical model. In case of smooth walls, this is not much of a problem. However in rough boundaries, like granular beds, this is not trivial.

Because of steep gradients and strongly reduced eddy sizes near a boundary, high numerical resolution is necessary. Similar to flow over smooth walls, specification of the wall shear stress or some a-priori knowledge of the velocity profile over the rough wall is needed. This by itself is not an easy task as the law of the wall for rough boundaries is still subject of ongoing research and several different formulations exist. Most common methods to account for modelling a rough boundary are discussed below.

Explicit resolution of roughness elements

One basic possibility to account for wall roughness is to resolve the flow around the individual roughness elements, specifying as boundary condition the no-slip condition at the walls of these elements. Fundamental studies that resolved the individual elements through the numerical grid in scale resolving techniques, revealed that the numerical effort required is extremely high.

Apart from that, two important disadvantages of this method are summarized in the following:

1. The detailed topology of the rough surface is usually unknown. That is why these studies usually concern flows over relatively simple and exact defined roughness elements like square bars or wavy walls. References for these studies that be found in Rodi et al. (2013) or Stoesser (2014).

2. The requirements in terms of grid resolutions to represent individual roughness elements (using ten or more points per roughness element of about 6 mm) are exceeding most current computing resources

These two reasons set this method to be not applicable for modelling granular bed protection in the LES framework.

An alternative to using body-fitted grids to explicitly resolve individual roughness elements is the Immersed Boundary Method (IBM). In that method,, the grid does not need to conform to the shape of the physical domain boundaries. The physical domain boundaries are immersed or embedded within the grid. Even in this method the numerical requirements are still large.

Momentum forcing

A more natural way to account for the turbulence producing roughness but also avoiding the expensive explicit resolution of roughness is to consider the rough bed in a spatially averaged sense. In the momentum forcing approach the effect of the roughness on the flow and turbulence above the rough bed over a predefined volume is simulated. The dispersive stresses are a result of spatially averaging the Navier-Stokes equations over a control volume in which the velocity profiles are heterogeneous in space due to the rough bed.

In work of Scotti (2006) a way is proposed to mimic the roughness within the framework of DNS/LES. The idea is to randomly place ellipsoids on a smooth wall aiming at imitating sandpaper roughness. A Cartesian grid is used overlying the roughness and the grid spacing is determined from the resolution requirements for an LES/DNS and not based on the size of the roughness elements, which can be larger or smaller than the grid spacing. This treatment reproduces the downward shift of the spatially averaged velocity profile on a Clauser plot as well as realistic spatially averaged turbulence statistics.
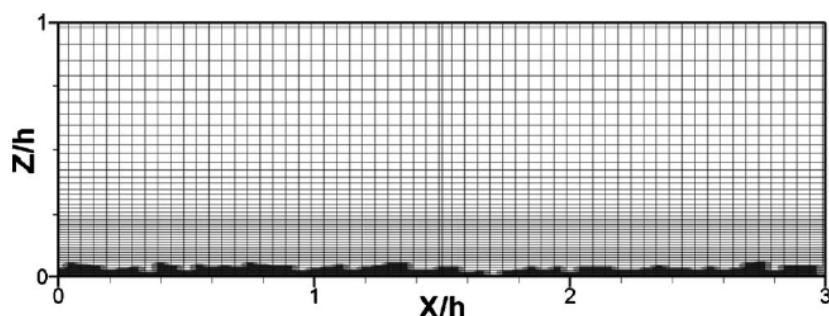
Figure 2.17: Longitudinal plane of the numerical grid including the embedded bed roughness. (from Rodi et al. (2013))

Stoesser (2010) extended Scottis method from technical roughness to natural roughness by generating a realistic, natural-channel bed topology from measurable physical parameters. Stoessers method requires knowledge of the mean grain diameter of d_{50}, the sediment material comprising the rough bed. The material is then placed on the bed according to a roughness-geometry function. A Cartesian grid is then generated, which in part includes the rough bed (figure 2.17) and momentum forcing is applied to force the velocity to zero in the cells that contain the roughness. The advantage of both the Scotti and the Stoesser methods is that they are extremely simple to implement numerically. Also they only require physically measurable input parameters, hence they do not rely on empirical formula or subjective roughness length scales. This is especially valuable for flows of hydraulic interest in which the details of the rough bed are only known approximately or in a statistical sense.

An example of implementation of this method in OpenFOAM can be found in Margalit (2015). Another study where this method was implemented is Stoesser et al. (2015). In all of these studies Reynolds numbers lower than the ones relevant in this thesis are present. In addition, despite the fact that the grid size can be larger than the mesh size, in the framework of LES still a quite expensive refinement is needed near the bottom wall (figure 2.17).

Implementation of a porous layer

Another modelling option would be to model the granular bed as a porous media. In the work of Breugem et al. (2006), Direct numerical simulations (DNS) have been performed in turbulent flow of a plane channel with a solid top wall and a permeable bottom wall. The focus on this study is on the effect of wall permeability on turbulence. The permeable wall is realized as a packed bed, which is characterized by the mean particle diameter and the porosity. The flow inside the permeable wall is described by means of the volume-averaged NavierStokes equations. Several experiments conducted to investigate the effect of wall permeability on turbulence, indicated that the effect of wall permeability on turbulence is different from wall roughness. This implies that wall permeability alters the structure and dynamics of turbulence. In Breugem et al. (2006) this alteration was studied by means of direct numerical simulation (DNS) of turbulent flow over a permeable wall. To that end, the roughness Reynolds number was set to a small value while the permeability Reynolds number was relatively large.

In this study, the the flow geometry is represented as shown in figure .
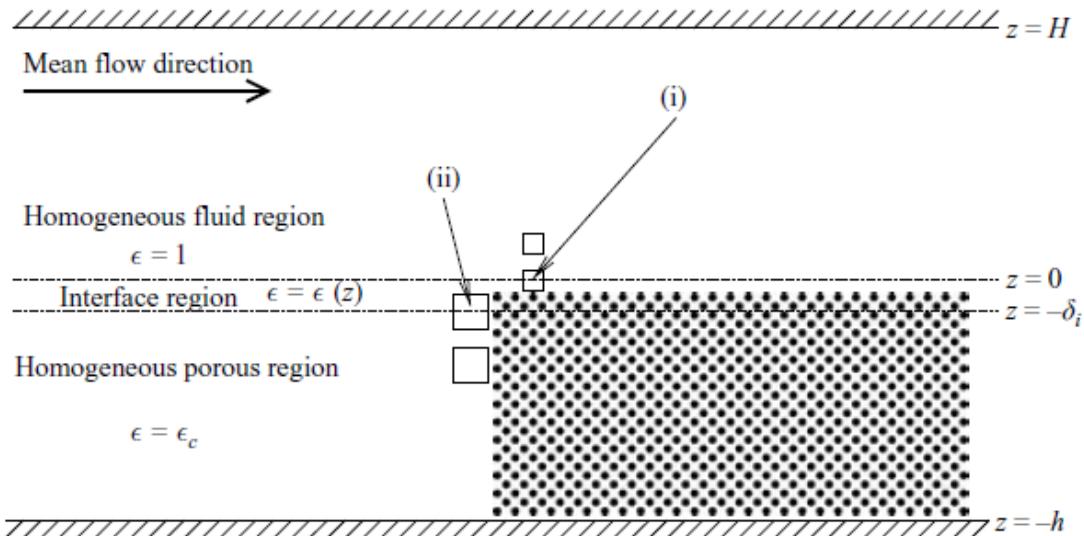
Figure 2.18: Sketch of the flow geometry. (i) Centroid averaging volume that marks the beginning of the interface region; (ii) centroid averaging volume that marks the end of the interface region. (adjusted from Breugem et al. (2006))

In this representation, three regions are distinguished:

1) The homogeneous fluid region or channel region between $z = 0$ and $z = H$ in which the porosity is equal to unity.

2) A small interface region between $z = -\delta_i$ and $z = 0$, characterized by a spatially varying porosity.

3) The homogeneous porous region between $z = h$ and $z = \delta_i$, with a constant porosity ($\epsilon = \epsilon_c$).

The implementation of DNS, as suggested before, is not possible for this study. LES could be a possible method. Still, the resolution of the grid above the porous media could prove very expensive when considering the high Reynolds numbers of this study.

Wall Functions

To date most numerical simulations of flow over rough walls have been based on the Reynolds-Averaged Navier Stokes (RANS) equations, where the effect of roughness has been accounted for by wall functions involving roughness functions determined empirically from experiments. This RANS-type treatment is, in theory, applicable in LES too. In that methods, the first grid point is placed outside the roughness layer (figure 2.19), which is the (rough) equivalent of the buffer layer in smooth walls, and an instantaneous shear stress is imposed at the boundary, in effect at the lower boundary of the first grid cell.
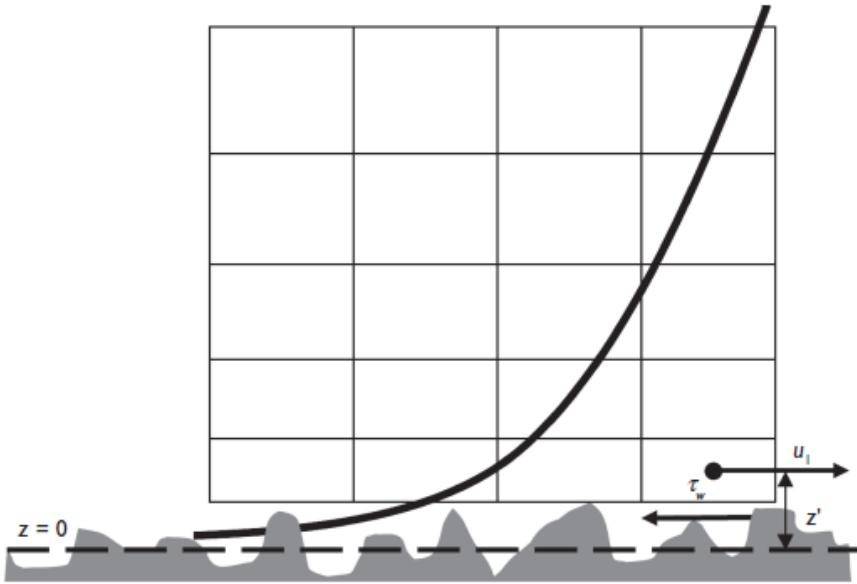
Figure 2.19: Near-wall numerical mesh cells for finite-volume LES over a rough boundary. (from Rodi et al. (2013))

The most basic and popular wall-function model is proposed by Schumann (1975):

$$\overline{\tau}_w = \frac{< \overline{\tau}_w >}{< \overline{u}_1 >}\overline{u}_1 \tag{2.28}$$

assuming a liner relation between velocity and wall shear stress ($\tau \sim u$). In equation 2.28, <> denotes time-averaging and $\overline{\tau}_w$ and $\overline{u}_1$ are the instantaneous shear stress and velocity in the first grid point (see also figure 2.19)

Next, the ratio of time-averaged shear stress and velocity at the first grid point, are obtained from a logarithmic law of the wall for rough walls of the form:

$$\frac{< u >}{u_*} = \frac{1}{\kappa}ln(z^+) + 5.5 - \Delta B \tag{2.29}$$

where ΔB in equation 2.29, expresses the downshift of the velocity profile (from the one over a smooth wall) when plotted on a semi-logarithmic Clauser plot. The friction velocity is linked to the time-averaged shear stress as:

$$u_* = \sqrt{\frac{<\overline{\tau}_w>}{\rho}} \tag{2.30}$$

In addition, the z^+ is calculated as:

$$z^+ = \frac{z u_*}{\nu} \tag{2.31}$$

The validity and accuracy of a log-law based boundary condition in LES of channel flow over rough beds is currently a topic of ongoing research. There are several uncertainties and assumptions involved in this treatment. A relatively coarse grid near the roughness may lead to inaccuracies of the velocity gradient or for flows with low water-depth-to-roughness-height the grid is too coarse over the entire water depth to resolve the dominating turbulent structures. In addition, due to the absence of local variations in bathymetry, the effects of local pressure gradients and streamline curvature on the flow are neglected. In particular if the bed is comprised of exposed roughness elements, local flow separation and recirculation can be substantial contributors to turbulence production and are likely to affect the flow over a substantial portion of the water depth. However, in Rodi et al. (2013) it is stated that for flows at high relative submergence the log law based semi-slip condition can provide reasonable results if (1) the effect of the roughness on the velocity profile can be estimated a-priori (e.g. by knowledge of the equivalent sand-grain roughness and zero-plane displacement) (2) the interaction of the flow in the roughness layer with the outer layer is very weak or absent, which is true if the roughness height is small.

Wall functions implementation in OpenFOAM

In this section, the wall functions used in the LES framework are presented. Understanding of how wall functions work in OpenFOAM is necessary in order to realize the limitations imposed when these are used in the LES framework, since they are originally derived to be used in the RANS modelling technique.

In the current thesis use is made in wall functions of the family `nutWallFunction`. More specifically, use is made of the `nutURoughWallFunction` and of `nutkRoughWallFunction` (see also figure C.2.2). They will be both discussed below.

For this section the main source of information is the source code of OpenFOAM, the work of Liu (2017) and also https://www.fluidmechanics101.com.

Standard wall functions

The main question one has to answer in case the wall modelling technique is employed is how to arrive to the correct shear stress at the wall.

The wall shear stress is defined as:

$$\frac{\tau_w}{\rho} = \nu \frac{\partial U}{\partial y} \tag{2.32}$$

As already discussed, depending on the y^+ value of the first cell-centroid near the wall, this can lie in following areas:

viscous sub-layer: $U^+ = y^+, y^+ < 11.25$
log-law area: $U^+ = \frac{1}{\kappa} log E y^+, 11.25 < y^+ < 200$

where

$\kappa = 0.4187$ and $E = 9.793$ are empirical coefficients.

The value of 11.25 defines the limit in the buffer region where the transition of the inner to the outter region is introduced. This value is refereed to as yPlusLam in OpenFOAM.

At the wall, velocity goes to zero (no-slip condition). The velocity of the first cell-centroid (U_p) is calculated from momentum equations.

In case the first cell is located in the viscous sublayer:

$$\tau_w = \nu \frac{\partial U}{\partial y}\bigg|_{y=0} = \nu \frac{U_p - 0}{y_p} = \nu \frac{U_p}{y_p} \tag{2.33}$$

In case the first cell is located in the log-law layer, the variation of the velocity gradient is no longer linear. We just simply need to impose the correct value of the velocity according to the log-law. However the shear stress has to still be computed in the same way in all cases (through equation 2.32):

$$\tau_w = \nu \frac{\partial U}{\partial y}\bigg|_{y=0} = \frac{u_* U_p}{\frac{1}{\kappa} log E y^+} \tag{2.34}$$

Equating equations 2.33 and 2.39, we get:

$$\nu_w \frac{U_p}{y_p} = \frac{u_* U_p}{\frac{1}{\kappa} log E y^+} \Rightarrow \nu_w = \frac{u_* y_p}{\frac{1}{\kappa} log E y^+} \tag{2.35}$$

and therefore:

$$\tau_w = \nu_w \frac{U_p}{y_p} \tag{2.36}$$

This means that the CFD code actually modifies the near wall viscosity when the log-law wall function is used.

The turbulence viscosity is when calculated as:

$$\nu_t = \nu_w - \nu = \nu \left(\frac{\kappa y^+}{ln(E y^+)} - 1 \right) \tag{2.37}$$

Wall functions modification for roughness

In case of roughness, τ_w is expected to increase. In this taken into account in with the following modification in the log-law:

$$U^+ = \frac{1}{\kappa} log E y^+ - \Delta B \tag{2.38}$$

where ΔB is a function of size and shape of roughness elements.

To assign the value of ΔB, the code uses the input value ks to calculate ks^+ and then:

If $ks^+ < 2.25$, $\Delta B = 0$ [hydrodynamically smooth flow]

If $2.25 < ks^+ < 90$, $\Delta B = \frac{1}{\kappa} log \left(\frac{ks^+ - 2.25}{87.75} + Csks^+ \right)$

If $ks^+ > 90$, $\Delta B = \frac{1}{\kappa} log(1 + Csks^+)$ [hydrodynamically rough flow]

It is then understood that increasing ks^+ slightly, change the value of ΔB very little because the variation is logarithmic.

Finally, in OpenFOAM, ΔB is embedded to E as:

$$U^+ = \frac{1}{\kappa} log E y^+ - \Delta B = \frac{1}{\kappa} log E y^+ - log e^{\Delta B} = \frac{1}{\kappa} log \frac{E y^+}{exp \Delta B} = \frac{1}{\kappa} log E' y^+ \tag{2.39}$$

with

$$E' = \frac{E}{exp\Delta B} \tag{2.40}$$

As in case of smooth wall function in 2.40, the wall turbulent viscosity is calculated as:

$$\nu_w = \frac{u_* y_p}{\frac{1}{\kappa} log E' y^+} \tag{2.41}$$

`nutURoughWallFunction` vs `nutkRoughWallFunction`

Finally, some attention is paid to the `nutkRoughWallFunction`, which is defined as a boundary condition that provides a turbulent kinematic viscosity condition, based on turbulence kinetic energy. In contrary, `nutURoughWallFunction` is stated that provides a turbulent kinematic viscosity condition, based on velocity.

Their difference ins traced to the definition of y^+ and friction velocity. In case of `nutURoughWallFunction`, the friction velocity and y^+ are calculated as:

$$u_* = \sqrt{\frac{\tau_w}{\rho}} \tag{2.42}$$

and

$$y^+ = \frac{\sqrt{\frac{\tau_w}{\rho}} y}{\nu} \tag{2.43}$$

Equation 2.43 along with equation 2.39, form a 2 equations with 2 unknowns (U^+ and y^+) system to be solved with iterations.

In the case of `nutkRoughWallFunction`, the friction velocity and y^+ are calculated as:

$$u_* = \sqrt{C_\mu k_p} \tag{2.44}$$

and

$$y^* = \frac{\sqrt{C_\mu k_p} \rho y}{\nu} \tag{2.45}$$

In this case, the value of k_p is already known, so no iterations are needed. Hence this method is computationally less expensive than using the `nutkRoughWallFunction`.

2.2.4. Conclusion

Based on the analysis done in section 2.2.1 and especially the numerical output of the IDDES model presented in Stevens (2018), it is concluded that there is room for improvement in the numerical modelling especially in predicting free turbulence, the initiation of mixing layer and also in resolving high frequencies up to the ones that correspond to the stone size (2.1.1). In addition, the investigation of ways to represent a rough boundary is presented in section 2.2.3. Based on this, wall functions in the LES environment are suggested as a next step mainly because of the numerical demands that the other methods would impose, which are far too large when considering the high Reynolds number engineering flows that the present study is dealing with. That being said, the Wall-Modelled LES (WMLES) method is the one that the present study will implement.

2.3. The long sill experiment

In this section, first the motivation is given for the choice of the experiment to be simulated. After that, the selected experiment is described.

2.3.1. Motivation for choosing an experiment

In this section, an overview is given of the experiments that where considered for modelling purposes. The author tried to find experiments that included measurements of both hydrodynamics of non-uniform rough flow and stone displacement counting. Many experiments are available in literature that measure pressure fluctuations and the development of turbulent boundary layer above rough surfaces, but usually these are more fundamental studies, with small roughness elements, or just different than the ones representing a natural gravel bed (for example Amir et al. (2014)). These were not considered as suitable for the purposes of this thesis.

Overview of relevant experiments

Experiment	Set-up	Measuring equipment/methods	Additioinal info
Hofland (2005)	1.uniform open channel flow 2.smooth to rough bed transition 3.BFS	pressure sensors LDV	pressures measured around target stone goal of measurements to distinguish force gnerating mechanisms
DeRuijter (2004)	1.uniform open channel flow 2.BFS	PIV pressure sensors motion sensors	pressures and motion sensors around target stone goal of measurements to get insight on coherent structures
Dessens (2004)	local contraction	EMS	lower measurement at 4 cm above bed measured displaced stones out of colored strips 7 measurements over the depth large stones with Dn50=2 cm small stones with Dn50=8.2 mm
Jongeling et al. (2003)	1. uniform flow over flat bed 2. roughness transition 3. flow under a gate 4. long sill 5. short sill	LDV EMF	measured displaced stones out of colored strips lower measurement at 2 cm above bed
De Gunst (1999)	BFS	LDA EMS	measured displaced stones out of colored strips
Hoan (2008)	gradual expansion with 3 different expansion rates	LDV EMS	bed response and flow field both measured lower measurement at 3 mm above bed

Table 2.1: Overview of experiments considered

Conclusion

The long sill case of the Jongeling et al. (2003) experimental set is chosen for this thesis. It is a quite old experimental set with hydrodynamics data available and also stone displacement measured. The latter is not used in the current thesis, but when choosing this case, the possibility will be for a successor to continue on this study with stone stability. In addition, choosing this experiment will enable the author to compare different modelling techniques, since the long sill experiment was also used in the study of Stevens (2018).

To the author's knowledge there is no measurement campaign where PIV is used for the hydrodynamics and also the stone displacement to be measured.

2.3.2. Experiment Description

In this section, the experiment selected to be modelled will be discussed.Since the execution of the experiment itself was not the subject of this study, only the information needed to reproduce a "numerical twin" of the experiment are presented here. More details on the experiment can be found in Jongeling et al. (2003).

Overall set-up

The experiment was undertaken as part of a project aiming at improving methods for designing granular bed protections in Delft Hydraulics, during the years 2001-2003. The project included a set of measurements with different geometries followed by numerical simulations using ANSYS CFX software. The present thesis deals with the experiment made with a long sill with 1:8 upstream slope and 1:3 downstream slope. The experiments also included the measurement of stones displayed from the granular bed protection under the effect of the flow loads. That being said, the project aimed at deriving a design methodology for the bed protection, based on a representative flow load and a stone transport concept. Many geometries were used in order to generalize the methodology. An overview of the experimental facility can the realized in figure 2.20.
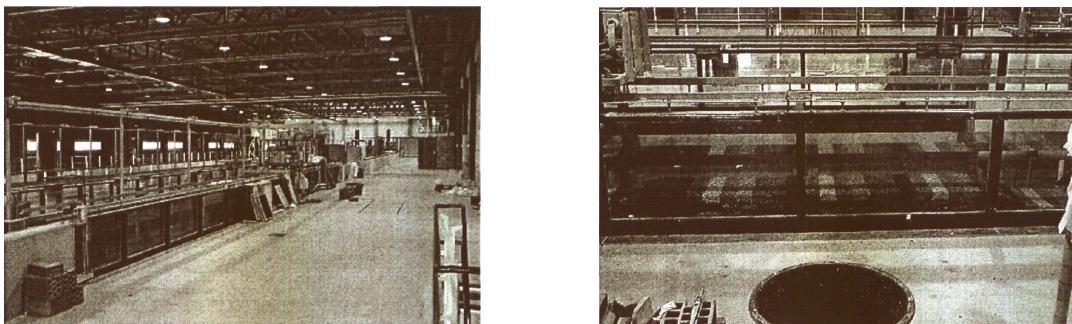
Figure 2.20: Experimental facility. Left:flume used. Right: the long sill set-up (from Jongeling et al. (2003))
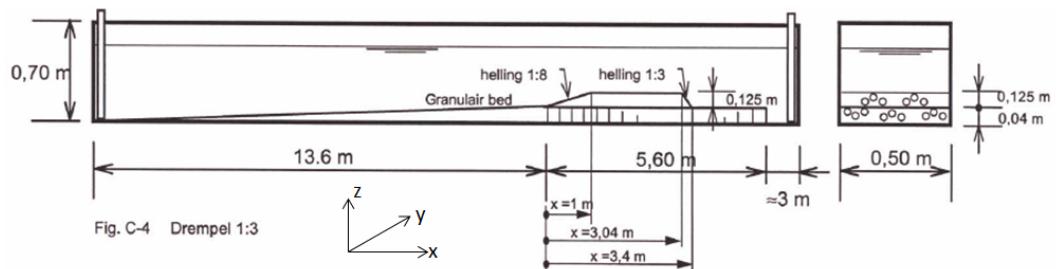
Figure 2.21: Experimental set-up of the "long sill" experiment(from Jongeling et al. (2003))

The flume used for the long sill experiment had a with of 0.50m, height 0.70m and was approximately 23m long (figure 2.21). It was provided with a pump system and water was recirculating. At the downstream side of the flume, an adjustable weir was installed, to control the water level. The first 19.2 m of the flume were covered with stones of nominal diameter d_{n50} of 6.2 mm. In addition the first 13.6 m of the flume had a gradual slope with maximum thickness 40 mm at the start of the measuring area. This approach length was considered large enough for the initial disturbances caused by the inflow to die out and the flow to be adapted to the rough bottom. After this approach length section, a flume section of 5.6 m was covered with a 40 mm thick layer, painted stones in strips of 10 cm wide (see figure 2.22). Seven colors of strips have been repeated eight times. The purpose of the colored strips was to be able to find out also where the stones to be moved under a flow condition, originate from in the flume.
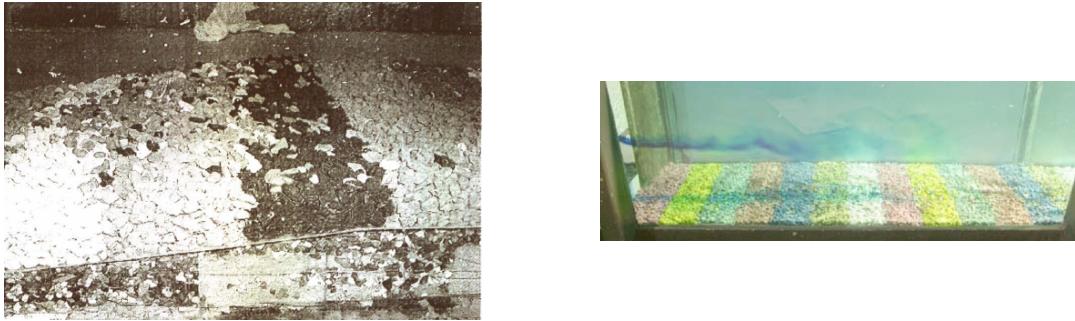
Figure 2.22: Implession of the color strips of granular bed protection (from Jongeling et al. (2003))

Experimental procedure

During the experiment, measurements were performed of velocity, turbulence, water levels and flow rates. An overview of the instruments used is presented in table 2.2. The definition of coordinate system used can be seen in 2.21.

Instrument	Parameter measured	Measuring direction	Location in the flume
LDV	velocity	x,z	center of the flume
EMS	velocity	x,y	center of the flume, 6cm downstream of the LDV
Wave gauge	water level	z	1. close to the right wall, not to interfere with EMS 2.upstream of colored strips, x=-1 (fixed position)
Dischargemeter	discharge	x	in the return circuit
Peilnaalden	water level of still water (only at the beginning of the test)	z	x=-13.6 m and x=6 m

Table 2.2: Measuring instruments

The measurement signals from the LDV and EMS were sampled at a frequency of 100 Hz and filtered off above 50 Hz. The frequency range up to 50 Hz was considered enough to measure turbulence in the flow. The duration of each measurement (one point in the vertical) was always 180s. In each experiment, time series where extracted in various cross sections and various positions in the vertical.The mean velocity $\overline{u}$ in each point measurement was defined as:

$$\overline{u} = \frac{1}{n} \sum_{n=1}^{n} u_i \tag{2.46}$$

with n being the number of samples. The mean velocity components $\overline{v}$ and $\overline{w}$ were defined accordingly. The standard deviation σ_u was defined as:

$$\sigma_u = \sqrt{\frac{1}{n} \sum_{n=1}^{n} (u_i - \overline{u})^2} \tag{2.47}$$

The mean turbulent kinetic energy in each point was defined as:

$$k = 0.5(\sigma_u^2 + \sigma_v^2 + \sigma_w^2) \tag{2.48}$$

The measuring accuracy of the LDV is estimated to be about 0.01 m/s. The results of the EMF are considered to include a slightly larger measuring error. The measurements near the bed are expected to contain are larger measuring error, as near the bed the velocity gradients are larger.

The measurement closer to the bed was 2 cm above the bed and the measure closer to the free surface was 7 cm away from the free surface. As can be seen from figure 2.23, out of 10 measuring cross sections, two were on top of the sill with 8 points in the vertical, while the rest had 11 points in the vertical measured. Each time series spanned 3 minutes. At the end of each test the number of stones moved from a strip or entered one were noted.
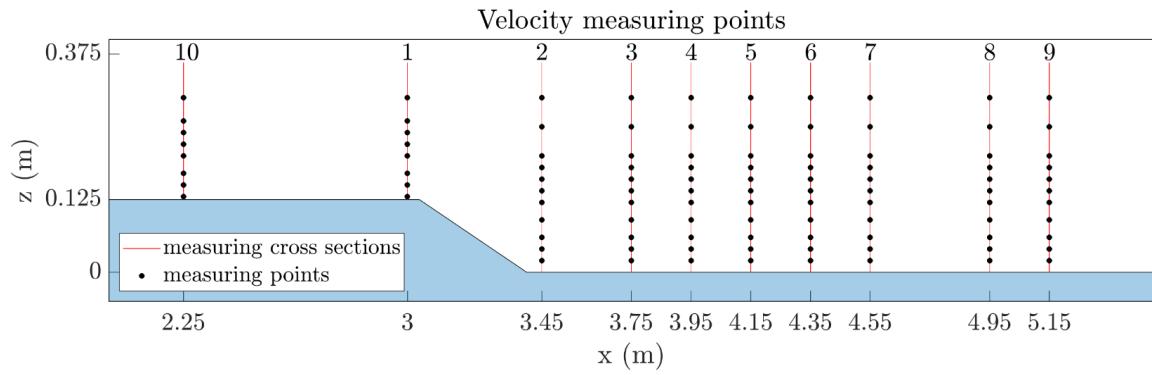
Figure 2.23: Measuring velocity points in Jongeling et al. (2003)

Finally, in table 2.3, some characteristic dimensionless numbers of the flow state are presented for the small depth case.

Geometry	Mean discharge (l/s)	Mean velocity $\overline{U}$ (m/s)	characteristic length (cm)	Reynolds number (-)	Froude number (-)
Long sill small depth	99.58	0.5311	37.5	198750	0.27

Table 2.3: Flow state characteristics

3

Model setup

In this section, all the important choices for the models setup are reviewed and discussed. The motivation for these choices comes from the literature review of the numerical modelling aspects from the previous section and also from some information coming from the appendix

Based on the previous works done in this research area and described in section 2, it is concluded that the possibility of LES with a rough wall function simulation is the next next to be investigated in this research area.

However, WMLES and especially with rough elements as our case, is a set-up that to the authors notice is not well investigation within the capabilities of OpeFOAM. To that end, first, the setup in given for the more fundamental case of an open channel flow case. Wall functions performance in combination with SGS models is tested. Secondly, the set-up of the RANS simulation of the long sill case is presented. This serves as a precursor simulation before the LES simulation. Finally the long sill domain setup is presented and elaborated in more detail. Most results and analysis of this thesis works is based on this set-up. The long sill experiment is already described in section 2.3.

3.1. WMLES of an Open Channel

In this section, all important choices for the model set-up of a simple open channel flow case are given in detail. Since this is a fundamental test case, many of the modelling choices are based on literature of similar studies and they are indicated below.

3.1.1. Flow conditions

A summary of the hydraulic parameters is presented in table 3.1. The height h of the domain, the mean bulk velocity U_b and the equivalent sand grain diameter k_s, are selected to be the same with the experiment of Jongeling et al. (2003), later to be modelled.

Geometry	h (m)	U_b (m/s)	Re (-)	Fr (-)	u_* (m/s)	k_s (mm)
flat bed	0.375	0.5311	$2 \cdot 10^5$	0.2	0.0362	12.4

Table 3.1: Hydraulic conditions for the cyclic case

3.1.2. Grid and boundary conditions

A simple 3D flat plate domain is built. The model consists of a rectangular box with length of 9δ in the streamwise direction, 4δ in the spanwise and 2δ in the wall-normal direction, with $\delta = 1$ denoting the channel half-height. These dimensions are considered sufficient to accommodate the turbulence structures and are suggested by literature (Mukha et al. (2018), Moin and Kim (1982)). Other configurations were tested with no significant difference in the results. In all cases, the domain mesh is represented by equidistant cubic cells. More details of the mesh generation for this case can be found in appendix D.

Cyclic boundary conditions are applied in the inlet,outlet and sides of the domain for the velocity and pressure fields. The slip boundary condition is applied to the top boundary, while the no-slip condition is applied to the bottom (see figure 3.1). In the bottom, the wall functions are tested. Since more than one wall functions with roughness are available in OpenFOAM, and no systematic reporting of their performance in the LES environment is found in literature, the choice is made to test all of them. More specifically, the `nutURoughWallFunction`,`nutkRoughWallFunction` and the `nutkAtmRoughWallFunction` wall functions are used.
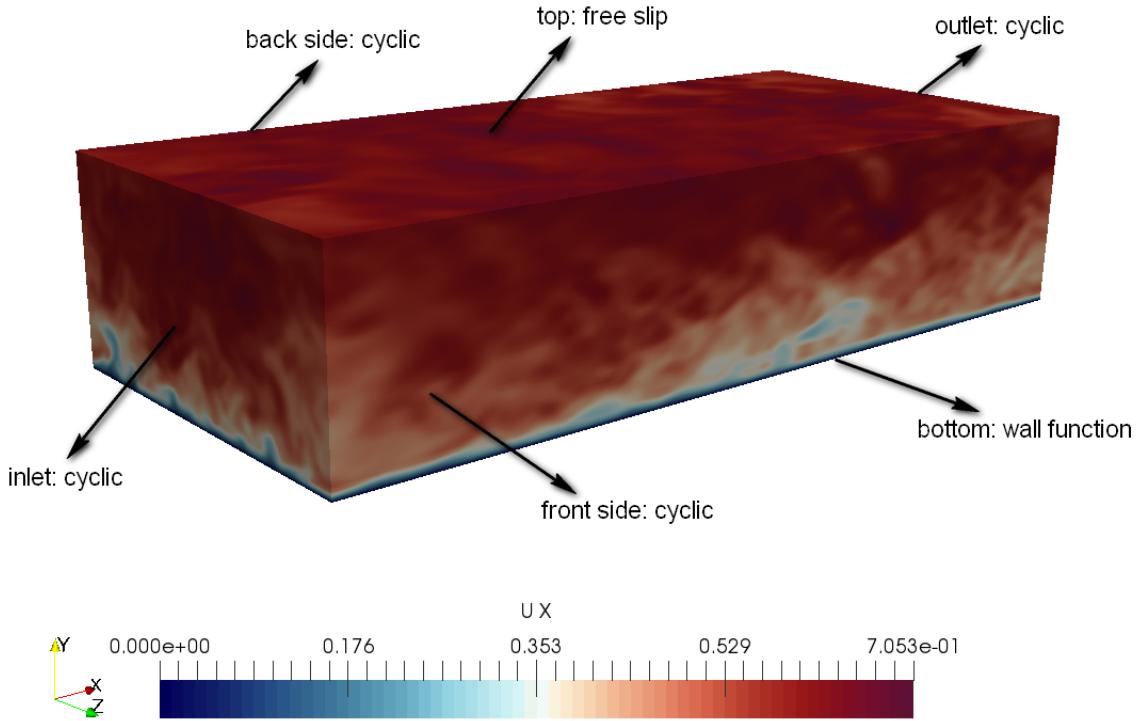
Figure 3.1: Geometry model of the cycli LES simulation

To drive the flow in the domain, there is the choice to define the pressure gradient or the bulk mean velocity U_b:

$$U_b = \frac{1}{h} \int_0^h <u> dy \qquad (3.1)$$

This is done with the following lines in the `fvOptions` file in the `system` directory:

```
  momentumSource
{
    type        meanVelocityForce;
    active      on;
    selectionMode  all;
```

```
    meanVelocityForceCoeffs
    {
        fields (U);
        Ubar        (0.5311 0 0 );
        selectionMode all;
    }
}
```

The computational procedures of fixing U_b, were already implemented in OpenFoam and known from past studies (eg. Mukha and Liefvendahl (2015)). It is also considered more practical to prescribe a mean velocity or discharge rather than a pressure gradient to drive the flow, since in many applications the discharge is usually the known flow parameter. For these reasons the bulk mean velocity U_b is specified as input parameter in this study. However, the pressure gradient has to somehow be computed. This is done by introducing an additional external force term into the momentum equation. This artificial force drives the flow, and the magnitude of the force is determined by the prescribed bulk velocity. At each time step, the actual U_b is re-calculated, and an adjustment to the magnitude of the external force is made, to correct the value. With this set-up the main objective is then the correct prediction of the friction velocity or the bed shear stress.

In case of WMLES, the effort is to accurately resolve the outer layer. That being said, the number of cells n_0 per δ^3-cube is the relevant number. In Mukha et al. (2018) and Spalart (1997), numbers in the range from 8000 to 27000 are considered sufficient. This corresponds to 20 to 30 cells used to discretize the channel-half height, $\frac{n}{\delta}$. Both limits are applied in this test case.

In addition, the choice of the sub-grid model is expected to play an important role. Due to computational limitations, the choice is made to test the standard Smagorinsky model and the WALE model, which is also used and suggested by Mukha et al. (2018) and other researchers to perform good with relatively coarse grids.

3.1.3. Numerical process

The PISO algorithm is employed. At all cases, the CFL is kept under 0.5. Second order schemes are used for the time and space discretization, according to suggestions by Mukha (2018). The numerical choices are similar to the ones described in more detail in section 3.3.5.

3.2. RANS long sill

Before proceeding to the more demanding LES simulation of the long sill case, it was considered important to run precurson RANS simulations. The main reasons for that, was firstly to acquire an initial RANS solution for the LES simulation, get a first impression of the flow features in a relatively cheap simulation and secondly to test the inlet discharge value and rigid-lid assumption in a simpler set-up. Concerning the inlet boundary condition, in both Jongeling et al. (2003) and Stevens (2018), some adjustment was needed to the measured discharge, namely an up to 5% increase, to arrive to a good validation.

The set-up of the RANS long sill case simulation is described in short. Similarities with the WMLES long sill case set-up are highlighted.

3.2.1. Geometry and Mesh

The geometry of the model exactly reproduces the experiment flume. The coordinate system can be seen in figure 3.2. The total length of the domain is 19.2. The first 13.6 m, approximately equal to 100 step heights, have a mildly sloping bed, while the rest 5.6 m contain the slopping BFS. The top of the flume has the shape of the measured free surface (see also section 3.3.4). Side walls are present. The width is then 0.5 m.

inlet   outlet
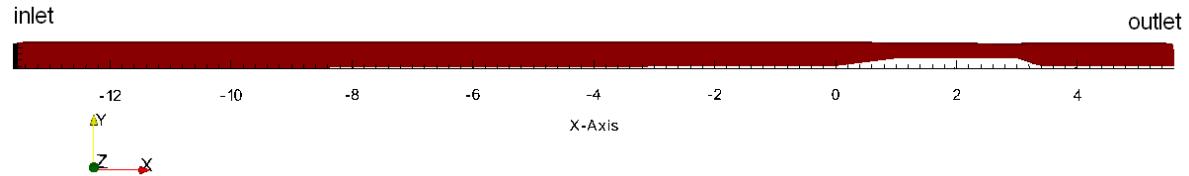
Figure 3.2: Geometry model of the RANS simulation

Concerning the mesh, the choice was made to use the same mesh in RANS and WMLES simulations. For reasons that will be made clearer in the next section, a homogeneous mesh of 8 mm was used for the first 20 cm of the domain (figure 3.3). For the upper part of the domain, Δx and Δz, remain 8 mm, while in the vertical a cell to cell expansion ratio is set. The mesh consists of 5205830 hexahedra.

homogeneous mesh region
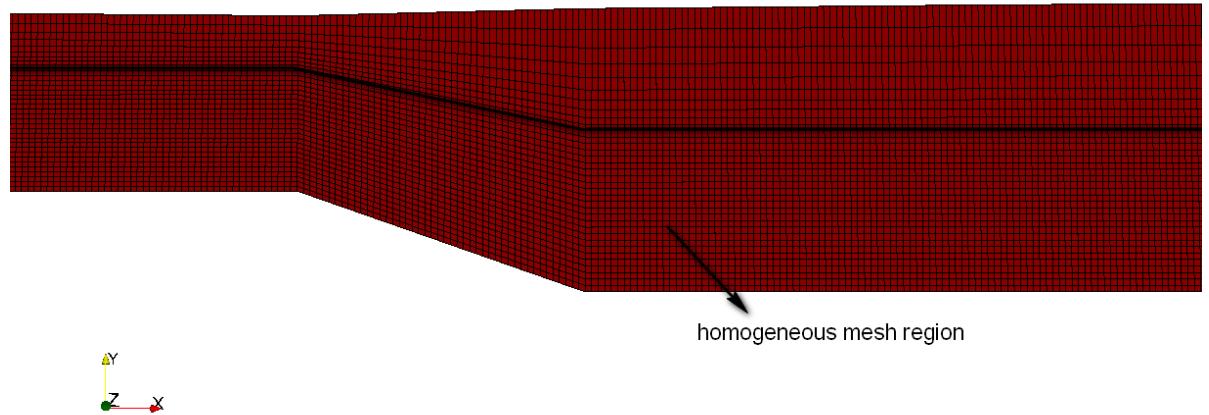
Figure 3.3: Mesh in the downstream region with indication of the homogeneous mesh region

3.2.2. Initial and boundary conditions

Uniform initial condition values were used in the required fields. These are summarized in table 3.2.

Field:	U (m/s)	p (m^2/s^2)	ν_t (m^2/s)	k (m^2/s^2)	ϵ (m^2/s^3)
Value:	0.5311	0	0	0.0042135	0.001712052

Table 3.2: Initial conditions for the RANS simulation

It must be noted that the initial conditions for the turbulence properties are set according to the following equations suggested for OpenFOAM:

Reference velocity:
$$U = 0.53 \text{m/s} \tag{3.2}$$

Turbulent length scale:
$$L = 0.07 x h = 0.02625 \text{m} \tag{3.3}$$

Turbulent intensity:
$$I = 10\% \tag{3.4}$$

Turbulent kinetic energy:

$$k = \frac{3}{2}(UI)^2 \tag{3.5}$$

Dissipation rate:

$$\epsilon = 0.09^{3/4} \frac{k^{3/2}}{L} \tag{3.6}$$

In OpenFOAM, all flow parameters need to be assigned to all boundaries surrounding the domain. An overview is given in table 3.3.

Boundary	U (m/s)	p (m^2/s^2)	ν_t (m^2/s)	k (m^2/s^2)	ϵ (m^2/s^3)
inlet	cyclic profile	zeroGradient	calculated	0.0042135	0.001712052
outlet	inletOutlet	0	calculated	inletOutlet	inletOutlet
top	slip	zeroGradient	zeroGradient	zeroGradient	zeroGradient
bottom	noSlip	zeroGradient	*nutkRoughWallFunction*	*kqRWallFunction*	*epsilonWallFunction*
side walls	noSlip	zeroGradient	*nutkWallFunction*	*kqRWallFunction*	*epsilonWallFunction*

Table 3.3: Boundary conditions for the RANS simulation

The roughness at the bottom is defined as:

```
lowerWall
  {
      type            nutkRoughWallFunction;
      Ks              uniform 0.0124;
      Cs              uniform 0.5;
      value           uniform 0;
  }
```

where k_s is the sand-grain roughness height and Cs is a roughness constant, with Cs=0.5 for uniformly distributed and closely packed sand. The side wall are modelled as smooth.

It must be noted that a logarithmic velocity profile is set at the inlet, to set the mass flux. To that end, a simple periodic simulation is build, same with the one described in appendix C, but with the side walls defined as walls with the no-slip condition (figure 3.4). With this boundary conditions it takes approximately 40 s for the water to flow through the domain.
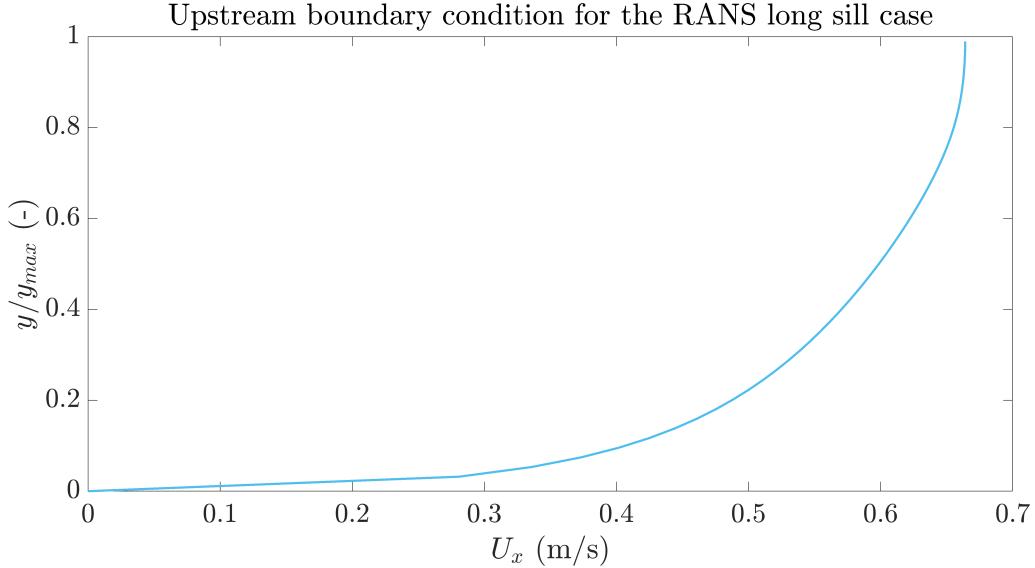
Figure 3.4: Inlet velocity profile extracted in the middle of the domain doe the RANS long sill case

3.2.3. Turbulence model and wall function

Concerning the turbulence model and wall function choice, these are selected based on the cyclic RANS case presented in appendix C. That being said, the realizable $k - \epsilon$ turbulence model is the first choice. However, the k-ω SST model is also used here for comparison. In appendix C, it was concluded that the choice of `nutURoughWallFunction` against `nutKRoughWallFunction`, resulted in little difference. Therefore, the argument provided in section 2.2.3, namely that the `nutKRoughWallFunction` is less intensive for the solver, makes it the more attractive than `nutURoughWallFunction` and it is indeed the one used for the RANS long sill simulation.

3.2.4. Numerical process

For the RANS simulations, the PIMPLE algorithm is used. The CFL number was kept in all cases below 1. A further lowering of the CFL number resulted in no difference.

Each term in the model equations is discretized with a specific scheme. In all cases, in beginning of the simulation, first order schemes were used, which were later switched to second order.

Concerning the solvers choice, the GAMG solver is used for the pressure equation and the PBiCGStab solver is used for the momentum and the turbulence model equations. Loose tolerance is selected for the first seconds of the simulation which is later switch to tighter values.

Convergence of the mean quantities is monitored through the residuals.

3.3. WMLES long sill

In this section the set-up of the wall-modelled LES simulation of the long sill is described in detail.

3.3.1. Geometry and Mesh

The overall geometry of the model can be seen in figure 3.5 with the corresponding coordinate system. Comparing this domain with the one used for the RANS simulation (see figure 3.2), the first 13.1 m are missing. This is done due to computational limitations.
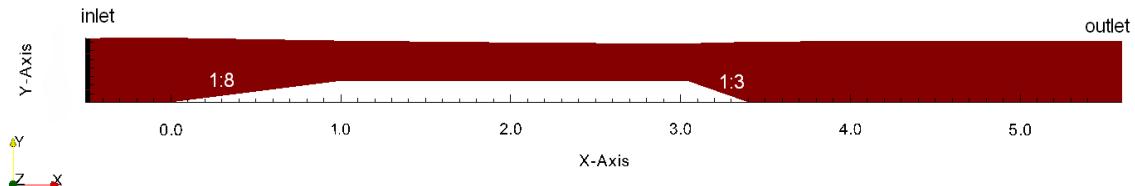
Figure 3.5: Geometry model of the WMLES simulation

As described in section 2, in work of Stevens (2018), it was concluded that a finer mesh is needed for important flow scales to be resolved. In this thesis, the mesh is furthered refined to 4mm. In figure 3.6, two regions are discerned. In the region of interest, region 1, the mesh is homogeneous, namely $\Delta x = \Delta y = \Delta z$. In region 2, a cell to cell expansion ratio is adopted which is lower than the suggested limit of 1.2. It must be noted that in case of LES simulations, a homogeneous grid is suggested to be used. However due to computational restrictions this is done only in region 1, 20 cm above the bed, where the most interesting flow features are expected to appear.

An overview of the mesh properties is given in table 3.4.
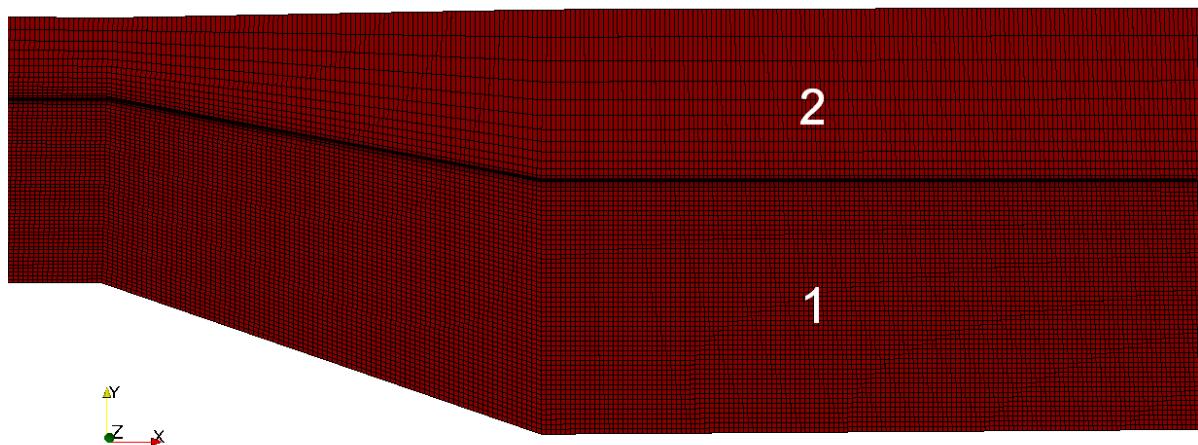
Figure 3.6: Impression of the homogeneous mesh region (1) and the mesh region with cell to cell expansion ration (2)

Mesh	Δ x (m)	Δ y (m)	Δ z (m)	Cell to cell expansion ratio	No. Cells
Coarse	min: 8mm max: 3cm	8mm	8mm	region 1: 1 region 2: 1.15	1682415
Fine	min: 4mm max: 2.8cm	4mm	4mm	region 1: 1 region 2: 1.15	12200000

Table 3.4: Mesh Properties for LES simulations

3.3.2. Subgrid model and wall treatment

The wall shear stress in the domain, depends on the wall-function. In addition, the subgrid model determines the sub-grid scale viscosity in the near wall region. Combining the two, one should arrive to the correct value of the shear stress. Since there is no clear consensus is literature about this, wall function sensitivity tests were performed that revealed that only the wall function based on velocity `nutURoughWallFunction` performed best in the LES environment in OpenFOAM (see section 4.1).

The following sub-grid models are tested:

1) WALE
2) Dynamic Smagorinsky
3) Smagorinsky
4) k-equation model

An overview of these models can be find is section 2.2.2. All of the above models were already implemented in OpenFOAM, except for the dynamic Smagorinsky model which was compiled in the OpenFOAM code. This was freely available from Passalacqua (2010). The subgrid-models are defined inside the turbulenceProperies file of the `constant` directory, while the wall functions are defined in the `nut` file of the `0` directory. An example of defining the the sub-grid model can be seen in the following:

```
simulationType LES;

LES
{
    LESModel        WALE;
```

```
    turbulence     on;

    printCoeffs    on;

    delta          cubeRootVol;
}
```

Regarding the delta (Δ) values used for the various sub-grid models, in all cases this is set to vanDriest. An exception is the WALE model where the cubeRootVol setting was chosen, since the WALE model does not require damping close to the wall (see also section 2.2.2).

The roughness of wall bottom is introduced by the equivalent sand roughness diameter ks. According to Jongeling et al. (2003), this is set as:

$$k_s = 2D_n^{50} = 1.24cm \tag{3.7}$$

The side walls are modelled as smooth, using the `nutUWallFunction`.

```
lowerWall
    {
        type           nutURoughWallFunction;
        roughnessHeight 0.0124;
        roughnessConstant 0.5;
        roughnessFactor 1;
        value          uniform 0;
    }
    frontAndBack
    {
        type           nutUWallFunction;
        value          uniform 0;
    }
```

In roughness constant C_s in the`nutURoughWallFunction` function is set to 0.5, which is the default value in OpenFOAM and it represents uniformly distributed and closely packed sand. Sensitivity tests for this parameter were done in the Open Channel flow case and showed only minor change of the results with varying C_s factor, for a value of $k_s of 0.0124m$.

3.3.3. Initial and Boundary conditions

The output of the RANS simulation served as the initial condition for the coarse LES simulation. More specifically, the velocity U and pressure p are used. Since the same mesh was used in both simulation no interpolation was needed. The part of the RANS model mapped to the LES simulation can be seen in figure 3.7.
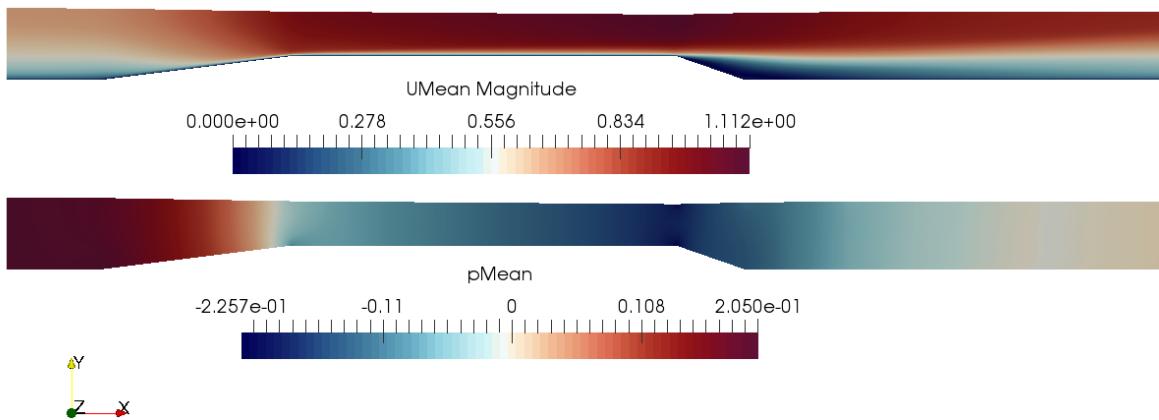
Figure 3.7: Initial condition for velocity and pressure fields for the LES simulation

It must be noted that using the turbulent viscosity ν_t field of the RANS simulation as initial condition for the ν_{SGS} field of the LES simulation is inconsistent.

Special attention is also paid to the boundary conditions. An overview is given at table 3.5.

Boundary	U (m/s)	p (m^2/s^2)	ν_{SGS} (m^2/s)
inlet	turbulentDFSEMInlet	zeroGradient	calculated
outlet	inletOutlet	0	calculated
top	slip	zeroGradient	zeroGradient
bottom	noSlip	zeroGradient	*nutURoughWallFunction*
side walls	noSlip	zeroGradient	*nutUWallFunction*

Table 3.5: Boundary conditions for the LES simulation

Regarding the inflow turbulence generator needed for the LES simulation, the Divergence Free Synthetic Eddy Method (DFSEM)method as suggested by Poletto et al. (2013) is used. This method is already implemented in OpenFOAM. More information on this method and also other methods considered for inlet turbulence generation as described in section 2.2.2.

To make use of this method, velocity, Reynolds stresses and turbulence length scales are needed. These are extracted from a RANS simulation of the first 13.6 meters of the domain. An overview of the approach is visible in figure 3.8.
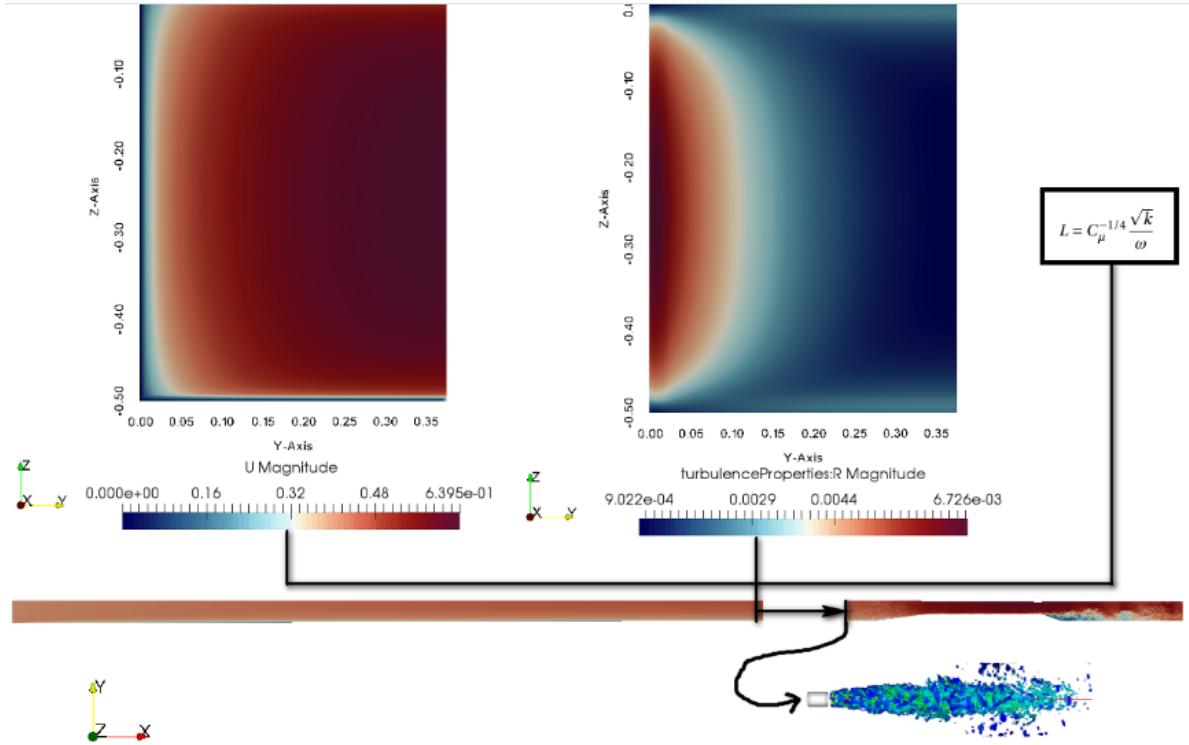
Figure 3.8: Overview of the RANS and LES domain. Output of the RANS domain gets processed and becomes input in the LES with the *turbulentDFSEMInlet* boundary condition.

The velocity U and Reynolds stress tensor are extracted directly from the RANS simulation. The L file is generated from the turbulence parameters k and omega in a Matlab script, according to the definition of the turbulent length scale in the $k - \omega$ turbulence model:

$$L = C_\mu^{-1/4} \frac{\sqrt{k}}{\omega} \tag{3.8}$$

3.3.4. Free surface treatment

The rigid lid approximation is used in the present study for all simulations. In this way one avoids the challenges imposed by the volume of fluid solvers, while saving computational time. In the case that a horizontal top surface is implemented in the domain, any surface variations present in the experiment are accounted for in the pressure variation term. However, it is possible to approximate the shape of the free surface using the measured water levels from the experiment.

To understand if the latter treatment is needed, we can compare the measured magnitude of the surface deviation h, with respect to local water depth d. As suggested by Rodi et al. (2013), if ratio of the two is small, say below 10%, the error introduced in the continuity equation is small. According to figure 3.9, this ratio is well above 10%, in the region above the step. It must be noted, that during the experiment the free surface displacement in the measuring locations was remarkably stable and steady in time. In addition, in Fan et al. (2017) a Froude number of 0.3-0.4 is suggested as the limit for the validity of the rigid lid assumption. In the long sill case a Froude number of approximately 0.3 to 0.6 is expected. That being said, a simplified shape of the free surface based on the measured water displacements is introduced in the top boundary of the domain.
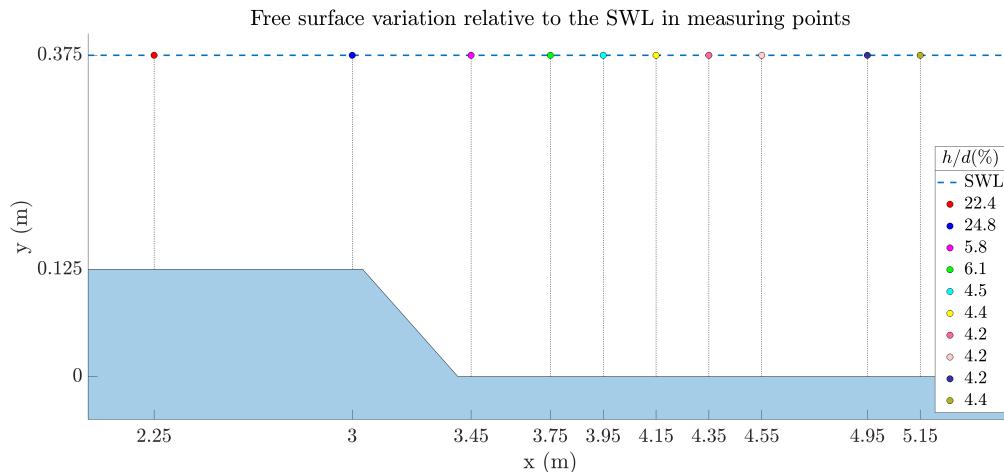
Figure 3.9: Magnitude of the surface displacement h, divided by the local water depth d in various cross sections. Data retrieved from Jongeling et al. (2003).

3.3.5. Numerical Process

Choosing spatial interpolation and time-marching schemes has to be done with care in order to have a good balance between accuracy and stability. To obtain reliable results in LES at least a second order accuracy is needed.

In the simulations presented here, a second order backward differentiating scheme was used for time marching.The time-step was chosen to be small enough to keep the Courant number below 0.5.

Concerning the spatial discretization, a common scheme used is the linear interpolation. According to Mukha (2018), this scheme (second order and unbounded), leads to the introduction of numerical oscillations. Due to the small sizes in wall-resolved LES this does not cause a problem, but in wall-modelled LES it can affect the solution substantially. Therefore the LUST scheme is selected, which uses a blending of the linear and the linearUpwind scheme. In this way, the oscillations coming from the liner interpolation, are reduced due to the numerical dissipation coming from the upwinding. Finally, the PISO algorithm is used with 3 nCorrectors and 2 nNonOrthogonalCorrectors.

$$4$$

Results

In this section the results of the simulations are presented. Their set-up is already described in the previous chapter. First, the wall functions sensitivity tests in the simple open channel flow case are presented. Next, the results of the RANS long sill simulation are presented, followed by the WMLES simulation results. Since the latter ones are the most significant in this thesis, some extra analysis is undertaken.

4.1. Open Channel Flow

The wall functions performance is evaluated in the LES environment. Test are done and results are presented for different:

- wall functions
- sub-grid models
- mesh size
- k_s to cell size ratio

A description of the sub-grid models and wall functions used, can be found in chapters 2.2.2 and 2.2.3. Concerning the validation procedure, as mentioned in chapter 3.1.2, the mean bulk velocity U_b in the numerical model is fixed. That being said, the model friction velocity u_*, is then the output parameter of interest. This is compared with the theoretical friction velocity coming from the log-law for rough surfaces. Before the main results of this case are presented, the necessary steps to arrive both to the theoretical friction velocity and the model one are described. This will help to get an idea of the uncertainty of the final calculated error.

Theoretical friction velocity

According to Jongeling et al. (2003), the equivalent sand grain diameter in the long sill experiment is defined as $k_s = 2D_n^{50} = 1.24cm$. Supposing that we are in the fully rough regime, the following equation can be used to arrive to the friction velocity (Uijttewaal (2002)):

$$\frac{\overline{u_{da}}}{u_*} = \frac{1}{\kappa} ln\left(\frac{h}{k_s} + 6.1\right) \tag{4.1}$$

where
$\overline{u_{da}}$ Depth and time-averaged velocity   (m/s)
u_* Friction velocity   (m/s)
κ von Karman constant   (-)
h Height   (m)

Equation 4.1, can be derived by integrating over the depth the log-law for rough boundaries (Southard (2006)):

$$\frac{\overline{u}}{u_*} = \frac{1}{\kappa} ln\frac{y}{k_s} + 8.5 \qquad (4.2)$$

In that way it can be seen that the constant 6.1 in equation 4.1, comes from the constant 8.5 in equation 4.2. But how certain is 8.5? In Southard (2006), it is stated that 8.5 is the value corresponding to uniform closely-packed sand grain diameters, according to the experiments of Nikuradse (1933), where the constant 8.5 was derived. It is expected that for roughness geometries of our kind, where the shape and roughness height is not uniform, the shape and the arrangement of the roughness elements will result in different turbulent structures above the wall, than the ones that the original experiment included. The velocity profile will be affected accordingly.

From equation 4.1, we can get an idea of how sensitive our theoretical prediction is to 6.1. More specifically, changing the value 6.1 by 5%, results in 2% change in the friction velocity u_*.

From the above a value of 0.0362 m/s is calculated for the theoretical friction velocity, with a standard deviation of 2%.

Model friction velocity

Next, the necessary steps taken to arrive to the model friction velocity in the open channel flow cases are presented.

First of all, the wall shear stress τ_b and y^+ values are set-up for averaging in time in the `controlDict` directory.

where $y_{plus} = \dfrac{yu_*}{v}$ $(-)$
$\tau_b = \rho u_*^2$ (N/m^2)

Important concept here, is the averaging period relative to the domain. Bigger domains imply smaller averaging period and vica versa. With a domain of $9\delta x4\delta x\delta$, with $\delta = 1$ denoting the channel half-height, 500s are taken as an average period. The resulting y^+ value in the centroid of the first cell above the bottom, is shown in figure 4.1.
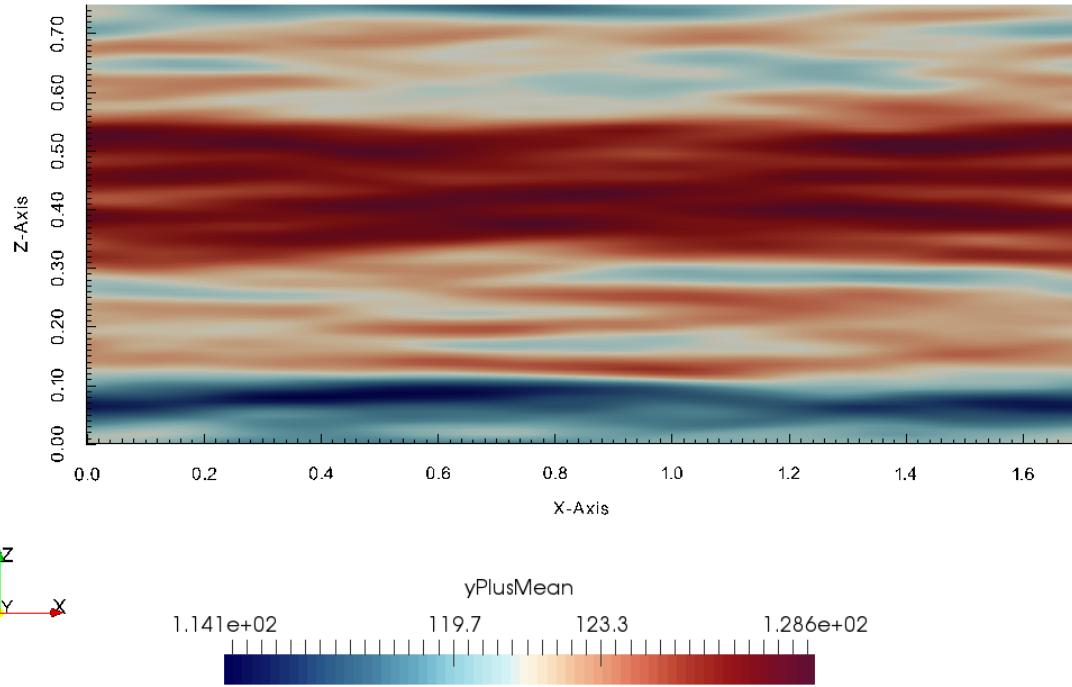
Figure 4.1: Overview of the y^+ values averaged over time in the first cell-centroid above the bottom wall, top view of the domain

Next the surface averaged value is extracted. In the case of figure 4.1, this is for example 123 and the height of the near wall cell is $\Delta y = 8mm$. Then we get to the model friction velocity by:

$$y^+ = \frac{u_* (\Delta y / 2)}{\nu} \tag{4.3}$$

It must be noted that, the solution has a streaky structure near the wall, resulting these "superstructures" when averaging over time. It is observed that the variations over the width persist more than the streamwise direction. Averaging in longer period results in less variation over the width. However it is considered that even at this state a consistent mean y^+ value can be extracted from the model.

Next, the simulation results are presented. At all cases, mean velocity profiles are sampled from the middle of the domain (see figure 4.2) and are compared with the theoretical log-law for rough surfaces. The resulting model friction velocity u_*, is compared with the theoretical one. The resulting error $\epsilon[u_*]$ is calculated from:

$$\epsilon[u_*] = \frac{u_*^{theoretical} - u_*^{model}}{u_*^{theoretical}} \% \tag{4.4}$$
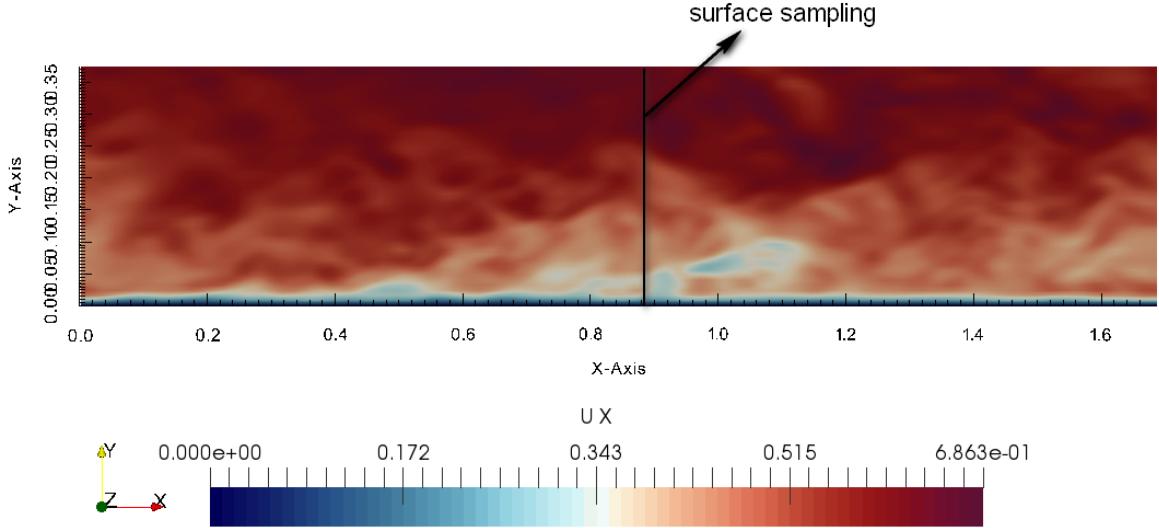
Figure 4.2: Instantaneous velocity field in of the open channel case. Fields are sampled from the middle of the domain.

First the results relative to different wall functions are presented. These are done with the WALE sub-grid model. A relatively coarse mesh is used, representing the upper limit of acceptable mesh sizes in such studies, as mentioned in section 3.1.2.
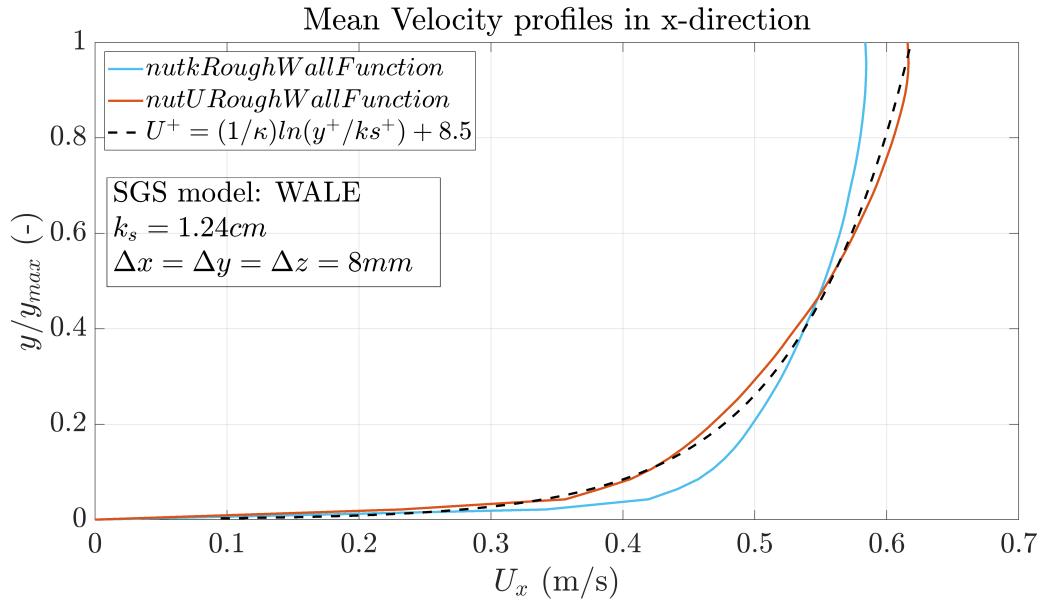
Figure 4.3: Mean velocity profiles of the open channel flow case using different wall functions

In figure 4.3, results of the `nutAtmWallFunction` are omitted since they coincide with the `nutkRoughWallFunction` ones. In figure 4.3 it is immediately seen that the `nutkRoughWallFunction` fails to predict the correct boundary layer in the near wall area. The depth-averaged velocity of the profile is correct, but the velocity gradients near the wall are quite different from the other two profiles. In this case, the profile is more full,resembling that of a smooth boundary layer case. Additional tests with the `nutkRoughWallFunction` are made with same mesh and varying the k_s magnitude. All cases produced the same result, equal to the one presented in figure 4.3. It is therefore concluded that in further sensitivity tests only the `nutURoughWallFunction` is used.

Next, two different subgrid models are used along with the `nutURoughWallFunction`. Results are presented in figure 4.4. As mentioned in the corresponding set-up section, the mass flux is fixed and therefore it is not clear from figure 4.4, which sub-grid model performs better.
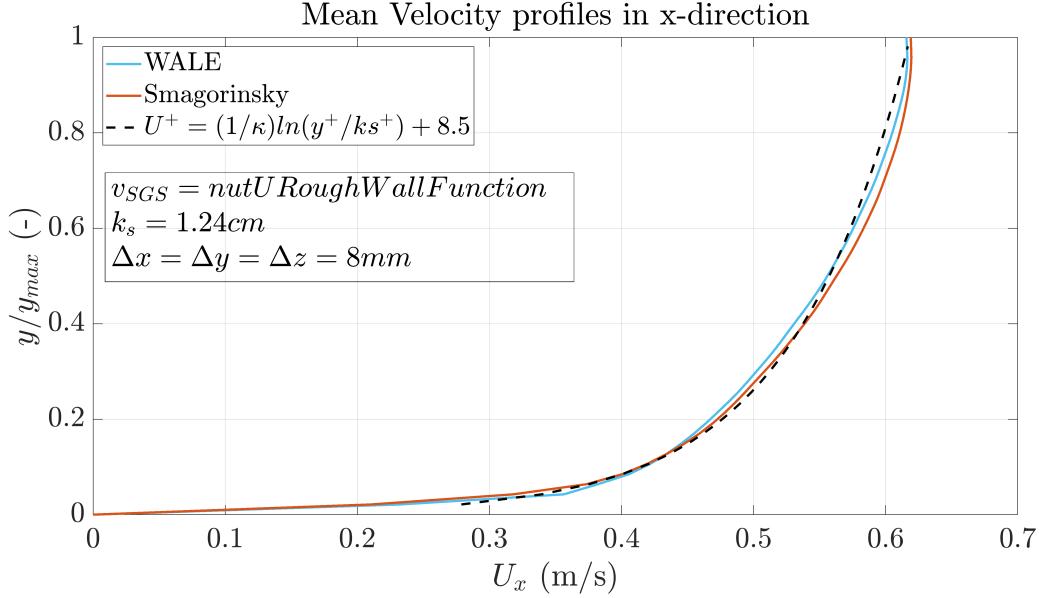
Figure 4.4: Mean velocity profiles of the open channel flow case using different sub-grid models

That being said, in figure 4.5, the mean flow velocity is made dimensionless with the friction velocity:

$$U^+ = \frac{u}{u^*} \tag{4.5}$$

It can be seen that both sub-grid models underestimate the friction velocity, leading to an error of 28% for the WALE model and 15% for the Smagorinsky model.
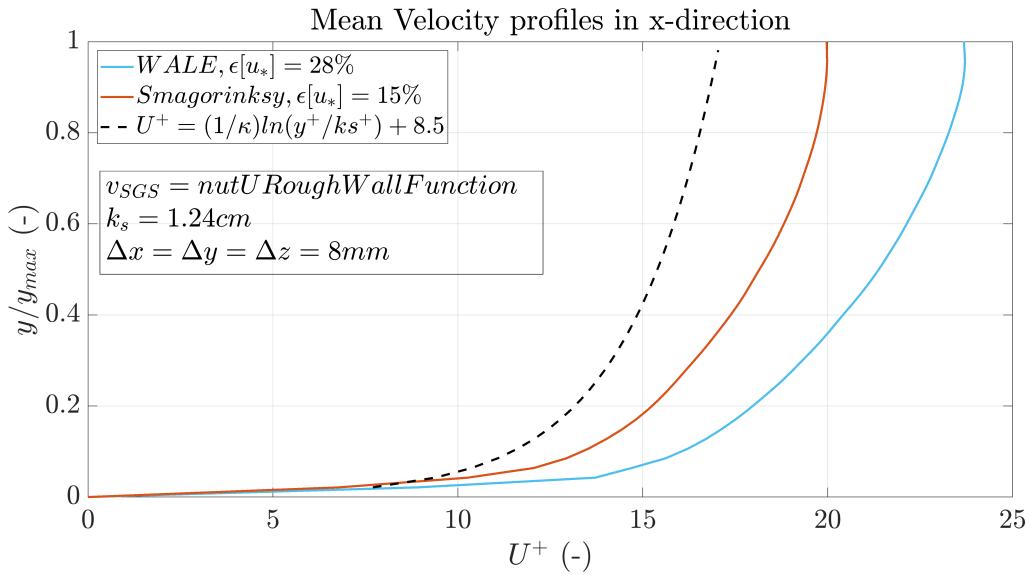
Figure 4.5: Mean velocity profiles of the open channel flow case using different sub-grid models: zooming in the near wall region

It is usually the practice in RANS simulations, that the sand roughness diameter k_s is set to be at most 20% larger than the cell size. With a k_s value of 1.24 cm, this would mean that cell sizes up to 1 cm would produce acceptable results. However, as can be seen from figure 4.6, even in this case the error $\epsilon[u_*]$ is about 28%, getting bigger for larger k_s to cell size ratios.
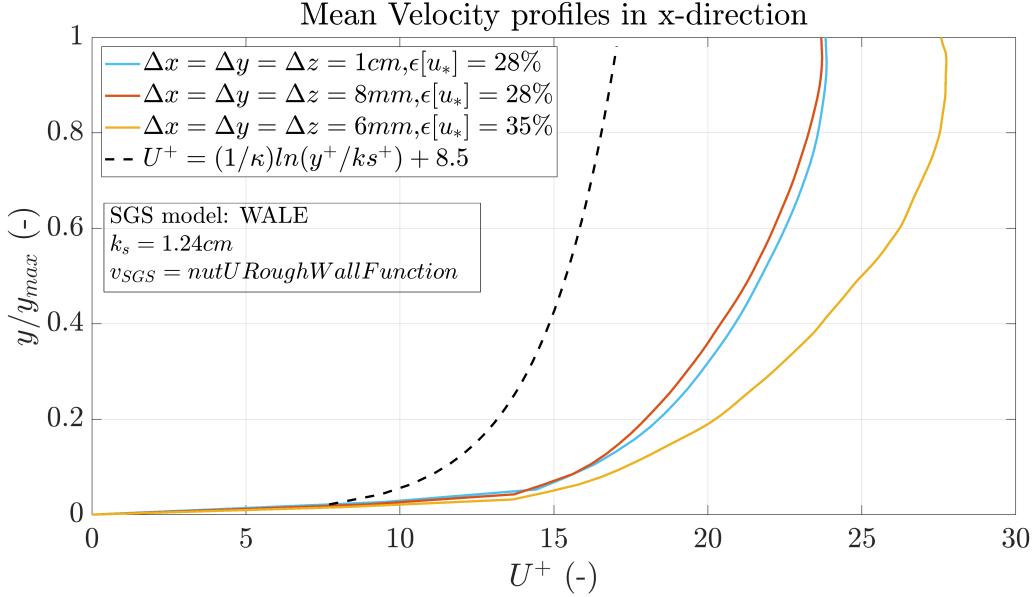
Figure 4.6: Mean velocity profiles of the open channel flow case using different k_s to cell size ratio with WALE subgrid model.

Lastly, the Smagorinsky subgrid model is used to test the sensitivity of the wall model to the k_s to cell size ratio. This is illustrated in figure 4.7. As in the case of the WALE subgrid model, the relative error seems to decrease for smaller k_s to cell size ratios. When this number is 80% or lower, the error seems to remain fixed 10%. This is better than the 28% relative error achieved when using the WALE subgrid model. Taking into account the uncertainty of the theoretical prediction discussed above, the final error $\epsilon[u_*]$ is estimated to be $8-10\%$.
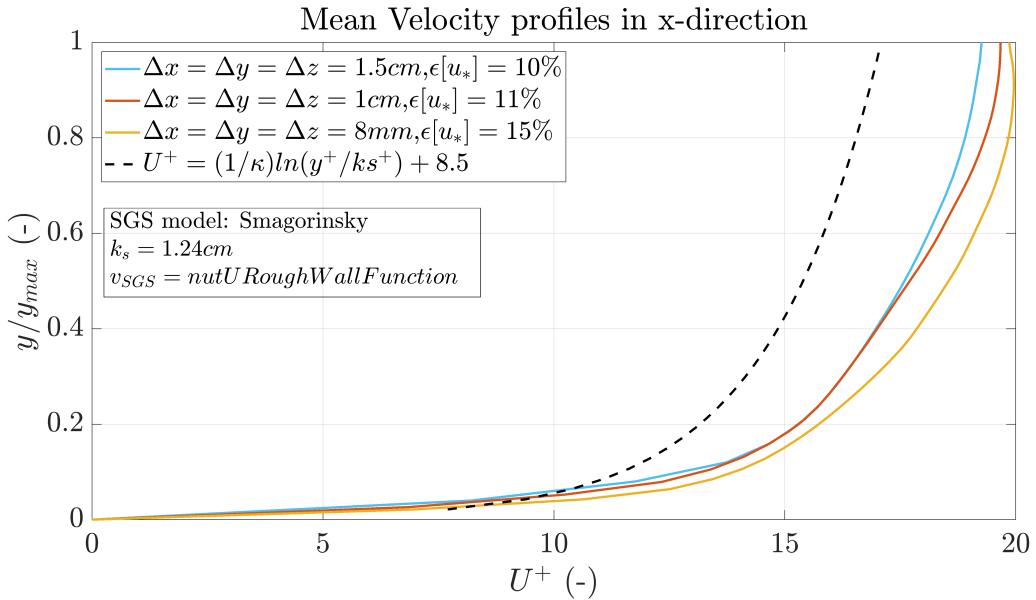
Figure 4.7: Mean velocity profiles of the open channel flow case using different k_s to cell size ratio with Smagorinsky sub-grid model.

Finally, it must be noted that,in absence of experiments, the theoretical log-law for rough surfaces is used. This was formulated based on the experiments of Nikuradse (1933). On the other hand, in OpenFOAM, the wall function implemented uses a different log-law for rough surfaces. Its exact origins could not be traced, but it is based on the work of Jayatilleke (1969).

As stated in section 2.2.3, the wall functions are modified to include the effect of wall roughness. This is done through ΔB which is a function of the size of roughness elements. Our case lies in the fully rough regime (see section 2.1.3) and ΔB is defined as:

$$\Delta B = \frac{1}{\kappa} ln(1 + Csks^+) \tag{4.6}$$
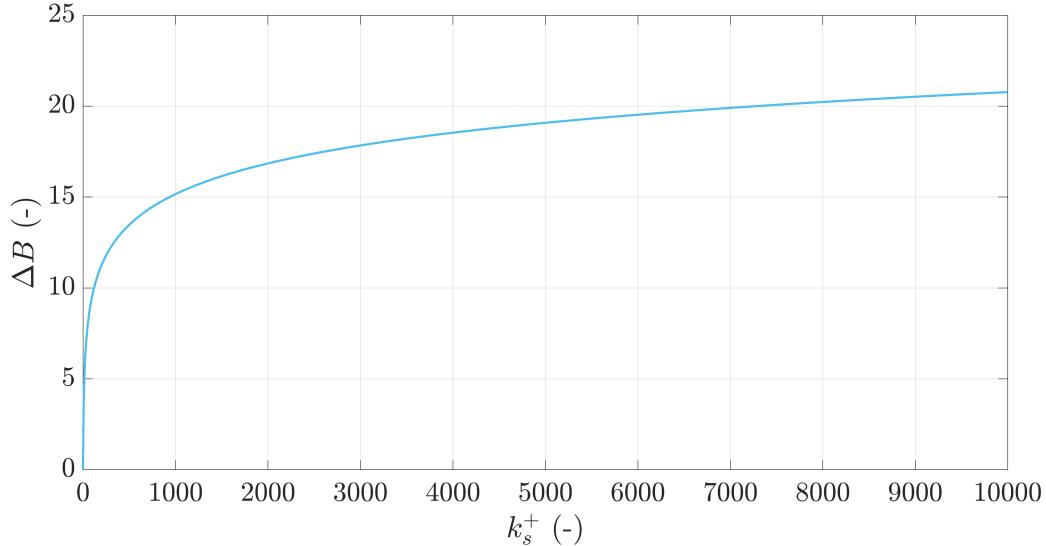
Figure 4.8: Relation between the equivalent sand grain diameter k_s and the roughness function ΔB

In figure 4.8, it can be seen how the ΔB responds with increasing k_s values. In our case, k_s is about 4500, meaning that we are in the regime where small changes in roughness (k_s), equals small change of the friction velocity u_*, certainly smaller than in the k_s <1000. On the other hand, the theoretical log-law of equation 4.2, does that have same k_s - ΔB relationship.

To get a better understanding of the latter remark, the two log-laws are plotted assuming the same friction velocity u_* and roughness k_s in figure 4.9. The resulting error in mean velocity U is estimated to be 9%.
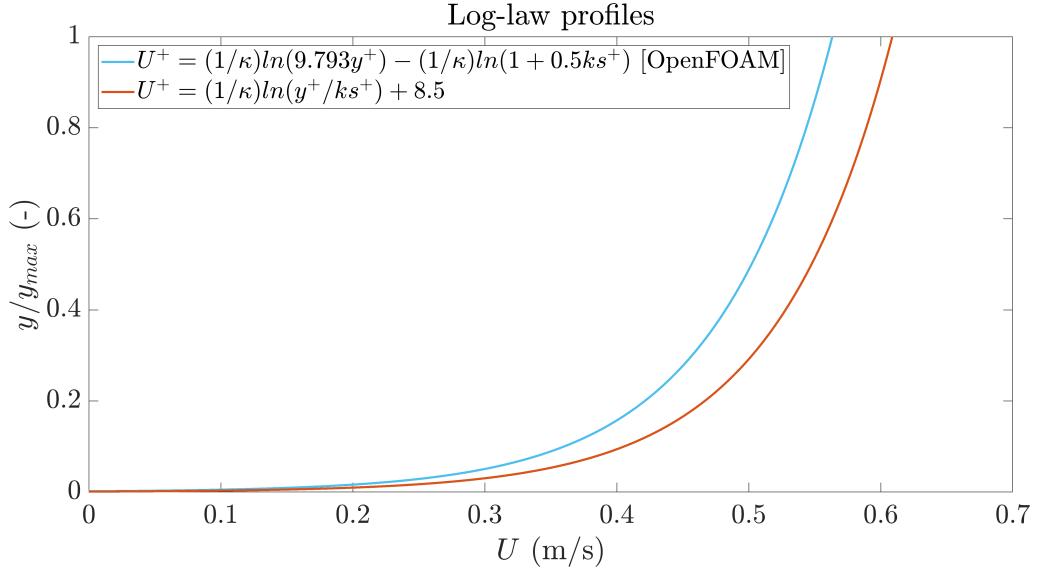
Figure 4.9: Relation between the equivalent sand grain diameter k_s and the roughness function ΔB

4.2. RANS long sill

In this section, the results of the RANS long sill case are presented shortly. These serve as an initial condition for the WMLES case. Since these results were available prior to the WMLES results, it would be useful to discuss these in short to get an idea of points that need special attention later in the WMLES long sill simulations. In addition, as stated in section 3.1.3, the discharge in the inlet boundary condition, needed adjustment in the previous studies simulating the present experiment, in order to result in a good validation. In this study, the discharge prescribed is the experimental one without adjustment. This choice is further examined below.

For the purposes of this simulation, wall sensitivity tests are undertaken and presented in appendix C. Following up on those, the $k - \omega$ SST and realizable $k - \epsilon$ models are tested.

In figure 4.10, the mean velocity profiles in the center over the width of the domain are presented for the two models tested. It can be seen that both models show similar results in cross sections 10,1 and 9. Both models seem to underestimate the magnitude of the separation behind the sill in cross section 2, while in the realizable $k - \epsilon$ model the recovery after the reattachment point happens faster (crosse sections 3 and 5). A quantitative comparison of the results is available in table 4.1. The relative error ϵ[%] is calculated by taking the average absolute error of all the measured points in a cross section and dividing that by the maximum velocity per measured cross section. It can be seen that the $k - \omega$ SST model produces better results than the realizable k-ϵ model. However, the magnitude of the errors (see table 4.1), do not allow a safe conclusion on the mass flux to be used in the inlet. Furthermore, non physical asymmetries over the width of the domain where present in the 3D RANS case. In the absence of measurements over the width, it is difficult to quantify these asymmetries. Further investigation of these is not presented here since its deviates from the scope of this thesis. However, at this point it was decided that a simple 2D RANS simulation with the $k - \omega$ SST model will be done to inspect the results without the present of the side walls. The inlet boundary conditions was adjusted to the 2D case accordingly.

Mean Velocity profiles in x-direction
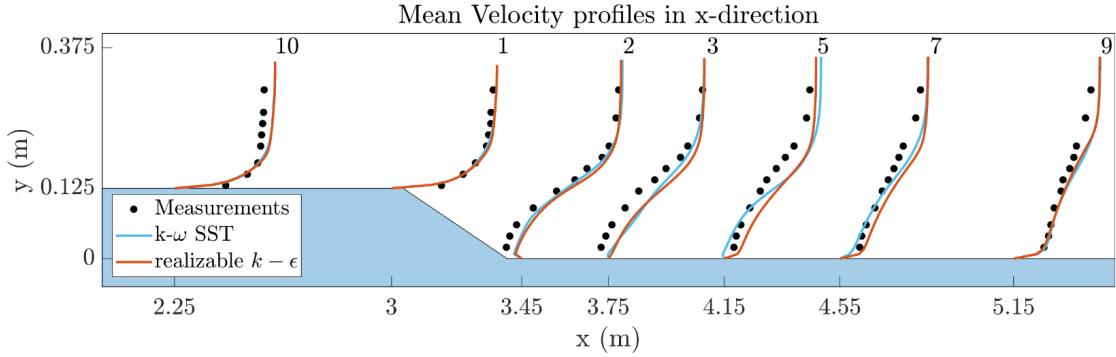
Figure 4.10: Mean velocity profiles for the RANS long sill case

Turb. Model/Cross Section	10	1	2	3	5	7	9
k- ω SST	17.18%	3.28%	5.29%	11%	9.7%	4.7%	4.5%
realizable k- ϵ	17.31%	3.9%	8.47%	12.95%	12.75%	8.9%	3.6%

Table 4.1: Error ϵ[%], between the experimental results and the numerical model output for the RANS 3D long sill case

The results of the 2D case can be seen in figure 4.11. As can be seen, the results are now better than the 3D RANS case, lower than 5% in all cases except for cross sections 10 and 9. From these it can be concluded that CONTENYT

Mean Velocity profiles in x-direction
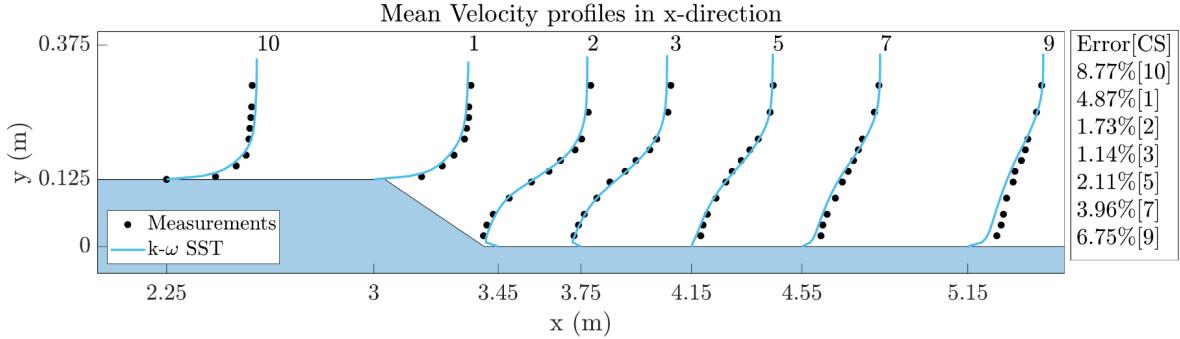
Figure 4.11: Mean turbulent kinetic energy profiles for the RANS long sill case

4.3. WMLES long sill

Lastly, the model results of the WMLES case are presented. Four different subgrid scale models are tested, namely the WALE sunbgrid model, the Smagorinsky subgrid model, the dynamic version of Smagorinsky model and the k-equation model. A description of the models can be sound in section 2.2.2. Two different mesh sizes are tested for each model, as discussed in section 3.3.1. The most important results are presented below.

First, results of the WALE and Smagorinsky sub-grid model on the coarse mesh are given qualitatively. In figure 4.12, the validation of the mean velocity profiles is depicted. A large difference in the performance of subgrid models is immediately realized. More specifically, both models seem to have a good agreement with measured mean velocity in cross section above the sill, namely 10 and 1. However, the WALE subgrid model seems to fail in predicting separation in cross sections 2 and 3. The Smagorinsky model performs better in these regions, giving good results in cross section 3.
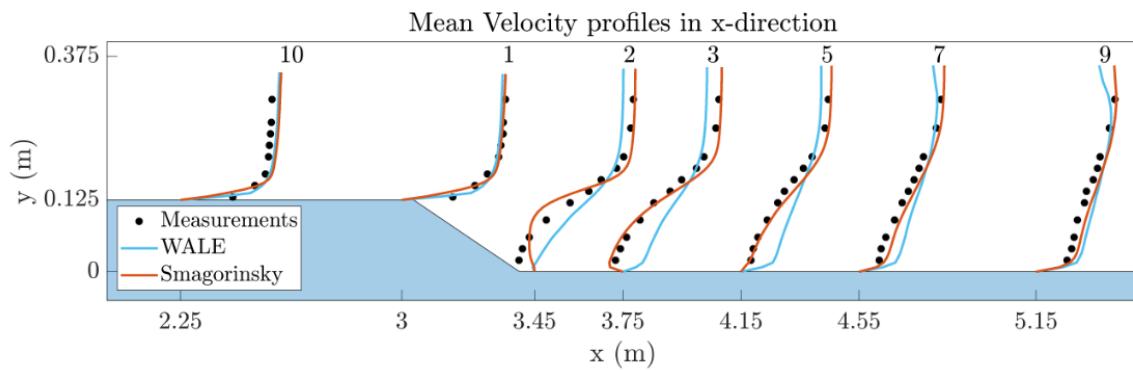
Figure 4.12: Averaged measured and simulated velocity profiles with the coarse mesh

Results produced using the k-equation and dynamic Smagorinsky model are seen in figure 4.13. More specifically, the Dynamic Smagorinsky model seems perform similarly to the WALE model, while the k-equation model produced results in agreement with Smagorinsky model.
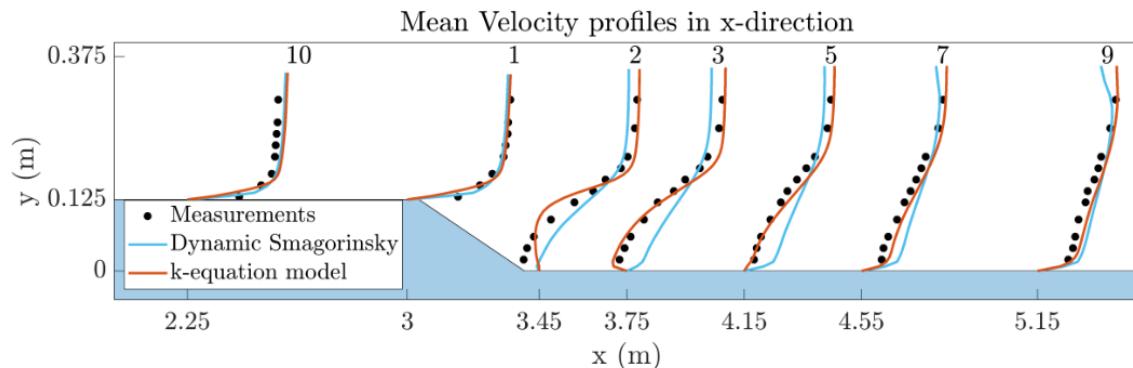
Figure 4.13: Averaged measured and simulated velocity profiles with the coarse mesh

Next, model results using the fine mesh as described in section 3.3.1 are presented.
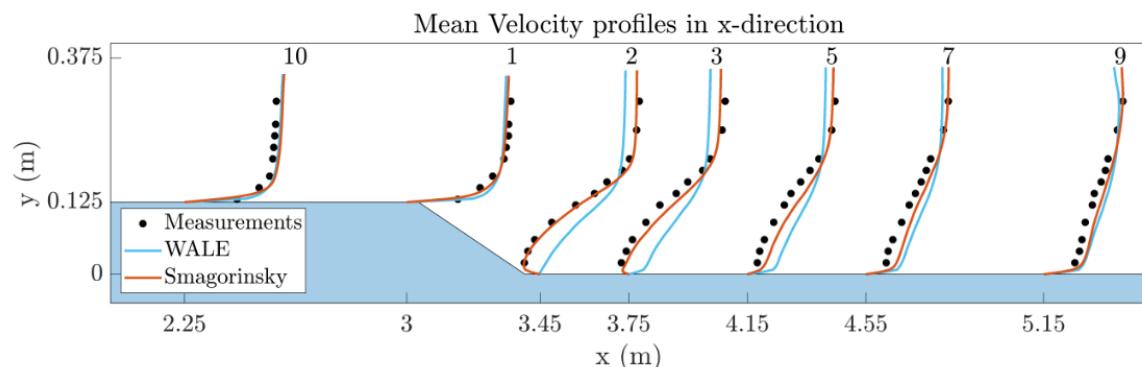
Figure 4.14: Averaged measured and simulated velocity profiles with the fine mesh

In figure 4.14, it can be seen that the refinement improved the results of the Smagorinksy subgrid model, while the results of the WALE model remained almost the same. More specifically, in cross sections 2 and 3 the separation is well-predicted by the Smagorinsky model, while the WALE model again fails to predict any separation at all. As a result, the recovery of the WALE velocity profile starts already in cross section 2. In cross sections 5,7 and 9 the depth-averaged mean velocity of the model is slightly larger than the measured one for both models.
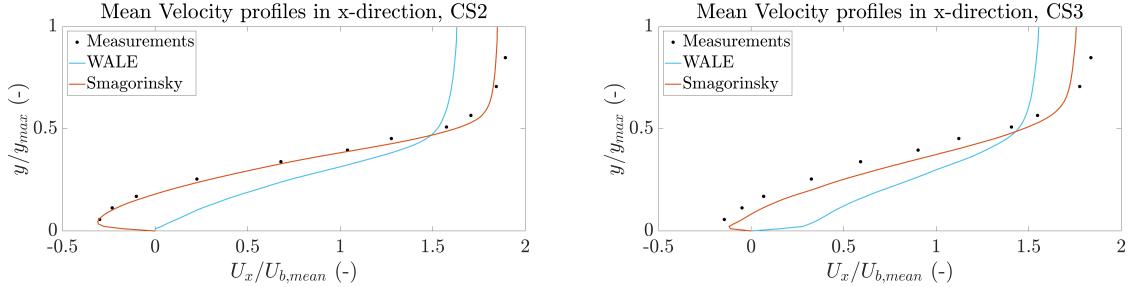
Figure 4.15: Averaged measured and simulated velocity profiles with the fine mesh in cross section 2 (left) and cross section 3 (right)

In figure 4.15 we zoom on the mean velocity in cross sections 2 and 3. The Smagorinsky model seems to perform remarkably good in predicting the separation especially in cross section 2.
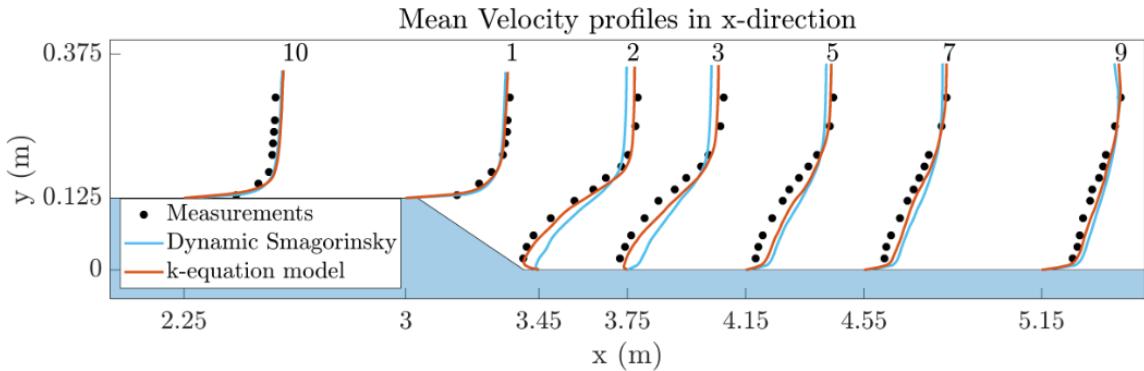
Figure 4.16: Averaged measured and simulated velocity profiles with the fine mesh

Concerning the k-equation model and dynamic Smagorinsky, again the bigger difference is in predicting the separation. The dynamic Smagorinsky seems to fails in that task, while the k-equation model have a performance comparable to the Smagorinsky model elaborated above (see figure 4.16).

In figure 4.17, the instantaneous velocity field in streamwise direction for both meshes used is presented. It can be seen that only with a fine enough mesh, the initiation of the mixing layer is predicted correctly. In the case of a smaller grid, more flow scales are resolved in the mixing layer and less are modelled. In addition, since also a smaller time step is used for the smaller mesh case, spatial integration error and time integration error could both result in the differences of coarse and fine mesh.

coarse mesh

U X
-2.723e-01   0   0.34   0.67   1.075e+00
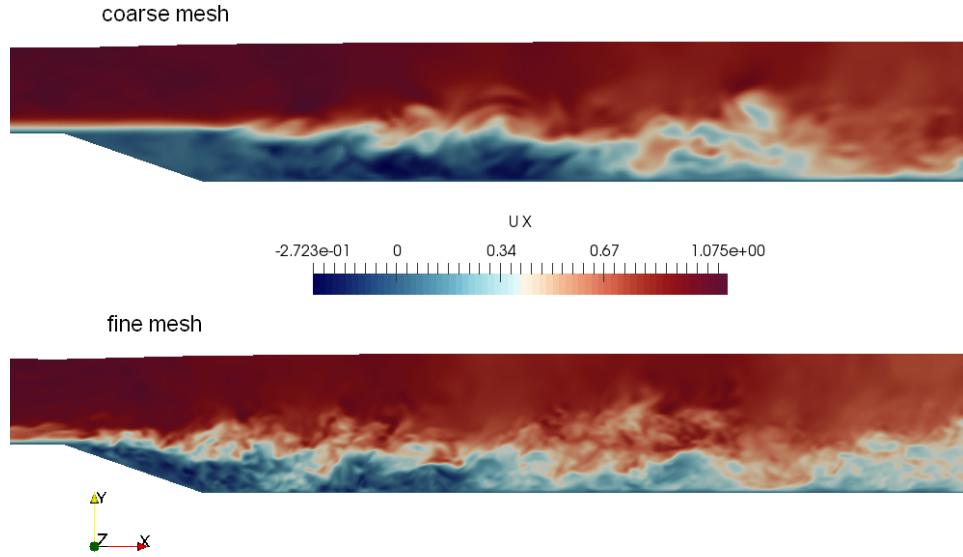
fine mesh

Figure 4.17: Instantaneous streamwise velocity field of the Smagorinsky model in coarse and fine mesh

From the above it can be concluded the Smagorinsky subgrid model seems to perform best. As presented in section 2.2.2 of the literature review, the Smagorinsky model is strictly dissipative. In figure 4.18 the results are shown of the instantaneous ν_{SGS} field for the Smagorinsky and the dynamic Smagorinsky model, around the same time instance. In both models the same mesh is used. In regions where high ν_{SGS} or nut values are present, smaller eddies are located that the current mesh cannot resolve. It is can be seen that the Dynamic Smagorinsky model is indeed less dissipative than the standard Smagorinsky one. However near the wall, it seems that the Dynamic Smagorinsky model performs worse. It must be noted that results of mean ν_{SGS} value of the two models yield the same conclusions. The instantaneous ν_{SGS} field is shown here for illustration purposes.

Smagorinsky

Dynamic Smagorinsky

nut
0.000e+00   1.1e-5   2.2e-5   3.3e-5   4.438e-05
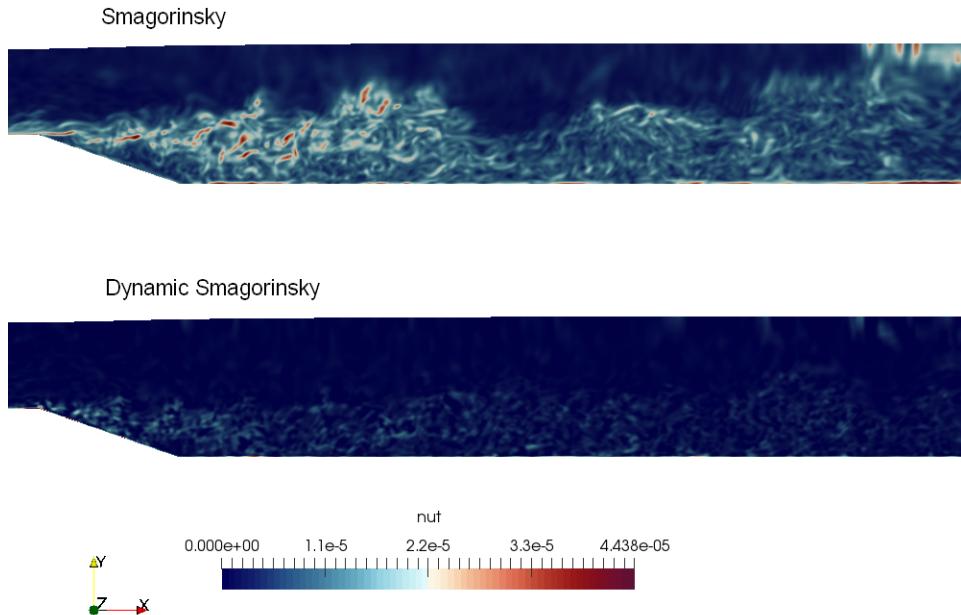
Figure 4.18: Instantaneous subgrid scale viscocity field ν_{SGS} in the case of Smagorinsky and Dynamic Smagorinsky models. The same mesh is used in both models.
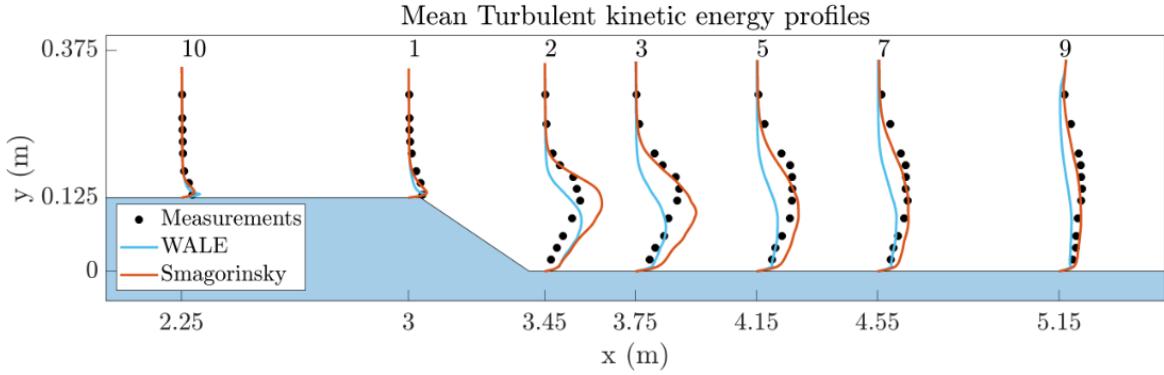
Figure 4.19: Averaged measured and simulated TKE profiles with the fine mesh

The mean turbulent kinetic energy profiles of the WALE and Smagorinsky models can be seen is figure 4.19.
Both the resolved and the modelled turbulent kinetic energy in included in the numerical results. In cross
sections above the sill, both models produce similar results and in accordance with the measured ones. In
cross section 2, the Smagorinsky model seems to overpredict the mean TKE on the first 15 cm above the bed.
This continues in cross section 3, where an overprediction can be seen for the first 13 cm above the bed (see
also figure 4.20). In cross section 5,7 and 9 the overprediction of the TKE is less, leading to a better agreement
with the measured profiles (figure 4.20).
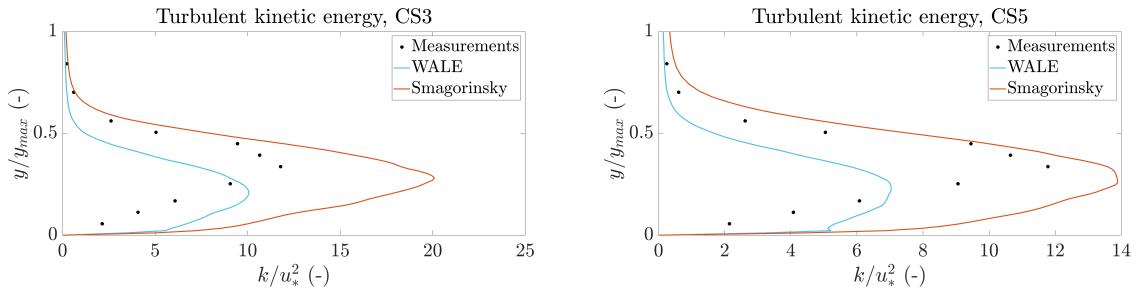
Figure 4.20: Averaged measured and simulated TKE profiles with the fine mesh in cross section 3 (left) and cross section 5 (right)

In figure 4.21 the energy density spectra in cross section 3 can be seen which is located in the shear layer. An
under prediction of the amount of turbulent kinetic energy can be seen especially for frequencies under 1 Hz.
After that, the measured and simulated TKE converge until a frequency of 21 Hz, where the red line drops.
Similar results are found in cross sections 4 and 5 (figure 4.22). It must be noted that at all cases the shape of
the measured and simulated spectrum are in agreement with simultaneous peaks and lows.
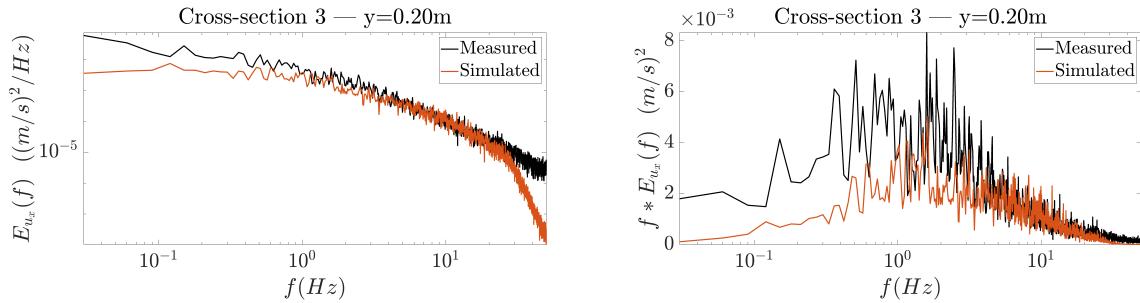
Figure 4.21: Energy density spectrum in cross section 3, 20 cm above the bed
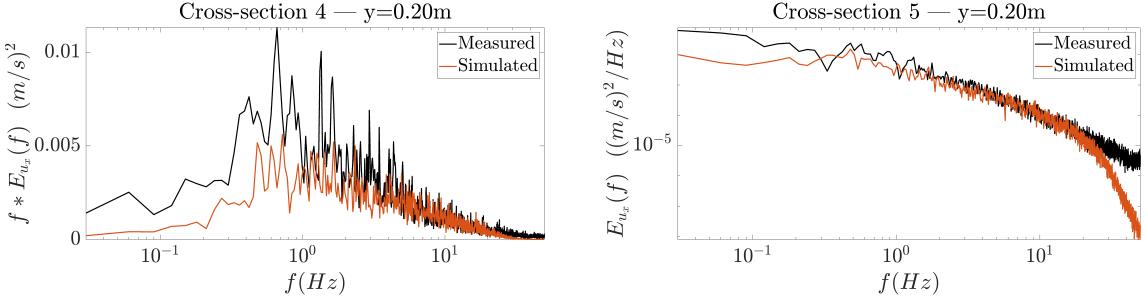
Figure 4.22: Energy density spectrum in cross section 4 (left) and 5 (right), 20 cm above the bed

Next, a comparison is done with the measured and simulated signals, at a lower location, 9 cm above the bed. As can be seen from figure 4.23, the mismatch is improved. Similar results of energy density spectra 9 cm above the bed are also observed in the other cross sections.
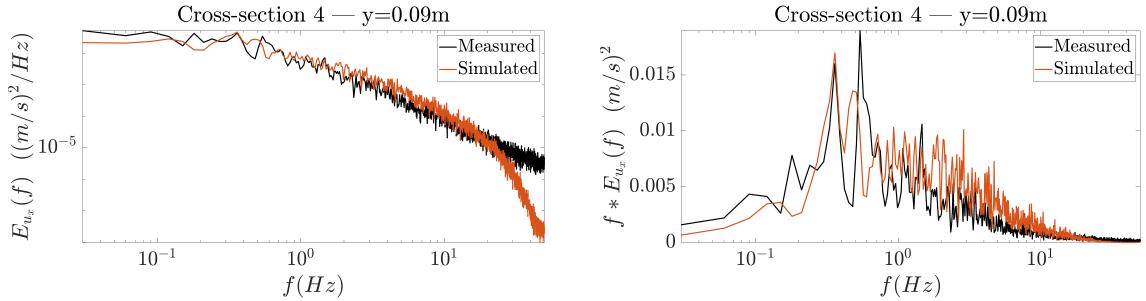
Figure 4.23: Energy density spectrum in cross section 4, 9 cm above the bed

A possible cause of difference in the measured and simulated energy density spectrum could be the inflow boundary condition. In Sagaut (2006), the strong dependence of the mixing layer and the inflow perturbations is mentioned. In our case the flow dynamics downstream the sill are dependent on the development of the mixing layer, making the inflow boundary condition very important. It is noted that in this study a synthetic turbulence generation method as suggested by Poletto et al. (2013) is implemented, which is described in selection 2.2.2. After the simulation was finished it was discovered that there is some discrepancy about a coefficient of the method, namely the C coefficient in equation (13) as given in Poletto et al. (2013) and its implementation in OpenFOAM. In the present study, no further investigation was undertaken, so that no conclusion can be made that this is the source of overprediction of turbulent kinetic energy. However, having said that the mixing layer development is sensitive to the inlet boundary condition, it is important that further investigation on this synthetic turbulence generation boundary is done in future works.

In the near wall region, wall turbulence and TWPs are at play. Since a wall function is present and the first grid point is located at y^+ larger than 30, the inner boundary layer (viscous and buffer layers) are not resolved. Close to the wall, the flow consists of pockets of fast and slow fluid that organize in flow streaks. These migrate slowly outward in the boundary layer (ejection) and are subject to instabilities that make them explode near the outer edge of the inner region. A fast fluid them arrived from above and sweeps that near wall region. Sagaut (2006). It must be understood that these effects, while relevant for stone stability are not resolved. With the mesh size used in the present thesis, the region 1-2 stone sizes above the bed is resolved, but the dynamics below that height, responsible for stone movement are not resolved. They are left for sub-grid scale treatment. Since the above mentioned mechanisms are highly anisotropic, it is expected that the sub-grid model performs poor is predicting them.

However, the energy density spectrum close to the wall is investigated, to get an idea to the higher frequency resolved in the numerical model. In figure 4.24, energy density spectrum 2 cm above the bed is depicted. This is the point measurement closest to the bed. In both cross section, frequencies up to 10 Hz are resolved. In cross section 5, the frequency corresponding to 1 d_n^{50} is 16 Hz, meaning that the highest frequency resolved is close to the higher frequency relevant for stone stability.
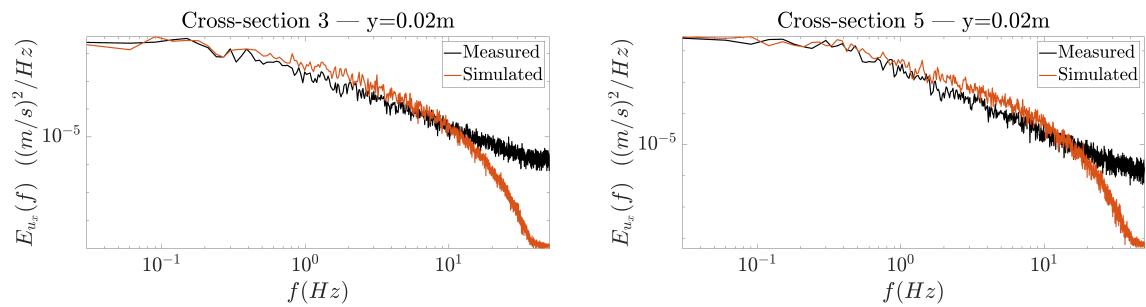
Figure 4.24: Energy density spectrum in cross section 3 (left) and 5 (right), 2 cm above the bed

5

Discussion

Some reflection on the choice and the adequacy of the Jongeling et al. (2003) experiment is presented here. During the first month of this thesis, an investigation of relevant experimental sets was undertaken leading to the selection of the long sill case of the Jongeling et al. (2003). An overview of other choices considered, is included in section 2.3.1. An advantage of this experimental set-up was the fact that both hydraulic data and stone displacement was measured, so that it made it possible for next students to continue this study. Concerning the measured velocities, point measurements were taken. To the author's knowledge no experiments are available were PIV is used for flow field measurements and also stone displacement is measured for the purposes of this research area.
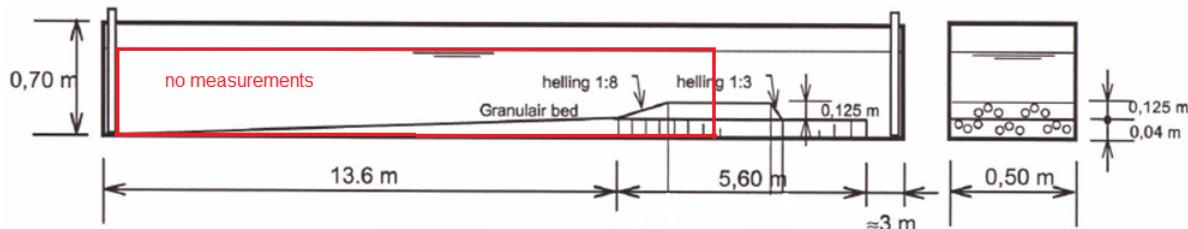
Figure 5.1: Geometry model of the cyclic LES simulation

While building a "numerical twin" of this experiment, some challenges are recognized. In figure 5.1, it can be seen that in the first 13.6 m no measurements are taken. Physically, these first meters, are necessary for the inflow velocity profile to recover from perturbations introduced by the pump in the beginning of the flume and also to develop a canonical turbulent boundary layer before the area of interest. Embedding this area in the model domain was not possible due to computational limitations. As a result the inlet was placed 4 steps height away from the sill. In case velocity measurements along with turbulence data were available before the sill, these could have been used in the model inlet boundary condition. This would eliminate uncertainties regarding the inflow boundary and speed-up the simulation set-up. In addition, no information was available on the flow field over the width. In RANS simulations, the resulting flow was asymmetrical over the width, but no comparison or reference to the experiment could be made.

It must be noted however that this experimental set-up could serve its aim, namely to help in creation of a stability formula of the needed complexity in work of Jongeling et al. (2003). It is logical that more sophisticated numerical models are in need of more detailed experimental measurements. For example, a better description of the bed and the flow conditions as close to the bed as possible would help to validate numerical models in the near wall region and motivate other bed treatments than the wall function approach.

Nature of the application

After conducting the literature review in section 2, it can be concluded that the application of interest in this study has two characteristics that pose challenges to the numerical modelling and make the application itself unique. First, since we are dealing with engineering flows, high Reynolds numbers are present, namely of the order of 10^8. In the present study since the validation case came from an experiment a Reynolds number of 10^6 was at play. Secondly, as explained in section 2, a scale resolving technique must be applied, so that the numerical model is able to predict extreme forces that cause stone displacement. In addition, it was stated, that the numerical model must be able to predict high frequencies, roughly corresponding to the stone size length scale and capture the flow eddies at a distance equal to the 1.5 times the stone size above the bed. These two features make the computational demands very high and the implementation of numerical modelling far from trivial.

Wall-modelled LES is indeed an attractive solution for applying a scale-resolving technique in engineering flows. However, studies of this type usually deal with an order of magnitude smaller Reynolds number flows of 10^5 (Mukha et al. (2018), Balen (2010),Stoesser et al. (2010), Hinterberger et al. (2007)). In addition, only in case of Mukha et al. (2018) this was done on a general-purpose software for computational fluid dynamics.

To get an idea of how expensive is such a simulation, it is noted that 3 minutes of simulation time are equivalent to one month of real time. Moreover, in order to capture the shear layer development and reach the target stone frequency, a 4 mm mesh was used leading to 12 million cells. As can be seen in figure 3.6, only in the first 20 cm a homogeneous mesh could be afforded. An expansion ratio was applied in the upper water column leading to coarser cells near the surface. A compromise was set between resolving eddies and computational time.

Free and wall turbulence sto WMLES

Another challenge that this application is posing is that the stone elements to be simulated fall in the fully rough regime. On one hand, small cell sizes must be used to capture as much flow scales as possible until the stone size and on the other hand, as seen in figures 4.6 and 4.7 the equivalent sand grain diameter must be of the order of magnitude of the cell size or less. In case this direction was followed for the simulation of the long sill, a cell size of 1.24 cm should have been used. However, as seen in figure 4.17, already a cell size of 8 mm was not enough to capture the development of the shear layer.

In addition, it can seen that the best result of the open channel flow case (figure 4.7) still resulted in an under-prediction of the wall shear stress by 10%. From the above it can be concluded that in the fundamental case of open channel flow, where wall turbulence is solely responsible for the correct development of the boundary layer and shear stress, rough wall functions seem to introduce errors. On the long sill case, where free turbulence and geometry induced flow features were also an important trade-off had to be made between underpredicting wall shear stress and underpredicting the shear layer development.

That being said, it is expected that in the affinity of hydraulic structures were mixing layers are absent and the focus is on wall induced turbulence, the present model is not an attractive choice.

Wall function performance

Since no systematic reporting was found in literature for the application of WMLES for rough surfaces within OpenFOAM, sensitivity tests were performed and results are available in section 4.1. First of all, it is concluded that only the `nutURoughWallFunction` can be used to produce sensible results (see figure 4.3). In section of wall functions in 2.2.3, the implementation of the `nutURoughWallFunction` and the `nutkRoughWallFunction` is explained in detail. Both functions, use a modified viscosity ν_w, to account for the correction of the velocity gradient near the wall. The `nutURoughWallFunction` is based on the velocity to arrive to an expression of ν_w, while the `nutkRoughWallFunction` is based on turbulent kinetic energy. In case of RANS simulations all the kinetic energy is modelled and the `nutkRoughWallFunction` performs well (see also appendix C). However, in the LES environment it is hypothesized that the sub-grid kinetic energy is used instead of the resolved one, so that the use of this wall function leads to large error.

Concerning the error itself, the minimum error was found when the Smagorinsky model was used for a cell size to D_n^{50} ratio of 2.4 and it was 10%. A comparison of the wall function used in OpenFOAM and the theoretical log-law used for validation (equation 4.2), yielded an error of 9% (see figure 4.9). This means that no solid conclusions can be drawn from the validation by a theoretical log-law and a comparison with experiments or DNS data could provide a quantitative error. This is also recommended as future work.

The SGS model in the WMLES environment

Four different sub-grid models are applied in the long sill case. More specifically the Smagorinsky model, the Dynamic Smagorinsky model, the WALE model and the k-equation model. At all cases the `nutURoughWallFunction` is applied in the bottom wall. From the validation of mean velocity profiles and turbulent kinetic energy with measured ones, it can be concluded that remarkably similar results are found when using the Smagorinsky and the k-equation model. In addition, the WALE model produced similar results with the dynamic Smagorinsky model.

It must be noted that it is not surprising that different results are produced with different models. Still in 4 mm, the mesh cannot be characterized as fine enough, so that the sub-grid models are important. Thus the results are sensitive to that. The surprising thing is that especially the WALE model produced, worse results that the Smagorinsky model, despite the fact that the WALE model has a special treatment near the wall (see section 2.2.2).

The Smagorinsky sub-grid model is based on the resolved large scales. It is based on the hypothesis of local equilibrium, namely the production and dissipation through the cut-off frequency are equal. The above ensures that the right amount of TKE is dissipated in the smaller scales but this often happens too quickly. This is also evident in our case by comparing the ν_{SGS} field, of Smagorinsky with the Dynamic Smagorinsky model (figure 4.18). Another shortcoming of the Smagorinsky model is that the ν_{SGS} does not reduce to zero in the viscous sub-layer, in which turbulent fluctuations should be damped as impermeable surfaces. However it that be argued that since we use a wall model near the wall this is not relevant in this study.

On the other hand the dynamic Smagorinsky model and the WALE model are also algebraic models but they adjust the model coefficient to adapt to the local flow state.

The source of this difference should have its origin in the boundary layer itself. It seems that the dynamic procedure and the wall functions cannot be applied in the same time without conflict, at least for a near wall y^+ larger than 30.

As a concluding remark it is noted that the concept of WMLES relies on the fact that the the turbulence in the log-law and above is fairly independent of what happens closer to the wall. This allows us to keep, say, the turbulent kinetic energy peak at $y^+ = 15$ Sagaut (2006) unresolved and still get sensible results. However in the near wall region, even at $y^+ = 30$, it appears that special treatment for the ν_{SGS} is needed.

Performance of WMLES in comparison to IDDES

In section 2.2.1, the limitations of the IDDES model were highlighted and the reasons that led to the choice of WMLES as a next step in this study were indicated. On the basis of that, some qualitative comparison of WMLES and IDDES is made in the following.

In figure 5.2, an instantaneous plot of the velocity field in streamwise direction in both WMLES output(this thesis) and IDDES output(Stevens (2018)), can be seen. In the latter, the delay on the initiation of the shear layer was attributed to the presence of RANS region (see also figure 2.12). A better development of the mixing layer can be seen in the WMLES output. This is further investigated in the following.

It must be noted however that a one to one comparison of the IDDES and WMLES results is not possible because different numerical software (StarCCM and OpenFOAM respectively) and modelling techniques were used. A comparison of each of one of them with the experimental results is more sensible.
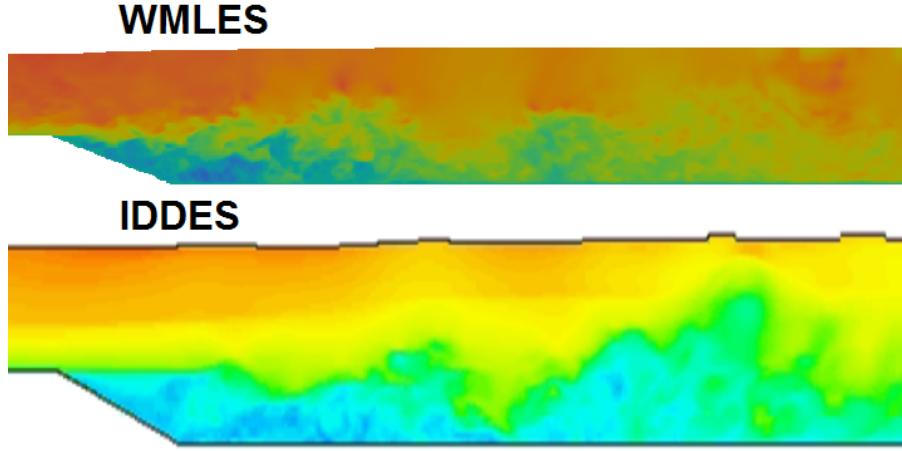
Figure 5.2: Instantaneous velocity profile downstream the sill

First, the performance of the models is evaluated based on the mean velocity profiles. This is illustrated in a qualitative sense in figure 5.3. The measured velocity profiles above the sill seem to agree more with the ones produced by the WMLES. In cross sections 2 and 3 separation is present. In case of WMLES and also in the experiment maximum negatives velocity were found in cross section 2. This is captured almost perfect by the WMLES. In the IDDES results, maximum negative velocities are present in cross section 3. This is in agreement with the argument that there is a delay in the mixing layer initiation also shown in figure 5.2. In the recovering area, IDDES seems to underpredict the mean velocity, while the WMLES is overpredicting it.
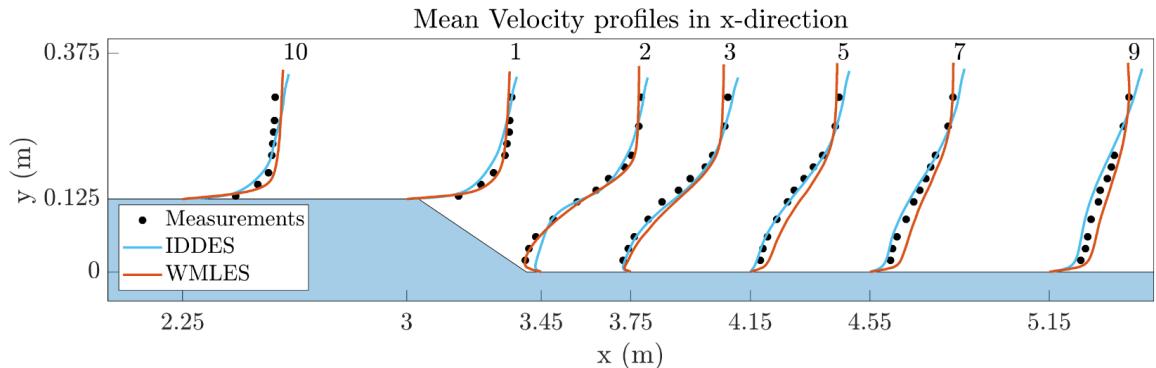
Figure 5.3: Mean velocity profiles in IDDES and WMLES

In terms of mean turbulent kinetic energy, both models seem to be in agreement with the measured TKE above the sill. In cross section 3, the IDDES seems to underpredict the TKE at all points, while the WMLES overpredicts the TKE in the lower 15cm of the domain. Similar results in comparison with the measured ones are present in cross sections 7 and 9.

Finally, in figure 5.5, the energy density spectrum in cross section 5 and 2 cm above the bed is depicted. The sampling frequency of the experiment was 100 Hz. A probing time interval of 0.01 s is used to create a velocity signal out of model results. For frequencies lower than 1Hz, the IDDES and measured results seem to be in good agreement while the WMLES underpredicts the amount of TKE in lower frequencies. At 2 Hz the yellow line drops quickly, meaning that the higher frequency resolved in the IDDES is about 2 Hz. In contrary, the higher frequency present in the WMLES is about 30 Hz, larger than the corresponding stone frequency of 16 Hz (section IDDES in 2.2.1).
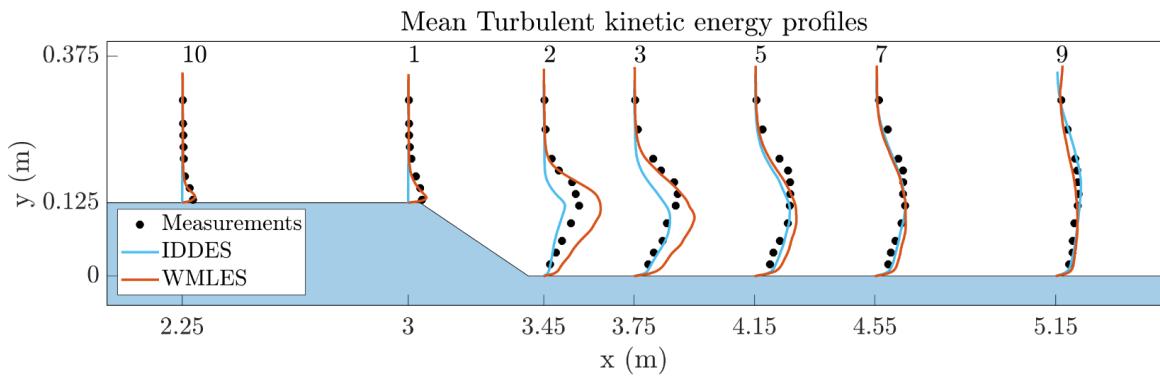
Figure 5.4: Mean turbulent kinetic energy profiles in IDDES and WMLES
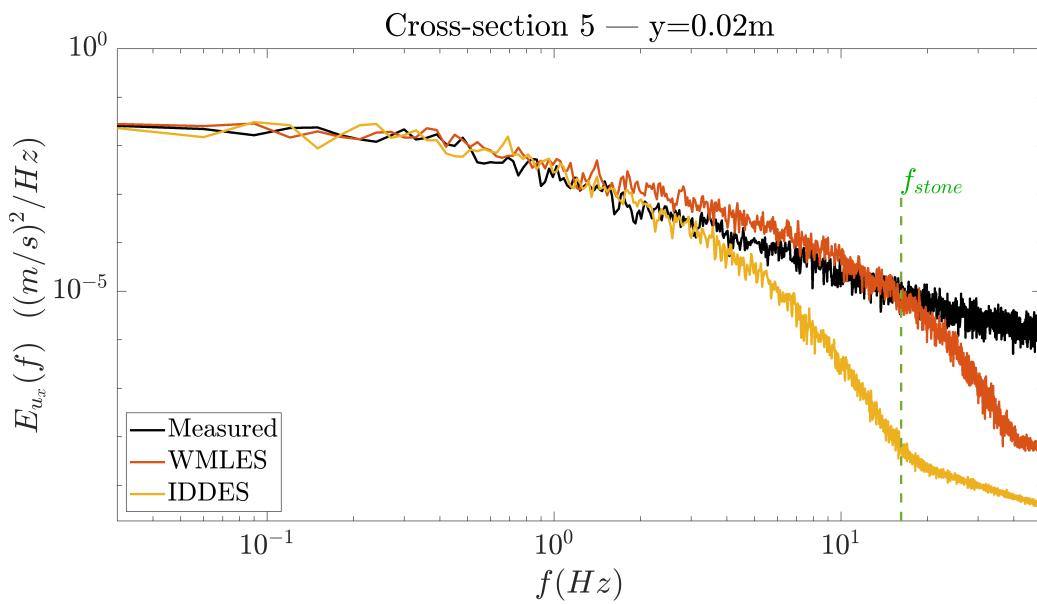
Figure 5.5: Comparison of the energy density spectrum in cross section 5, 2 cm above the bed between the IDDES and the WMLES.

6

Conclusions

The research objective of this study was formulated in chapter 1 as follows:

To establish a hydrodynamic numerical tool that predicts the governing mechanisms associated with bed stability in non-uniform flows

To that end, the numerical software OpenFOAM was selected and the motivation for that is given in section B. The experiment which was used in the numerical modelling comes from the Jongeling et al. (2003) experimental set. Motivation and description of that can be found in section 2.3. The present thesis continues a research line in the framework of stone stability. Previous works done include Steenstra et al. (2016) and Stevens (2018).

Before the main question is addressed, an answer will be given for the five sub-questions posed.

How can the previously applied IDDES model be improved for predicting stone stability?

Further post-processing of the numerical results coming from the study of Stevens (2018), revealed the limitations of the Improved Delayed Detached Eddy Simulation model (IDDES). These are presented in section 2.2.1 and based on the analysis it is concluded in section 2.2.4 that the WMLES is the next numerical modelling technique to be applied for the purpose of simulating the flows of interest. More specifically:

- In section 2.2.1 it was seen that the initiation of the shear layer after the sill in the case that the RANS region is present right above the bed in the IDDES model, is delayed (see also figure 2.12). The mixing layer is an important region because as explained in section 2.1.4, large eddies coming from this region attack the bed causing stone displacement. In the case of wall-modelled LES, the near wall RANS region is not present and thus it was hypothesized that a correct initiation of the shear layer would be possible.

- Secondly, additional post-processing of the IDDES results revealed an under prediction of free turbulence (2.11 and 2.14). The reason for that could not be directly linked to a process or numerical feature of IDDES but it was realized as a model limitation and point for further improvement in the next model to be build.

- Thirdly, according to literature it was seen that frequencies up to the stone size are important for stone stability. As discussed also in Stevens (2018), this was not achieved with IDDES and there is room for improvement (see figure 2.13).

- Lastly, in case of IDDES an uncertainty exists in the interface between the LES and the RANS model and it is not clear what effect this has on the results (near wall region after the sill). By using wall-modelled LES, this interface is no longer there, without additional computational costs, since the demands for IDDES and WMLES are comparable.

Which is the most appropriate method to include bottom roughness in the case of granular bed protections in such flows based on literature?

In this thesis special attention is paid on the way the granular bed protection is included in the numerical model. The main challenges noticed, is firstly, the high Reynolds number engineering flows that this study is dealing with, which make the resolution of the inner layer very expensive. The second one is the large size of the roughness elements which makes their inclusion in the LES environment not straightforward.

The following methods were investigated to represent the rough boundary:

- porous layer approach

- the momentum forcing approach as described by Stoesser (2010)

- explicitly resolving the stones

- wall functions

From the above the WMLES method was selected due to:

1. computational limitations
2. not a priori knowledge of the distribution of stones of the gravel bed

Concerning the first limitation, in all cases except for the wall functions the inner layer should be resolved (section 2.2.3). In addition, in the stoesser's approach and also in the case of resolving the stones, sufficient amount of grid cells is needed per stone element. Apart from that in the case of resolving the stone elements and the stoesser's approach, the distribution of the gravel bed must be known a priori. However, in the momentum forcing approach, a roughness function is proposed and then additional investigation must be done to realize if this could be used to generate a gravel bed.

That being said, the WMLES is proposed in this thesis (see also 2.2.4) as the next step in this study. The focus is then on the correct prediction of the effect of a rough bed on a spatial average sense and not on capturing individual stones.

How does WMLES perform in predicting wall shear stress in fully rough open channel flow?

The performance of wall functions that take roughness into account in the LES environment, and especially within OpenFOAM is not a well-studied area and therefore it was decided that simple open channel flow case will be performed to evaluate wall functions in LES. In section 3.1, the model set-up is presented based on similar studies. The results (section 4.1) showed that only the `nutURoughWallFunction` (see also section 2.2.3 for details on this function) delivered sensible results (figure 4.3). In addition, the Smagorinsky and WALE subgrid model were tested along with the `nutURoughWallFunction` and the Smagorinsky model resulted in smaller error (figure 4.5). The errors appear to be lower for larger grid cell size to equivalent sand grain diameter (figure 4.7). However, still a 10% was present. In section 4.1, the uncertainty present in the theoretical log-law used for validation is discussed and it is concluded that experimental results should be used instead of this theoretical law before more solid conclusions can be drawn on the wall functions performance in LES.

Which sub-grid scale model is more appropriate when modelling rough walls with wall functions in LES?

In section 4.1, where the results are shown for the open channel flow case, it can be seen that the Smagorinsky model performed better (figure 4.5). This is also true for the long sill case. Along the tested sub-grid scale models (WALE, Smagorinsky, Dynamic Smagorinsky and k-equation model), Smagorinsky performed best (see figures 4.14, 4.16). Based on the literature review in section 2.2.2, this model would not be the first choice for LES mainly due to its dissipative character (see figure 4.18). A dynamic model would probably be a more preferable choice. However based on the results, the Dynamic Smagorinsky and the WALE model, failed to capture the recirculation zone. The latter one also produced a larger error than the Smagorinsky model in the simple open channel flow case (see figure 4.5). Therefore the Smagorinsky model is suggested. It is hypothesized that the wall functions and the dynamic procedure in sub-grid models cannot be applied together without conflict. The reason why is probably not trivial and further investigation is needed. To the researcher's knowledge, the behavior of the sub-grid scale models near the wall where wall functions are applied is still an open research area.

How does WMLES perform in predicting high frequencies important for stone stability studies?

As discussed from literature in section 2.1.1, frequencies up to the stone size contribute to the initiation of motion. It is seen that the present model is able to resolve these frequencies, improving the prediction by an order of magnitude from the IDDES model (figure 5.5).

Lastly, the main question is addressed:

Which hydrodynamic numerical tool can be used for the prediction of the governing mechanisms associated with stone stability, in case of non-uniform high Reynolds number flows?

The main features of the numerical tool proposed in this thesis are given below. Capabilities and limitations are also mentioned below.

- The LES turbulence model is suggested along with the Smagorinsky sub-grid model. The k-equation sub-grid model also yielded acceptable results and is suggested along with Smagorinsky.

- The use of wall functions to represent the rough boundary is implemented in this study. More specifically, only the `nutURoughWallFunction` is suggested among other ones implemented in OpenFOAM. Any smooth walls present can be modelled with the `nutUWallFunction`. Both of these wall functions calculate a modified viscosity ν_w based on the velocity (see also section 2.2.3).

- Since in OpenFOAM implicit filtering is used, the choice of the mesh size is important for the performance of the sub-grid model. In addition, in order to achieve the target frequency that corresponds to the stone size and resolve the shear layer, a mesh of 4 mm is used. However according to the results of the open channel flow case at section 4.1, such a grid cell size to stone size ratio yields a non-negligible error in predicting the bed shear stress. It is then a compromise between resolving wall and free turbulence that one has to make if this numerical model set-up is used (see also the corresponding discussion in section 5).

- The inflow boundary condition is of prior importance for the LES simulation. A synthetic method approach as suggested by Poletto et al. (2013) was used in the present thesis (see section 2.2.2 for a description). The performance of this boundary condition could not be tested (see also section 4.3), but some attention must be paid in that before this model is used for other applications, since the shear layer development is very sensitive to the inflow fluctuations (Sagaut (2006)).

- The Wall-Modelled LES method appeared to improve the prediction of the shear layer development and to resolve eddies down to the stone size. These are factors that should be taken into account when one has to choose between RANS, IDDES or WMLES for the purposes of this research area. In addition, it is concluded that the computational demands of the IDDES and WMLES model are comparable, namely around 30 days are needed to simulate 3 minutes using 40 cores.

Lastly, it is noted that the above described numerical model relies solely to the capabilities and models already implemented in OpenFOAM. Since it is an open source code, further improvements to the already existing models or implementation of completely new ones can be easily applied. This makes OpenFOAM a suitable code for academic purposes.

7

Recommendations

In this thesis the potential of Wall-Modelled Large Eddy Simulation (WMLES) is explored for the aim of determining the stone stability in granular bed protections. The WMLES method itself and especially with wall functions that account for roughness, is a relatively unexplored area, so further research is needed. Recommendations on numerical and other aspects are given below:

- It has been more than 10 years since an experiment for the purpose of determining the stone stability in a granular bed protection is undertaken. The application of more sophisticated CFD methods, requires the availability of more detailed experimental campaigns. Furthermore, through the work done in the current thesis and also through the work of Stevens (2018), experience and important knowledge is gathered so that the next time that an experiment is undertaken, certain measures will be taken to help the creation of a "numerical twin" of the experiment. According to literature, the mixing layer is sensitive to the synthetic turbulence generation. It is therefore recommended that at least velocity and turbulence intensity measurements are undertaken before the area of interest in the model, to enable a more accurate prediction and validation of such boundary conditions. Secondly, information for the flow features over the width could also prove valuable for the validation of the numerical 3D model.

- More investigation is needed on the performance of the synthetic turbulence generation method used in thesis (Poletto et al. (2013)), to examine if this is reason why the amount of TKE downwards the sill is over-predicted. Another alternative is the use of a new synthetic turbulence generation method available in the OpenFOAM version 1906, at the inflow boundary condition. This is based on the Digital-Filter Method (DFM). This is not analyzed here or tested in this work, since it was released by the end time of this thesis.

- In section 4.1 , the wall function performance is evaluated in the WMLES environment. To that end the numerical model results were compared to the theoretical log-law for rough walls. As a next step the validation with experimental or DNS results is recommended. The researcher then should find open channel flow cases with roughness belonging to the fully rough regime and calculated shear stresses. For the purposes of wall sensitivity tests many researchers use the data from Moser R.D. and N.N. (1999) but these are only suitable for smooth wall calculations.

- Concerning the near wall region it is not fully understood why certain sub-grid models performed better than others. Apart from that, the way the subgrid-scale in say $y^+ = 30$ should be formulated near the wall is still an open question, even in case of smooth walls. In the present application, the near wall behavior is of interest so that more investigation is needed.

- Apart from the wall functions used in this thesis, other methods are discussed to represent rough boundaries in the LES environment. Among them, the momentum forcing approach as described by Stoesser et al. (2010) seems like an attractive alternative. An attempt to implement this method is OpenFOAM is described in Margalit (2015). The challenges that such implementation would entail are already presented in section 2.2.3, with the most important one being the computational demands. However, simple open channel flow cases can be done in low Reynolds numbers to inspect the limits of this approach and the suitability of this to describe a granular bed.
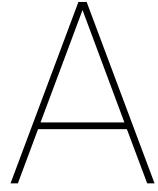
Bibliography

Amir, M., Nikora, V. I., and Stewart, M. T. (2014). Pressure forces on sediment particles in turbulent open-channel flow: a laboratory study. *Journal of Fluid Mechanics*, 757:458–497.

Balen, W. V. (2010). *Curved open-channel flows: A numerical study*. PhD thesis, TU Delft.

Benhamadouche, S., Jarrin, N., Addad, Y., and Laurence, D. (2006). Synthetic turbulent inflow conditions based on a vortex method for large-eddy simulation. *Progress in computational fluid dynamics*, 6(1/3):50.

Bradshaw, P. and Wong, F. (1972). The reattachment and relaxation of a turbulent shear layer. *Journal of Fluid Mechanics*, 52(1):113–135.

Bredberg, J. (2000). On the wall boundary condition for turbulence models. *Chalmers University of Technology, Department of Thermo and Fluid Dynamics. Internal Report 00/4. G oteborg.*

Breugem, W., Boersma, B., and Uittenbogaard, R. (2006). The influence of wall permeability on turbulent channel flow. *Journal of Fluid Mechanics*, 562:35–72.

De Gunst, M. (1999). Steenstabiliteit in een turbulente stroming achter een afstap. Master's thesis, TU Delft.

DeRuijter, R. (2004). Turbulence structures affecting stone stability in backward-facing step flow. experiments by means of piv. Master's thesis, TU Delft.

Dessens, M. (2004). The influence of an accelerating flow on the stability of stones. Master's thesis, TU Delft.

Driest, E. V. (1956). On turbulent flow near a wall. *Journal of the aeronautical sciences*, 23(11):1007–1011.

Fan, F., Liang, B., Li, Y., Bai, Y., Zhu, Y., and Zhu, Z. (2017). Numerical investigation of the influence of water jumping on the local scour beneath a pipeline under steady flow. *Water*, 9(9):642.

Fuhrman, D. R., Sumer, B. M., and Fredsøe, J. (2011). Roughness-induced streaming in turbulent wave boundary layers. *Journal of Geophysical Research: Oceans*, 116(C10).

Hinterberger, C., Fröhlich, J., and Rodi, W. (2007). Three-dimensional and depth-averaged large-eddy simulations of some shallow water flows. *Journal of Hydraulic Engineering*, 133(8):857–872.

Hoan, N. (2008). *Stone Stability Under Non-uniform Flow*. PhD thesis, TU Delft.

Hoffmans, G. (2006). Stability of stones under non-uniform. Master's thesis, Rijkswaterstaat.

Hofland, B. (2005). *Rock & Roll - Turbulence-induced damage to granular bed protections*. PhD thesis, TU Delft.

Hofland, B. and Battjes, J. A. (2006). Probability density function of instantaneous drag forces and shear stresses on a bed. *Journal of Hydraulic Engineering*, 132(11):1169–1175.

Huijsmans, M. (2006). The influence of flow acceleration on the stability of stones. Master's thesis, TU Delft.

Isbash, S. (1932). Construction of dams by dumping stones into flowing water. Technical report, USACE.

Jarrin, N., Prosser, R., Uribe, J.-C., Benhamadouche, S., and Laurence, D. (2009). Reconstruction of turbulent fluctuations for hybrid rans/les simulations using a synthetic-eddy method. *International Journal of Heat and Fluid Flow*, 30(3):435–442.

Jayatilleke, C. (1969). The influence of prandtl number and surface roughness on the resistance of the laminar sub- layer to momentum and heat transfer(laminar sublayer resistance to momentum and heat transfer, noting effects of prandtl number and surface roughness using mathematical model and experiments).

Jongeling, T., Blom, A., Jagers, H., Stolker, C., and Verheij, H. (2003). Ontwerpmethodiek granulaire verdediginen.pdf. Technical report, Delft Hydraulics.

Liu, F. (2017). Student project - a thorough description of how wall functions are implemented in openfoam.

Lund, T. S., Wu, X., and Squires, K. D. (1998). Generation of turbulent inflow data for spatially-developing boundary layer simulations. *Journal of computational physics*, 140(2):233–258.

Margalit, J. (2015). Student project - modeling of bed roughness using a geometry function and forcing terms in the momentum equations.

Menter, F. R. (1992). Improved two-equation k-omega turbulence models for aerodynamic flows.

Moin, P. and Kim, J. (1982). Numerical investigation of turbulent channel flow. *Journal of fluid mechanics*, 118:341–377.

Moser R.D., K. J. and N.N., M. (1999). Dns of turbulent channel flow up to re_{tau}=590. *Phys. Fluids*, 11:943–945.

Mukha, T. (2018). *Modelling Techniques for Large-Eddy Simulation of Wall-Bounded Turbulent Flows*. PhD thesis, Acta Universitatis Upsaliensis.

Mukha, T. and Liefvendahl, M. (2015). Large-eddy simulation of turbulent channel flow. Technical report, tech. rep., Uppsala University, Department of Information Technology.

Mukha, T., Rezaeiravesh, S., and Liefvendahl, M. (2018). A library for wall-modelled large-eddy simulation based on openfoam technology. *arXiv preprint arXiv:1807.11786*.

Nakagawa, H. and Nezu, I. (1987). Experimental investigation on turbulent structure of backward-facing step flow in an open channel. *Journal of Hydraulic Research*, 25(1):67–88.

Nelson, J. M., McLean, S. R., and Wolfe, S. R. (1993). Mean flow and turbulence fields over two-dimensional bed forms. *Water Resources Research*, 29(12):3935–3953.

Nezu, I. and Nakagawa, H. (1989). Turbulent structure of backward-facing step flow and coherent vortex shedding from reattachment in open-channel flows. In *Turbulent shear flows 6*, pages 313–337. Springer.

Nicoud, F. and Ducros (1999). Subgrid-scale stress modelling based on the square of the velocity gradient tensor. *Flow, turbulence and Combustion*, 62(3):183–200.

Nikuradse, J. (1933). *Strömungsgesetze in rauhen Rohren*. VDI-Verlag.

Nozaki, F. (2019). Fumiya nozaki's cfd blog.

Packman, A. I., Salehin, M., and Zaramella, M. (2004). Hyporheic exchange with gravel beds: basic hydrodynamic interactions and bedform-induced advective flows. *Journal of Hydraulic Engineering*, 130(7):647–656.

Papanicolaou, A., Diplas, P., Evaggelopoulos, N., and Fotopoulos, S. (2002). Stochastic incipient motion criterion for spheres under various bed packing conditions. *Journal of Hydraulic Engineering*, 128(4):369–380.

Passalacqua, A. (2010). dynamicsmagorinsky - implementation of the dynamic smagorinsky sgs model as proposed by lilly (1992) for openfoam. https://github.com/AlbertoPa/dynamicSmagorinsky.

Piomelli, U. and Balaras, E. (2002). Wall-layer models for large-eddy simulations. *Annual review of fluid mechanics*, 34(1):349–374.

Poletto, R., Craft, T., and Revell, A. (2013). A new divergence free synthetic eddy method for the reproduction of inlet flow conditions for les. *Flow, turbulence and combustion*, 91(3):519–539.

Pope, S. B. (2001). Turbulent flows.

Rodi, W., Constantinescu, G., and Stoesser, T. (2013). *Large-Eddy Simulation in Hydraulics*. International Association for Hydro-Environment Engineering and Research (IAHR).

Sagaut, P. (2006). *Large eddy simulation for incompressible flows: an introduction.* Springer Science & Business Media.

Schiereck, G. and Verhagen, H. (2012). *Introduction to bed, bank and shore protection.* VSSD, Delft, 2nd edition.

Schumann, U. (1975). Subgrid scale model for finite difference simulations of turbulent flows in plane channels and annuli. *Journal of computational physics*, 18(4):376–404.

Scotti, A. (2006). Direct numerical simulation of turbulent channel flows with boundary roughened with virtual sandpaper. *Physics of Fluids*, 18(3):031701.

Shields, A. (1936). *Anwendung der Aehnlichkeitsmechanik und der Turbulenzforschung auf die Geschiebebewegung.* PhD thesis, Berlin.

Shih, T.-H., Liou, W. W., Shabbir, A., Yang, Z., and Zhu, J. (1995). A new k- eddy viscosity model for high reynolds number turbulent flows. *Computers & Fluids*, 24(3):227–238.

Singh, K., Sandham, N., and Williams, J. (2007). Numerical simulation of flow over a rough bed. *Journal of Hydraulic Engineering*, 133(4):386–398.

Smagorinsky, J. (1963). General circulation experiments with the primitive equations: I. the basic experiment. *Monthly weather review*, 91(3):99–164.

Southard, J. (2006). Lecture notes: Introduction to fluid motions, sediment transport, and current-generated sedimentary structures - chapter 4, massachusetts institute of technology.

Spalart, P. (1997). Comments on the feasibility of les for wings, and on hybrid rans/les approach, advances in dns/les. In *Proceedings of 1st AFOSR International Conference on DNS/LES, 1997.*

Steenstra, R. (2014). Incorporation of the effects of accelerating flow in the design of granular bed protections. Master's thesis, TU Delft.

Steenstra, R., Hofland, B., Smale, A., Paarlberg, A., Huthoff, F., and Uijttewaal, W. (2016). Stone stability under stationary nonuniform flows. *Journal of Hydraulic Engineering*, 142(12).

Stevens, T. (2018). The prediction of stone stability by a three-dimensional eddy resolving simulation technique. Master's thesis, TU Delft.

Stoesser, T. (2010). Physically realistic roughness closure scheme to simulate turbulent channel flow over rough beds within the framework of les. *Journal of Hydraulic Engineering*, 136:812–819.

Stoesser, T. (2014). Large-eddy simulation in hydraulics: Quo vadis? *Journal of Hydraulic Research*, 52(4):441–452.

Stoesser, T., McSherry, R., and Fraga, B. (2015). Secondary currents and turbulence over a non-uniformly roughened open-channel bed. *Water*, 7(9):4896–4913.

Stoesser, T., Ruether, N., and Olsen, N. R. B. (2010). Calculation of primary and secondary flow and boundary shear stresses in a meandering channel. *Advances in Water Resources*, 33(2):158–170.

Tromp, M. (2004). Influences of fluid accelerations on the threshold of motion. Master's thesis, TU Delft.

Uijttewaal, W. (2002). Lecture notes: Turbulence in hydraulics, tu delft.

Verhagen, H. (2016). Lecture 2: Flow loads, bed bank and shoreline protection presentation.

Vollmer, S., de los Santos Ramos, F., Daebel, H., and Kühn, G. (2002). Micro scale exchange processes between surface and subsurface water. *Journal of Hydrology*, 269(1-2):3–10.

Vollmer, S. and Kleinhans, M. G. (2007). Predicting incipient motion, including the effect of turbulent pressure fluctuations in the bed. *Water Resources Research*, 43(5).

Wilcox, D. C. (1988). Reassessment of the scale-determining equation for advanced turbulence models. *AIAA journal*, 26(11):1299–1310.

Wu, X. (2017). Inflow turbulence generation methods. *Annual Review of Fluid Mechanics*, 49:23–49.

Yoshizawa, A. (1982). A statistically-derived subgrid model for the large-eddy simulation of turbulence. *The Physics of Fluids*, 25(9):1532–1538.

A

Stone Stability

Since both the hydraulic load on the bed and the resisting force of the particles have a random distribution, it is necessary to introduce a probabilistic approach. In that case, the convolution of the two distributions would yield the fraction of time that the instantaneous load exceeds the critical load. In case shear stresses are used this is translated to $p(\tau > \tau_c)$.

In their work Hofland and Battjes (2006), derived a PDF of the instantaneous drag forces and shear stresses using measured pressures on a bed-mounted cube. In their model, they assumed the drag law:

$$F = \frac{1}{2}\rho C_D A |u_b| u_b \tag{A.1}$$

meaning that the instantaneous drag force on the bed is proportional to the instantaneous near-bed velocity squared, with conservation of sign. In Hofland and Battjes (2006), the work of (Papanicolaou et al., 2002) is used as a starting point. In the latter, the use of the x2-distribution for the PDF of the drag force is proposed, based on the assumption that the drag is proportional to u_b^2 and that the near bed velocity u_b is Gaussian in distribution. However in (Hofland and Battjes, 2006) they adjusted their PDF based on the fact that the drag force in actually proportional to near bed velocities according to:

$$F = \alpha |u_b| u_b \tag{A.2}$$

where α is constant.

The final PDF proposed in is of the form:

$$p(F) = \frac{1}{2\sqrt{2\pi\alpha|F|}} exp[-\frac{1}{2}(\sqrt{|F|/\alpha} - sign(F)\delta)^2] \tag{A.3}$$

with δ being the noncentrality parameter interpreted as the reciprocal of the relative near-bed turbulence intensity r:

$$r = \frac{1}{\delta} = \frac{\sigma(u_b)}{\overline{u_b}} \tag{A.4}$$

By comparing their derived PDF with measured ones they concluded that the measured near-bed velocity can be approximated quite well by a Gaussian distribution. For normal (uniform flow) to low (nondeveloped turbulence) turbulence intensity, the PDF was represented very well. For large relative turbulence intensities (flow behind a backward-facing step), only the positive tails of the distribution are represented well. This part of the PDF is most important for modeling sediment transport.

The authors also mention the limits of the theory. More specifically, they highlight the absent of the inertia force, proportional to fluid acceleration $\frac{\Delta U}{\Delta t}$ and the disconnection of the vertical velocity in the drag force.

Concerning the PDFs of the lift forces, they are expected to be associated with the TWP induced forces as well. In Hofland and Battjes (2006) it was noted that for the lowest exposures, the resulting pdf is quite symmetrical. That could be a characteristic of the TWP since a convecting pressure field is expected to give similar pressure statistics at both sides of the stone and hence a symmetrical pdf. In Hofland and Battjes (2006) it is also stated that the behavior of the lift force (both mean and fluctuating) remains a topic for further research. As this force is generally caused by smaller-scale fluctuations, it is also less obvious to link it directly to the shear stress.

In need of coupling the stability parameter ψ with a bed response, a method is needed to define whether a bed is stable or not. In literature two methods are recognized:

1) the threshold of motion
2) stone transport approach

In the first one, it is assumed that there is a certain value of the stability parameter above which movement occurs:

$$\psi \geq \psi_c \tag{A.5}$$

This is the method commonly used in practice. The most famous stability relations that used the threshold of motion concept are Shields (1936) and Isbash (1932). In those, a critical value of the stability parameter is derived from measurements. In the design, in practice the nominal stone diameter is chosen such that this critical stability parameter is not exceeded. Several issues arising from the definitions of the the threshold of motion concept are listed below:

1) The condition at which the threshold of motion occurs, is rather subjective since the movement of stones can be interpreted in different ways.
2) Due to the irregularities of natural stones the position, the protrusion and hence the exposure and stability is different for every stone in the bed. Therefore, it can be said that one threshold of motion for the entire bed does not exist.
3) The threshold of motion concept gives no information about the damage to the bed when the critical stability parameter is exceeded.

In the second one, a certain value of the stability parameter is coupled to the bulk transport of stones from the bed. The main advantage of the stone transport concept is that it gives information and control on how the bed behaves after the stones become unstable. A general form of this method can be written as:

$$\phi = f(\psi) \tag{A.6}$$

with:

ψ the dimensionless stability parameter

ϕ the dimensionless transport parameter

Concerning the stability parameter ϕ, this should include a way to describe the transport of particles. Two different definitions are discussed below:

1) The bed load transport q_s, equal to the number of particles transported through a cross-section per unit of time
2) The volume entrainment rate E, equal to the number of pick-ups per unit area and time

The volume entrainment rate can be interpreted as the average lowering speed from the bed. It can be described by:

$$E = \frac{nd^3}{AT} \tag{A.7}$$

with:

E the entraintment rate [m/s]

n the number of stones picked-up [-]

d the stone diameter [m]

A the surface are [m^2]

T the time [s]

The dimensionless entraintment rate ϕ_E can be obtained as:

$$\phi_E = \frac{E}{\sqrt{\Delta g d}} \tag{A.8}$$

In Hoan (2008) it is stated that because of the dependence of the bed load transport on upstream hydraulics (the stones passing a certain cross-section is a function of all the entrained stones upstream) the bed load transport is a non-local parameter. The stability parameter ψ, however, is a local parameter (solely depending on local flow characteristics). However, the entrainment rate is completely dependent on local hydrodynamic parameters. Following this, it can be stated that the relation between ψ and ϕ is also valid for non-uniform flow.

B

Choosing a modelling software

In this appendix, motivation for choosing the modelling software is discussed. In the framework of the thesis, this choice was made mostly after the research gaps where identified, and new research goals was set. The main parameters taken into account, are the possibilities and limitations of the various codes to simulate the governing physics and also practical matters, such as the availability of the codes in the computational facilities open for master students. That being said, a short overview of the considered choices is given below.

B.1. Academic LES code

This computational model had been developed at the Laboratory for Aero and Hydrodynamics of the TU Delft initially for the purpose of simulating pipe flows. Later, its applicability got extended to bend flows. It should be noted that the Immersed Boundary Method (IBM) method in combination with wall modelling has been added to the code, making it attractive to the application of this thesis. It is available on the Hydraulic Engineering cluster. (I CANNOT FIND IT!).

One of the limitations of the code is that the free surface is treated as horizontal, impermeable rigid lid where the free slip condition is applied. The Smagorinsky subgrid-modelling technique is the only one available within the code. More information on this numerical model can be found at Balen (2010)

B.2. StarCCM+

This is a commercial CFD code by SIEMENS. Since the predecessor of this research topic made use of this code, attention was paid to the possibility to be used in the present thesis as well. This code is available in the Deltares computational facility.

In the advantages of this choice is the fact that the user has already experience in using this code as part of internship work in Deltares. There is also support in Deltares by experts in this code, as well as elaborate documentation by SIEMENS.

The disadvantage that led to the overlook of this choice is the limited computational capacity of the Deltares facility, which thought to be insufficient with respect to what was needed to the study of Stevens (2018). It is also the view of the author that such an commercial hard-coded software is not well suited for academic purposes research, when considering the current thesis to be part of a research area to be continued also in the future.

B.3. OpenFOAM

OpenFOAM is a free and open source Computational Fluid Dynamics (CFD) software package and is short for Open Field Operation And Manipulation. It is both available in the Deltares as well as the Hydraulic Engineering cluster. It has a large user base across most areas of engineering and science, from both commercial and academic organizations.

The software does not have a Graphical User Interface (GUI) and some basic knowledge of UNIX is needed to start modelling. The large variety of tutorials available make the start of the modelling easier. However there is not a universal platform of validated cases, nor an extensive manual to support the users. Much experience lies in forums and social CFD platforms, but it is in many cases difficult to discern what is valuable and what is not. Due to the above OpenFOAM has a steep learning curve.

There are also reported difficulties in modelling the free surface using OpenFOAM with the VOF solvers. Should that become a necessity, OpenFOAM could pose a real challenge in the user.

On the advantage is that the users have the ability to modify the code and create new solvers and utilities. In addition the C++ code is available for everyone interested on getting a better insight on how the software works. Support by experts on the OpenFOAM is also available in Deltares and TU Delft. All the above make OpenFOAM an attractive modelling choice for the present thesis.

B.4. DNS code for flow through and over a permeable wall

This code is also a modification of the LES academic code discussed in B.1. It is available within the Process & Energy Department of TU Delft. The usage of this code implies the modelling of bottom roughness with a porous layer approach. More about this approach and modelling technique can be found in Breugem et al. (2006).Support for the fortran-written code is possible.

The use of this approach in the current thesis implies the modification of the DNS code to an LES one. In combination with the limited experience of the user with fortran, the modification of such fundamental code could take a considerable amount of time.

B.5. Conclusion

Having discussed the above software, the choice was made to find balance between the fundamental LES codes and the commercial code with OpenFOAM. Choosing this code, the user could get insight on how the code works without the need to make large modifications. In addition, OpenFOAM is supported by both computational facilities available to the author and includes a variety of modelling techniques.

Two different versions of OpenFOAM were used within this thesis, depending on the boundary conditions and other modelling parameters available in each version. These are version 1812 by OpenCFD Ltd.and version 4.1 by OpenFOAM Foundation.

C

Cyclic Modelling [RANS]

This appendix describes the cyclic model, build to test the performance of wall functions with roughness in the RANS approach. Different turbulence closure models and wall functions are taken into account. The results are discussed and compared with the theoretical log-law for rough boundaries.The outcome of this parameter study, is taken into account in RANS long sill simulation. Many studies with wall functions are available. In particular the implementation of wall functions in OpenFoam in the RANS environment are widely tested and in some less extent systematically reported (Liu (2017), Bredberg (2000)).However, rough boundary cases and especially with roughness as high as our case are not that common.

C.1. Model set-up

In this section all important choices for the model set-up are given.

C.1.1. Flow conditions

A summary of the hydraulic parameters is presented in table C.1. The flow conditions are such that the fully rough flow regime is reached.

Geometry	h (cm)	$\overline{u}$ (cm)	Re (-)	Fr (-)	u_* (m/s)	k_s (mm)
flat bed	37.5	0.53	$2 \cdot 10^5$	0.2	0.0362	12.4

Table C.1: Hydraulic conditions for the cyclic case

C.1.2. Grid and boundary conditions

A simple 2D flat plate domain is built. The model consists of a rectangular box with length of 9δ in the streamwise direction and 2δ in the wall-normal direction, with $\delta = 1$ denoting the channel half-height. These dimensions are considered sufficient to accommodate the turbulence structures. Other configurations are tested with no significant difference in the results. In all cases, the domain mesh is represented by equidistant cubic cells.

Cyclic boundary conditions are applied in the inlet and outlet of the domain. The slip boundary condition is applied to the top boundary, while the no-slip condition is applied to the bottom (see figure C.1).
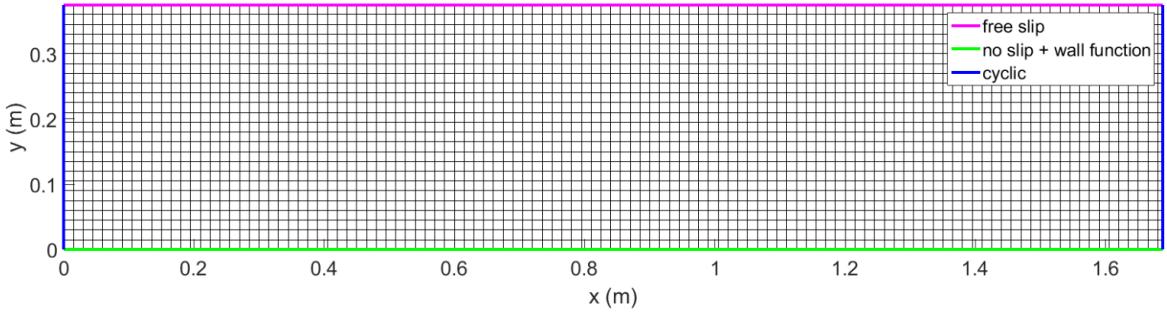
Figure C.1: Impression of the grid and the boundary conditions

To drive the flow in the domain, there is the choice to define the pressure gradient or the bulk mean velocity U_b. The computational procedures of fixing U_b, were already implemented in OpenFoam and known from past studies (eg. Mukha and Liefvendahl (2015)). It is also considered more realistic to prescribe a mean velocity or discharge rather than a pressure gradient to drive the flow. For these reasons the bulk mean velocity U_b is specified as input parameter in this study. However, the pressure gradient has to somehow be computed. This is done by introducing an additional external force term into the momentum equation. This artificial force drives the flow, and the magnitude of the force is determined by the prescribed bulk velocity. At each time step, the actual U_b is re-calculated, and an adjustment to the magnitude of the external force is made, to correct the value.

C.1.3. Turbulence model and wall Function

Regarding the turbulence model, several options are already available in OpenFoam. The k-ω by Wilcox (1988) or k-ω SST by Menter (1992) turbulence models are reported to be good approaches if one is dealing with separated flows (present in the long sill domain), as they perform particularly good in modelling the wall region when applied with a low value of y^+, namely close to 1. However in this thesis y^+ well above 30 are the aim. This means that the advantages of the k-ω SST are not in effect[and in addition one has the uncertainty of the k-e to k-omega transition.]That being said, also the choice is made to test the realizable $k - \epsilon$ model by Shih et al. (1995), which is an improved version of the standard k-ϵ and is also reported to perform good for separated flows.

Two different wall functions are tested. One is calculating the turbulent kinematic viscosity condition based on velocity (*nutURoughWallFunction*) and the other based on turbulent kinetic energy(*nutkRoughWallFunction*). Both wall functions take the equivalent sand grain diameter k_s as an input parameter. More information about the wall functions can be found in appendix TADE. These wall functions along with *nutkAtmRoughWallFunction* are the only functions implemented in OpenFoam able to include roughness. The latter one is not presented and tested here because it is designated for different applications.

Finally, it must be noted that the choice of turbulent viscosity wall functions, must be in line with the choice of both the turbulence model, and the choice of the wall functions for the turbulence parameters. For example, when viewing the near wall y^+ as a local Reynolds number, a viscous wall cell ($y^+ \approx 1$), must be accompanied by an ϵ and k wall function with the low Reynolds wall treatment available.

C.2. Results

Runs for different meshes are presented in C.2.1. Subsequently the turbulence model that performed best is evaluated against different rough wall functions in C.2.2.

C.2.1. k-ω SST vs Realizable k-ϵ

The results the realizable k-ϵ model are shown in figure C.2. The error produced by the model is less than 1.5% in all cases. This is of the order of the uncertainty of the log-law for rough boundaries which was used for validation.
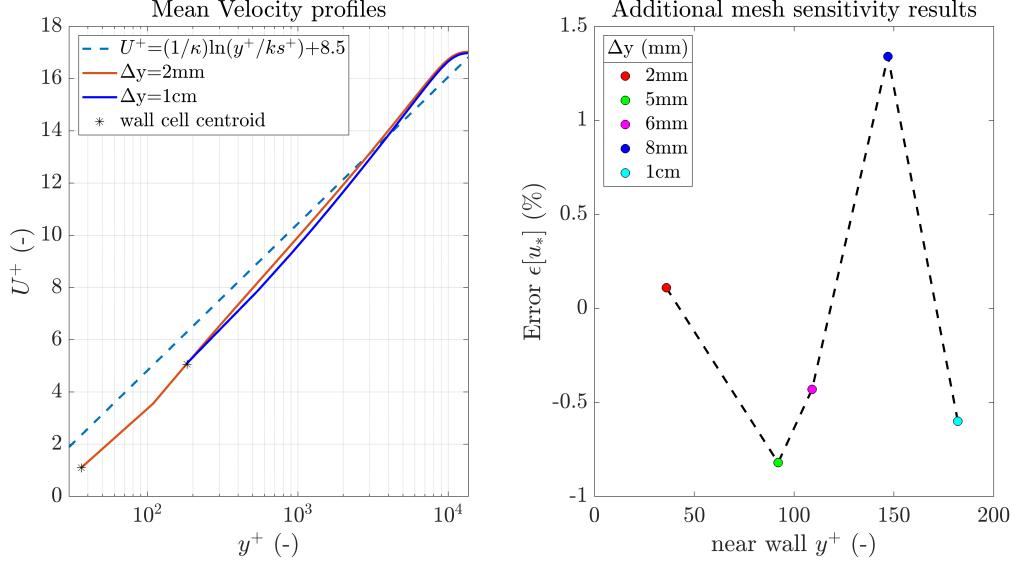
Figure C.2: Results of the realizable k-ϵ model. Left: plot of mean velocity profiles for the finer and coarser meshes used). Right: additional results for more y^+ tested.

The results the k-ω SST model are shown in figure C.3. The error produced by the model is of the order of 7% for all y^+ above 100. Only when the mesh is refined to reach $y^+ = 35$, the error drops to 4.7%, and reducing even more when finer meshes are used.
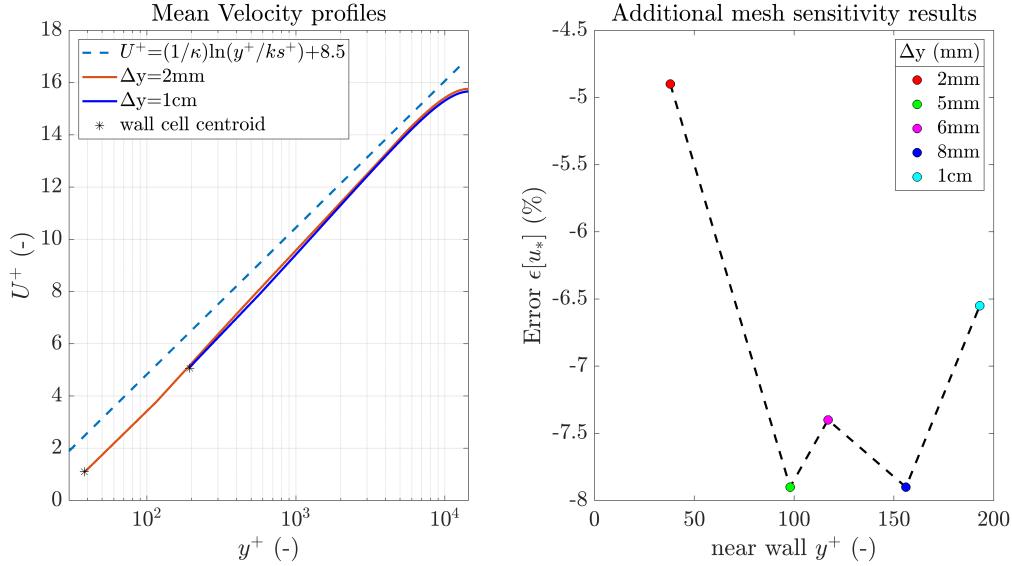
Figure C.3: Results of the realizable k-ω SST model. Left: plot of mean velocity profiles for the finer and coarser meshes used). Right: additional results for more y^+ tested.

C.2.2. *nutURoughWallFunction* vs *nutkRoughWallFunction*

In the previous section the *nutURoughWallFunction* was used for all cases. An additional test is done with the Realizable k-ϵ turbulence model, which performed best. This time the *nutkRoughWallFunction* is used, in a mesh of 8mm, which is the mesh later to be applied for the long sill simulations. Results are shown in table C.2, and reveal no significant sensitivity in the choice of the wall function in this simple flat domain case.
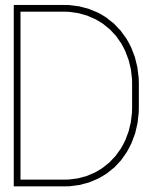
Wall Function	theoretical u_* (m/s)	model u_* (m/s)	Error $\epsilon[u_*]$ (%)
nutURoughWallFunction	0.0363	0.03679	-1.34
nutkRoughWallFunction	0.0363	0.037	-2

Table C.2: Comparison between different wall functions

C.3. Conclusion

In this section, the performance of wall function is evaluated. In the absence of experimental measurements, the theoretical log-law for rough boundaries is used. In this type of studies, many researchers use the DNS data of Moser R.D. and N.N. (1999). However, in our case even higher Re_τ values are expected, making this data set inadequate.

Out of the two turbulence models tested, the realizable k-ϵ turbulence model performed best, producing an error of the order of magnitude of the uncertainly of the log law for rough boundaries itself (up to 1.5%). Using the same set-up, the k-ω SST model produced an error up to 8%. Different wall functions seem to have a minor effect on the results. It is therefore the choice to proceed with the realizable k-ϵ turbulence model in the long sill domain.

D

OpenFOAM

In this section, some files of the mesh and numerics used in the open channel flow case and WMLES long sill case are given.

Openchannle flow case:

```
| =========                 |                                                 |
| \\      /  F ield          | OpenFOAM: The Open Source CFD Toolbox           |
| \\    /   O peration       | Version: 4.x                                    |
|  \\  /    A nd             | Web:     www.OpenFOAM.org                       |
|   \\/     M anipulation |                                                    |
\*---------------------------------------------------------------------------*/
FoamFile
{
    version    2.0;
    format     ascii;
    class      dictionary;
    object     blockMeshDict;
}
// * * * * * * * * * * * * * * * * * * * * * * * * * * * * * * * * * * * * * //


convertToMeters 1;

vertices
(
    (0 0 0)
    (0 0.375 0)
    (1.6875 0 0)
    (1.6875 0.375 0)
    (0 0 0.75)
    (0 0.375 0.75)
    (1.6875 0 0.75)
    (1.6875 0.375 0.75)
);

blocks
(
    hex (0 2 3 1 4 6 7 5) (210 47 94) simpleGrading (1 1 1)
);

boundary
(
```

```
    top
    {
        type patch;
        faces
        (
            (1 5 7 3)
        );
    }
    inlet
    {
        type cyclic;
      neighbourPatch outlet;
        faces
        (
            (0 4 5 1)
        );
    }
    outlet
    {
        type cyclic;
      neighbourPatch inlet;
        faces
        (
            (2 3 7 6)
        );
    }
    wall_bottom
    {
        type wall;
        faces
        (
            (0 2 6 4)
        );
    }
    front
    {
        type cyclic;
      neighbourPatch back;
        faces
        (
            (4 5 7 6)
        );
    }
    back
    {
        type cyclic;
      neighbourPatch front;
        faces
        (
            (0 2 3 1)
        );
    }

);

mergePatchPairs
(
);

// ********************************************************************* //
```

Listing D.1: Mesh of the Open Channel case

Long sill case:

```
/*--------------------------------*- C++ -*----------------------------------*\
| =========                 |                                                 |
| \\      /  F ield         | OpenFOAM: The Open Source CFD Toolbox           |
|  \\    /   O peration     | Version: 4.x                                    |
|   \\  /    A nd           | Web:      www.OpenFOAM.org                      |
|    \\/     M anipulation  |                                                 |
\*---------------------------------------------------------------------------*/
FoamFile
{
    version     2.0;
    format      ascii;
    class       dictionary;
    object      blockMeshDict;
}
// * * * * * * * * * * * * * * * * * * * * * * * * * * * * * * * * * * * * * //

convertToMeters 1;

vertices
(
    (-0.5 -0.001470588235 0 ) //0
    (-0.5 0.2 0) //1
    (-0.5 0.375 0) //2

  //(-1 -0.003 0) //3
  //(-1 0.2 0) //4
  //(-1 0.379 0) //5

    (0 0 0) //6
    (0 0.2 0) //7
    (0 0.377 0) //8

    (1 0.125 0)  //9
    (1 0.275 0)//10
    (1 0.36 0) //11

 (2.25 0.125 0)  //9
    (2.25 0.275 0)//10
    (2.25 0.347 0) //11


    (3.04 0.125 0) //12
    (3.04 0.275 0) //13
     (3.04 0.344 0) //14


    (3.4 0 0) //8 //15
    (3.4 0.2 0) //16
     (3.4 0.353 0) //17

    (3.95 0 0) //8 //18
    (3.95 0.2 0) //19
     (3.95 0.358 0) //20
```

```
    (4.15 0 0) //8 //21
    (4.15 0.2 0) //22
     (4.15 0.3585 0) //23

    (4.35 0 0) //8 //24
    (4.35 0.2 0) //25
     (4.35 0.359 0) //26

     (5.6 0 0) //27
     (5.6 0.2 0) //28
     (5.6 0.359 0) //29

    (-0.5 -0.001470588235 0.5 ) //0
     (-0.5 0.2 0.5) //1
     (-0.5 0.375 0.5) //2

    //(-1 -0.003 0.5)
    //(-1 0.2 0.5)
    //(-1 0.379 0.5)

     (0 0 0.5) //3
     (0 0.2 0.5) //4
     (0 0.377 0.5) //5

     (1 0.125 0.5)  //6
     (1 0.275 0.5)//7
    (1 0.36 0.5) //8

 (2.25 0.125 0.5)  //9
     (2.25 0.275 0.5)//10
     (2.25 0.347 0.5) //11

    (3.04 0.125 0.5) //9
    (3.04 0.275 0.5) //10
     (3.04 0.344 0.5) //11

    (3.4 0 0.5) //8 //12
    (3.4 0.2 0.5) //13
     (3.4 0.353 0.5) //14

    (3.95 0 0.5) //8 //12
    (3.95 0.2 0.5) //13
     (3.95 0.358 0.5) //14

    (4.15 0 0.5) //8 //12
    (4.15 0.2 0.5) //13
     (4.15 0.3585 0.5) //14

    (4.35 0 0.5) //8 //12
    (4.35 0.2 0.5) //13
     (4.35 0.359 0.5) //14

    (5.6 0 0.5) //15
    (5.6 0.2 0.5) //16
     (5.6 0.359 0.5) //17


);
//this is 8mm grid
```

```
blocks
(
    hex (0 3 4 1 30 33 34 31) (125 50 125) simpleGrading (1 1 1) //0
    hex (1 4 5 2 31 34 35 32) (125 14 125) simpleGrading (1 6.15 1) //1
    hex (3 6 7 4 33 36 37 34) (250 50 125) simpleGrading (1 1 1) //2
    hex (4 7 8 5 34 37 38 35) (250 14 125) simpleGrading (1 6.15 1) //3
    hex (6 9 10 7 36 39 40 37) (313 50 125) simpleGrading (1 1 1) //4
    hex (7 10 11 8 37 40 41 38) (313 14 125) simpleGrading (1 6.15 1) //5
    hex (9 12 13 10 39 42 43 40) (198 50 125) simpleGrading (1 1 1) //6
    hex (10 13 14 11 40 43 44 41) (198 14 125) simpleGrading (1 6.15 1) //7
    hex (12 15 16 13 42 45 46 43) (90 50 125) simpleGrading (1 1 1) //8 //SIDE SLOPE
    hex (13 16 17 14 43 46 47 44) (90 14 125) simpleGrading (1 6.15 1) //9
    hex (15 18 19 16 45 48 49 46) (138 50 125) simpleGrading (1 1 1) //10
    hex (16 19 20 17 46 49 50 47) (138 14 125) simpleGrading (1 6.15 1) //11
  hex (18 21 22 19 48 51 52 49) (50 50 125) simpleGrading (1 1 1) //12
  hex (19 22 23 20 49 52 53 50) (50 14 125) simpleGrading (1 6.15 1) //13
  hex (21 24 25 22 51 54 55 52) (50 50 125) simpleGrading (1 1 1) //14
  hex (22 25 26 23 52 55 56 53) (50 14 125) simpleGrading (1 6.15 1) //15
  hex (24 27 28 25 54 57 58 55) (313 50 125) simpleGrading (1 1 1) //16
  hex (25 28 29 26 55 58 59 56) (313 14 125) simpleGrading (1 6.15 1) //17

);

edges
(
);

boundary
(
    inlet
    {
        type patch;
        faces
        (
            (0 30 31 1)
       (1 31 32 2)
        );
    }
    outlet
    {
        type patch;
        faces
        (
            (27 28 58 57)
       (28 29 59 58)
        );
    }
    lowerWall
    {
        type wall;
        faces
        (
       (0 3 33 30)
     (3 6 36 33)
         (6 9 39 36)
         (9 12 42 39)
         (12 15 45 42)
       (15 18 48 45)
       (18 21 51 48)
       (21 24 54 51)
       (24 27 57 54)
```

```
        );
    }
    top
    {
        type patch;
        faces
        (

    (2 32 35 5)
    (5 35 38 8)
    (8 38 41 11)
    (11 41 44 14)
    (14 44 47 17)
            (17 47 50 20)

    (20 50 53 23)

    (23 53 56 26)

    (26 56 59 29)

        );
    }
    frontAndBack
    {
        //type wall;
        type wall;
        faces
        (
        (0 1 4 3)
        (1 2 5 4)
        (3 4 7 6)
        (4 5 8 7)
        (6 7 10 9)
        (7 8 11 10)
        (9 10 13 12)
        (10 11 14 13)
        (12 13 16 15)
        (13 14 17 16)
        (15 16 19 18)
        (16 17 20 19)
        (18 19 22 21)
        (19 20 23 22)
        (21 22 25 24)
        (22 23 26 25)
        (24 25 28 27)
        (25 26 29 28)

        (30 33 34 31)
        (31 34 35 32)
        (33 36 37 34)
        (34 37 38 35)
        (36 39 40 37)
        (37 40 41 38)
        (39 42 43 40)
        (40 43 44 41)
        (42 45 46 43)
        (43 46 47 44)
        (45 48 49 46)
```

```
        (46 49 50 47)
        (48 51 52 49)
        (49 52 53 50)
        (51 54 55 52)
        (52 55 56 53)
        (54 57 58 55)
        (55 58 59 56)
    );
    }
);

mergePatchPairs
(
);

// ************************************************************************* //
```

Listing D.2: Mesh of the WMLES Long Sill case

```
/*--------------------------------*- C++ -*----------------------------------*\
| =========                 |                                                 |
| \\      /  F ield         | OpenFOAM: The Open Source CFD Toolbox           |
| \\    /   O peration      | Version: 4.0                                    |
|  \\  /    A nd            | Web:      www.OpenFOAM.org                      |
|   \\/     M anipulation   |                                                 |
\*---------------------------------------------------------------------------*/
FoamFile
{
    version     2.0;
    format      ascii;
    class       dictionary;
    location    "system";
    object      fvSchemes;
}
// * * * * * * * * * * * * * * * * * * * * * * * * * * * * * * * * * * * * * //

ddtSchemes
{
    default         backward;
}

gradSchemes
{
    default         leastSquares;
}

divSchemes
{
    default         none;
    div(phi,U)      Gauss LUST grad(U); //second order accurate, unbounded but more stable than linear
    div(phi,k)      Gauss linear;
    div(B)          Gauss linear;
    div(phi,B)      Gauss limitedLinear 0.1;
    div((nuEff*dev2(T(grad(U))))) Gauss linear;

}

laplacianSchemes
{
    default         Gauss linear corrected;
}
```

```
interpolationSchemes
{
    default        linear;
}

snGradSchemes
{
    default        corrected;
}

wallDist
{
    method meshWave;
}


// *************************************************************************** //
```

Listing D.3: fvSchemes of the WMLES Long Sill case

```
/*--------------------------------*- C++ -*----------------------------------*\
| =========                 |                                                 |
| \\      /  F ield          | OpenFOAM: The Open Source CFD Toolbox           |
| \\    /   O peration       | Version: 4.0                                    |
|  \\  /    A nd             | Web:     www.OpenFOAM.org                       |
|   \\/     M anipulation |                                                 |
\*---------------------------------------------------------------------------*/
FoamFile
{
    version    2.0;
    format     ascii;
    class      dictionary;
    location   "system";
    object     fvSolution;
}
// * * * * * * * * * * * * * * * * * * * * * * * * * * * * * * * * * * * * * //

solvers
{
  p
  {
      solver         GAMG;
      tolerance      1e-6;
      relTol         0;
      smoother       DIC;
      cacheAgglomeration true;
      nCellsInCoarsestLevel 10;
      agglomerator   faceAreaPair;
      mergeLevels    1;

  }

  pFinal
  {
      $p;
      smoother       DICGaussSeidel;
      tolerance      1e-8;
      relTol         0;
  smoother  DIC;
  }
```

```
    "(U|k|epsilon|omega|f|v2)"
    {
        solver                  PBiCG;
        preconditioner             DILU;
        tolerance               1e-8;
        relTol                  0.0;
    }

    "(U|k|epsilon|omega|f|v2)Final"
    {
        $U;
        tolerance       1e-8;
        relTol          0;
    }
}



PISO
{
    nOuterCorrectors 1;
    nCorrectors     3;
    nNonOrthogonalCorrectors 2;
    momentumPredictor yes;
}



// ************************************************************************* //
```

Listing D.4: fvSolution of the WMLES Long Sill case

```
/*--------------------------------*- C++ -*----------------------------------*\
| =========                 |                                                 |
| \\      /  F ield         | OpenFOAM: The Open Source CFD Toolbox           |
|  \\    /   O peration     | Version: 4.x                                    |
|   \\  /    A nd           | Web:     www.OpenFOAM.org                       |
|    \\/     M anipulation  |                                                 |
\*---------------------------------------------------------------------------*/
FoamFile
{
    version     2.0;
    format      ascii;
    class       dictionary;
    location    "system";
    object      controlDict;
}
// * * * * * * * * * * * * * * * * * * * * * * * * * * * * * * * * * * * * * //

application    pisoFoam;

startFrom      startTime;

startTime      120;

stopAt         endTime;

endTime        5000;

deltaT         0.002;
```

```
writeControl   timeStep;

writeInterval 125;

purgeWrite     0;

writeFormat    ascii;

writePrecision 6;

writeCompression off;

timeFormat     general;

timePrecision 6;

runTimeModifiable true;

adjustTimeStep no;

maxCo          1;
maxAlphaCo     1;

maxDeltaT      1;

//Adding forces in the computation
libs
(
   "libutilityFunctionObjects.so"  //Library A
   "libsampling.so"      //Library B
);

functions
{
   residuals    //Name of the file and the folder in case/postProcessing/
   {
     type    residuals;
     enabled    true;
     writeControl timeStep;
     writeInterval 1;

     fields
     (
       P
       U
     );

   }

   yPlus
    {
       type        yPlus;
       libs        ("libfieldFunctionObjects.so");
       writeControl  timeStep;
   writeInterval 250;
    }


       shearStress
   {
       type        wallShearStress;
```

```
    libs            ("libfieldFunctionObjects.so");
    writeControl    timeStep;
writeInterval 250;
}

 turbulenceFields1
 {
    type        turbulenceFields;
    libs ("libfieldFunctionObjects.so");
writeControl    timeStep;
writeInterval 250;
    fields
    (
        R
        k
    );

 }
Q1
 {
    type            Q;
    libs            ("libfieldFunctionObjects.so");
    writeControl    timeStep;
writeInterval 250;
 }
 Lambda2
 {
    type            Lambda2;
    libs            ("libfieldFunctionObjects.so");
    writeControl    timeStep;
writeInterval 250;
 }

            CourantNo
 {
    type            CourantNo;
    libs            ("libfieldFunctionObjects.so");
    writeControl    timeStep;
writeInterval 250;
 }
            gradP
 {
    type            grad;
    libs            ("libfieldFunctionObjects.so");
    writeControl    timeStep;
writeInterval 250;
field    p;
 }
              gradU
 {
    type            grad;
    libs            ("libfieldFunctionObjects.so");
    writeControl    timeStep;
writeInterval 250;
field    U;
 }

        vorticity1
 {
    type            vorticity;
    libs            ("libfieldFunctionObjects.so");
```

```
    writeControl   timeStep;
writeInterval 250;
 }




fieldAverage1
 {
     type            fieldAverage;
     libs            ("libfieldFunctionObjects.so");
     writeControl   timeStep;
writeInterval 250;
       restartOnRestart no;

     fields
     (
        U
        {
            mean        on;
            prime2Mean on;
            base        time;
        }
     Lambda2
        {
            mean        on;
            prime2Mean on;
            base        time;
        }
        Q
        {
            mean        on;
            prime2Mean on;
            base        time;
        }
      CourantNo
        {
            mean        on;
            prime2Mean on;
            base        time;
        }
        p
        {
            mean        on;
            prime2Mean on;
            base        time;
        }
     wallShearStress
        {
            mean        on;
            prime2Mean on;
            base        time;
        }
     yPlus
        {
            mean        on;
            prime2Mean on;
            base        time;
        }
      turbulenceProperties:R
    {
```

```
      mean  on;
      prime2Mean on;
      base  time;
   }
   turbulenceProperties:k
   {
      mean  on;
      prime2Mean on;
      base  time;
   }
   nut
   {
      mean on;
      prime2Mean on;
      base  time;
   }
   grad(p)
   {
      mean on;
      prime2Mean on;
      base  time;
   }
   grad(U)
   {
      mean on;
      prime2Mean on;
      base  time;
   }
     );
  }


  wallNormal_profile
{

  type sets;
  libs ("libsampling.so");
   writeControl   timeStep;
  writeInterval  250;

  setFormat raw;

  surfaceFormat raw;

  interpolationScheme cellPoint ;

  fields
  (
     U  UMean UPrime2Mean p pMean turbulenceProperties:RMean turbulenceProperties:kMean nut nutMean yPlus yPlusM
  );


  sets
  (
    profile_inlet
    {
        type        face;
        axis        y;
        start       (-0.4 0 0.25);
        end         (-0.4 0.375 0.25);
```

```
    }

    profile_10
    {
        type        face;
        axis        y;
        start       (2.25 0.125 0.25);
        end         (2.25 0.375 0.25);

    }

    profile_1
    {
        type        face;
        axis        y;
        start       (3 0.125 0.25);
        end         (3 0.375 0.25);

    }
    profile_2
    {
        type        face;
        axis        y;
        start       (3.45 0 0.25);
        end         (3.45 0.375 0.25);
    }
    profile_2_width
    {
        type        face;
        axis        z;
        start       (3.45 0.05 0);
        end         (3.45 0.05 0.5);
    }
    profile_3
    {
        type        face;
        axis        y;
        start       (3.75 0 0.25);
        end         (3.75 0.375 0.25);
    }
    profile_4
    {
        type        face;
        axis        y;
        start       (3.95 0 0.25);
        end         (3.95 0.375 0.25);
    }
    profile_5
    {
        type        face;
        axis        y;
        start       (4.15 0 0.25);
        end         (4.15 0.375 0.25);
    }
    profile_6
    {
        type        face;
        axis        y;
        start       (4.35 0 0.25);
        end         (4.35 0.375 0.25);
    }
```

```
   profile_7
   {
       type        face;
       axis        y;
       start       (4.55 0 0.25);
       end         (4.55 0.375 0.25);
   }
     profile_8
   {
       type        face;
       axis        y;
       start       (4.95 0 0.25);
       end         (4.95 0.375 0.25);
   }
     profile_9
   {
       type        face;
       axis        y;
       start       (5.15 0 0.25);
       end         (5.15 0.375 0.25);
   }


   );

   surfaces
   (
   );

};

probes
   {
       // Where to load it from
       libs ( "libsampling.so" );

       type            probes;

       // Name of the directory for probe data
       name            probes;

       // Write at same frequency as fields
       writeControl   timeStep;
   writeInterval 5;

       // Fields to be probed
       fields
       (
          U   grad(p) Q Lambda2 p grad(U)
       );

       probeLocations
       (
               (3.75 0.02 0.25)      // profile 3 2cm
        (3.75 0.09 0.25)        // profile 3 9cm
        (3.75 0.20 0.25)        // profile 3 20cm
        (3.95 0.02 0.25)        // profile 4 2cm
        (3.95 0.09 0.25)        // profile 4 9cm
        (3.95 0.20 0.25)        // profile 4 20cm

        (4.15 0.02 0.25)   // profile 5 2cm
```

```
        (4.15 0.09 0.25)     // profile 5 9cm
        (4.15 0.20 0.25)     // profile 5 20cm
        (4.55 0.02 0.25)     // profile 7 2cm
        (4.55 0.09 0.25)     // profile 7 9cm
        (4.55 0.20 0.25)     // profile 7 20cm

        (3.75 0.002 0.25)       // profile 3 2mm
        (3.95 0.002 0.25)       // profile 4 2mm
        (4.15 0.002 0.25)       // profile 5 2mm

        (3.812 0.002 0.25)       // profile 3 2mm +6.2
        (4.012 0.002 0.25)       // profile 4 2mm
        (4.212 0.002 0.25)       // profile 5 2mm

        (3.812 0.02 0.25)       // profile 3 2cm +6.2
        (4.012 0.02 0.25)       // profile 4 2cm
        (4.212 0.02 0.25)       // profile 5 2cm



    );
   };


};

// ********************************************************************* //


// ********************************************************************* //


// ********************************************************************* //
```

Listing D.5: controlDict of the WMLES Long Sill case